**Advanced Techniques for Spectral and Temporal Ultrashort Pulse Synthesis in Coherent Pulse Stacking Amplification**

by

Mathew Whittlesey

A dissertation submitted in partial fulfillment
of the requirements for the degree of
Doctor of Philosophy
(Electrical and Computer Engineering)
in the University of Michigan
2023

Doctoral Committee:

Professor Almantas Galvanauskas, Chair
Professor Karl Krushelnick
Associate Professor Louise Willingale
Professor Herbert Winful

T. Mathew Whittlesey

tmwhitt@umich.edu

ORCID iD:  0000-0001-9252-3279

## Dedication

This thesis is dedicated to my fiancée, Rachel

**Acknowledgements**

I would like to thank all of the people I have met on my journey to completing my PhD, who have taught me so much, supported me, and provided guidance to become a better researcher.

First and foremost, I would like to thank my research advisor Professor Galvanauskas, who has taught me to think critically about problems and not get caught-up in the details. You have showed me not just how to be a problem solver, but to find the problems themselves. You have provided ample opportunities for me to learn and to teach others, which is an invaluable part of the learning process. I can honestly say that if you had not been my advisor, I don't think I would have done a PhD at all, so thank you for providing me a career path that I can be passionate about.

Next, I would like to thank all of my research colleagues I have worked with over the years: Alexander Rainville, Hanzhang Pei, John Ruppe, Yifan Cui, Siyun Chen, Mingshu Chen, Lauren Cooper, Christopher Pasquale, Yanwen Jing, Tayari Coleman, Yu Bai, Morteza Sheikhsofla, Michael Garner, and Weizhi Du. Developing this laser system has involved work from a lot of people, and I am grateful that it was such a helpful environment. These achievements wouldn't be possible without everyone else, and I can't wait to see what you all do next.

I would like to thank our collaborators at Lawrence Berkley National Lab: Tong Zhou, Qiang Du, and Russell Wilcox. Their knowledge of controls systems has been an invaluable

resource. Additionally, I'd like to thank Nicholas Peskosky from the University of Michigan for exploring applications with our laser system.

Additionally, I would like to thank my friends and family who have supported me through this journey, and always believed I could do it even when I didn't.

Lastly, I would like to thank my fiancé Rachel, who has supported me through thick and thin during this entire journey. Now that this chapter of our lives is closed, I can't wait to start the next one with you.

## Table of Contents

## List of Figures

## Abstract

Coherent combining methods enable scaling of average power and peak power in fiber laser systems. Coherent pulse stacking has the potential to enable high repetition rate laser-matter interactions by extending the effective pulse duration, enabling near-complete energy extraction from a fiber amplifier. This, along with coherent beam combining, provides a promising path to achieve efficient high-repetition rate laser sources for laser-matter interactions. This thesis explores the adaptable nature of coherent pulse stacking, and develops techniques to achieve repeatable, robust high-efficiency stacking. It also demonstrates, for the first time, simultaneous coherent spatial combining and coherent pulse stacking amplification.

Coherent pulse stacking was analyzed, and shown to be mathematically equivalent to a deep recurrent neural network. Different pulse amplitude profiles were shown to have minimal stacking loss, which demonstrates the adaptable nature of the technique. A method for increasing pre-pulse contrast by allowing post-pulses at the cost of efficiency was further developed and explored for equal-amplitude and equal nonlinear phase burst shapes. The impact of stacking parameter errors was quantified, and required tolerances for these parameters were derived. These analyses show stacking designs with >30 dB pre-pulse contrast and >95% stacking efficiency.

A theoretical framework for accounting effects of stacking alignment errors was developed, which enabled quantification of tilt and piston error impact on stacking efficiency via numerical simulations. This enabled determination of required alignment accuracies for achieving high efficiency stacking. Alignment methods to meet the required tolerances for both

tilt and piston errors were developed and implemented, achieving <5 μrad tilt accuracy and <2 μm piston accuracy and speeding up alignment. Additionally, oscillator repetition rate was locked to a highly stable rubidium frequency standard, eliminating oscillator cavity drift. In aggregate, all these technical advances significantly decreased system drift and enabled robust and stable stacking operation. As a result, high efficiency stacking of >80% stacking efficiency was achieved with high repeatability, robustness, and stability of <1% RMS.

Simultaneous coherent beam combining and coherent pulse stacking amplification was demonstrated for the first time. A record-high ultrashort pulse energy of 7 mJ per fiber was coherently spatially combined in a four-channel fiber array with a total energy of ~25 mJ, and stacked into a single output pulse with stacking efficiency of 70%. Stacking performance at these energies was shown to be stable and robust over long durations, with stabilization noise of 2.2% RMS. Stacking was shown to not affect compressed pulse duration, and stabilization of coherent beam combining was shown to not impact stacking efficiency. This represents a milestone in the development of coherently combined fiber lasers, enabling further scaling towards 100 mJ and beyond.

Finally, a technique to synthesize flat-top bandwidth-limited pulses using coherent spectral combining is developed. This method is directly compatible with other coherent combining techniques, which enables future scaling to high energies for generation of quasi-monoenergetic gamma photons via Thomson scattering. Spectral synthesis of the required spectrum is demonstrated with five spectral channels in a chirped pulse amplification system, and techniques for phase stabilization of spectral channels are developed.

In summary, this thesis work expands the understanding of coherent combining techniques, both spectral and temporal, and shows the adaptable nature of coherent pulse

stacking. When the techniques developed are used, high-energy high repetition rate laser sources are shown to be practically implementable via coherent combining techniques.

# Chapter 1 Introduction

## 1.1 Background

When lasers were first invented [1], it was said that they were "a solution looking for a problem". Since then, lasers have seen a multitude of advancements and applications. With the invention of mode-locking [2,3], ultrafast pulses became synthesizable, opening the way to light-matter interactions. The power and energy of laser pulses kept increasing until thermal and nonlinear limitations were encountered in gain media, limiting the achievable peak power of lasers for many years.

Eventually, a revolutionary breakthrough called Chirped Pulse Amplification (CPA) was invented [4], shown in Figure 1.1. CPA stretches ultrafast pulses in the time domain by nearly $10^5$ times, reducing the pulse peak power correspondingly. This is accomplished by inducing a temporal chirp on the pulses using a grating pair with imaging optics [5], enabling much larger amplification while avoiding nonlinear limitations in gain media. After amplification, pulses are compressed back to ultrafast durations using a grating pair [6].

CPA enables amplifying pulses to much higher peak powers, up to modern-day petawatt laser systems [7]. This has paved the way to high-field science and relativistic particle acceleration/production, however CPA laser systems face limitations in the form of grating size scaling. Grating size places a limitation on stretched pulse duration, and while steps are being taken to continue to improve grating size and performance [8], other approaches are necessary to stretch pulse durations further.

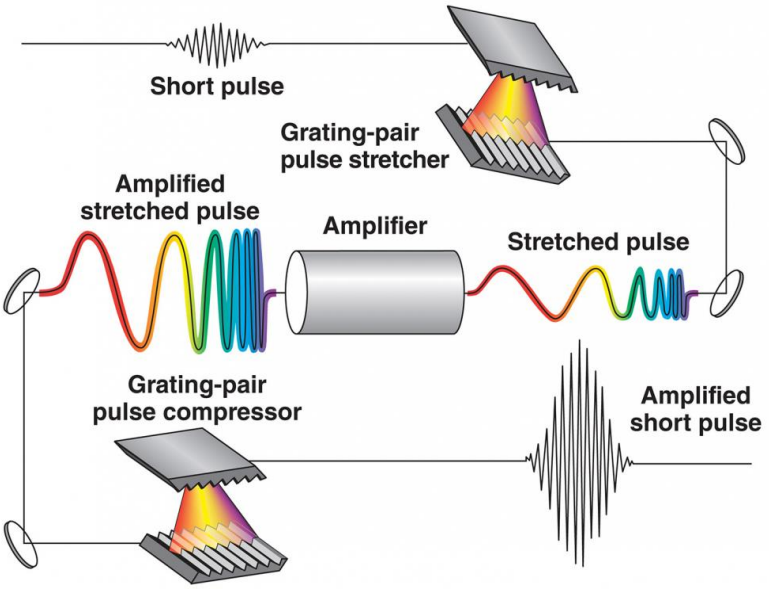


*Figure 1.1: Diagram illustrating chirped pulse amplification [9]*

Some laser gain media such as Ti:Sapphire lasers can overcome this limitation via transverse aperture scaling, enabling a 10-100 times additional increase in energy to >100J [10]. However, other laser types cannot achieve complete energy extraction by scaling transversely. For some laser gain media, such as Tm:YLF, the saturation fluence is higher than the laser-induced damage threshold of the material [11]. This means only a portion of the stored energy can be extracted from the amplifier with a single stretched pulse, limiting the efficiency and overall energy extraction. To overcome this, multiple pulses using temporal combining methods are required to reach complete energy extraction.

## 1.2 Fiber Chirped Pulse Amplification

Fiber chirped pulse amplification (FCPA) utilizes fibers to guide the laser pulse, and achieve high gain (40 dB) in an efficient manner. Solid-state lasers such as Ti:Sapphire generally have low wall-plug efficiency, and cannot scale to high repetition rates as thermal load management of the crystals become an issue. Fibers are much more efficient, with >50% wall-plug efficiency being demonstrated; however, they are limited in transverse aperture size by the

mode-field diameter of the fiber. Much work has been done to increase the core size of fibers while maintaining single-mode operation [12,13], but the extractable energy from a fiber amplifier is still limited. Nonlinear phase from the B-integral limits the extractable energy before the fiber damage threshold [14]. The equation for B-integral is given by Equation 1.1, and the nonlinearity-limited fluence $U_{\phi NL}$, the energy per unit area that can be extracted with a specific amount of nonlinear phase, is given by Equation 1.2. A value of $B = \pi$ is taken as the acceptable limit for nonlinear phase [14].

$$B = \frac{2\pi}{\lambda} \int n_2(z) I_{peak}(z) dz \tag{1.1}$$

$$U_{\phi_{NL} limited}(\tau) = U_{sat} g_0 L \left(1 - exp\left[\frac{-\phi_{NL}}{n_2 k_0 L U_{sat}} \tau\right]\right) \tag{1.2}$$

Figure 1.2 plots the damage threshold, available energy, and nonlinear phase limit for different pulse durations using either a 50 µm or 100 µm mode-field diameter fiber.

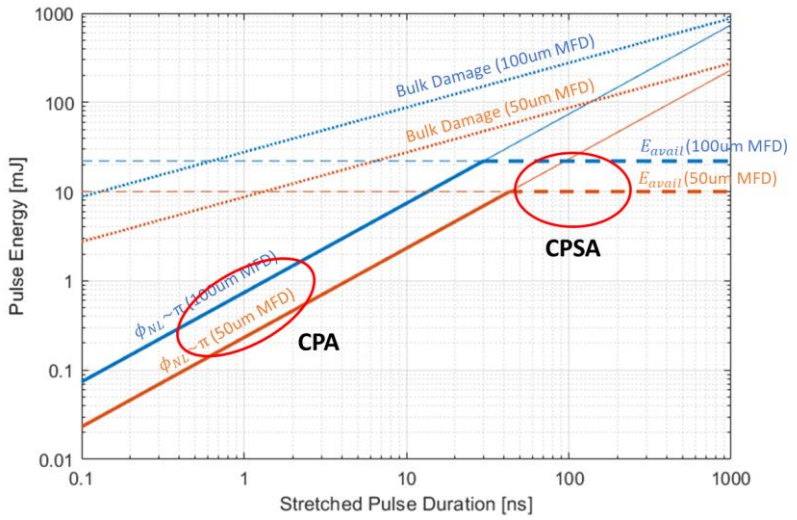


*Figure 1.2: Complete energy extraction from fiber amplifiers requires CPSA, courtesy of Alex Rainville [15]*

Using normal CPA methods to stretch the pulse to ~1 ns, the extractable energy from a fiber is limited to a couple hundred µJ due to nonlinear phase. To reach total energy extraction, the pulse duration needs to extend to ~100 ns, which would require gratings on the order of 10 meters in size, which is not feasible given current manufacturing limitations. Instead, coherent

temporal combining techniques can be employed to artificially extend the pulse duration. By amplifying a burst of stretched pulses, the peak power can be reduced proportionally to the number of pulses in the burst. Therefore, if temporal combining of ~100 pulses is used, complete energy extraction is possible, increasing the usable energy from fiber amplifiers. To do this, coherent pulse stacking amplification (CPSA) is utilized.

### 1.3 Coherent Pulse Stacking Amplification

Coherent Pulse Stacking Amplification (CPSA) is a temporal combining technique designed to extend CPA-provided stretched pulse durations by orders of magnitude [16]. This is accomplished by amplifying a burst of stretched pulses in an amplifier chain and then temporally combining them after the final amplifier, thus reducing the peak power in the amplifiers proportionally to the number of pulses in the burst. A basic diagram of a CPSA system is shown in Figure 1.3, where the key components of the technique are shown.

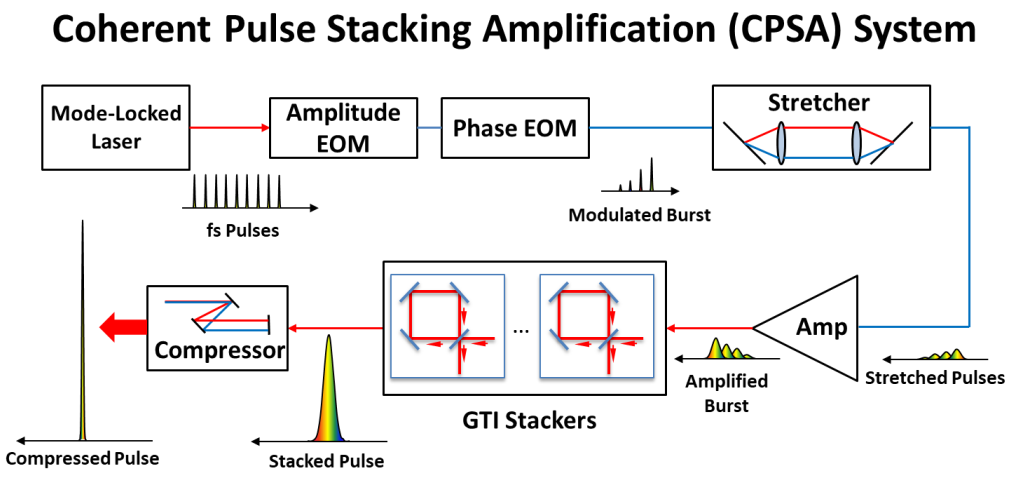


*Figure 1.3: Basic diagram for CPSA laser system*

CPSA begins with a mode-locked laser producing a train of pulses as the seed laser for the system. These pulses are then shaped into the stacking pulse burst using fast amplitude and phase electro-optic modulators (EOMs). This allows the user to prescribe the number of pulses in

the burst, the burst repetition rate, as well as the amplitude and phase of each pulse in the stacking burst. The burst can be pre-shaped as well, meaning after saturation effects in the amplifier chain, the burst will emerge with the proper shape for stacking [17]. After properly designing the burst, the pulses are stretched in a typical CPA stretcher. A series of amplifiers and acousto-optic modulators (AOMs) are used to increase the burst energy and decrease the burst repetition rate. After the final amplification stage, the burst is temporally combined into an effectively single-output pulse using a sequence of Gires-Tournois interferometer (GTI) stackers. This stacked pulse is then compressed, delivering a high-energy pulse. The design and adaptability of CPSA is further discussed in Chapter 2.

### 1.4 Other Coherent Temporal Combining Methods

Other coherent temporal combining methods exist, the most notable of which is divided-pulse amplification (DPA) [18], however this pulse combining technique cannot compensate the pulse burst B-integral when extracting most of the energy from the amplifiers. DPA can use N delay lines to combine $2^N$ equal-amplitude pulses, however the pulse burst shape can only be changed by modifying the half-wave plate angles, giving N controllable parameters for $2^N$ pulses. This means that DPA cannot extract stored energy with low nonlinearity and achieve high combining efficiency. A schematic demonstrating pulse dividing and combining in DPA is shown in Figure 1.4. First, an input pulse is split into multiple replicas by using a series of polarizing beamsplitters, half-wave plates, and delay lines. In the diagram shown, a single pulse is split into four sub-pulses via two delay lines. This pulse train goes through amplification stages, and is then recombined in a mirror setup of the division stage, and the phases of the delay lines are controlled to ensure proper temporal combining.

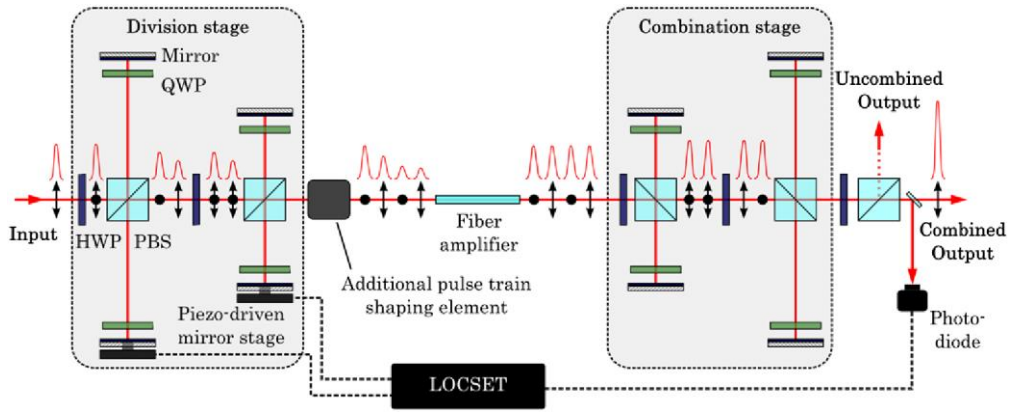


*Figure 1.4: Schematic for divided pulse amplification [19]*

DPA when implemented this way many limitations. In order to provide complete control of the input pulses, electro-optically controlled divided-pulse amplification (EDPA) was introduced [20]. This technique borrows from CPSA the use of electro-optic modulators (EOMs) to generate the input pulse train, enabling control of the amplitude and phase of each pulse. A schematic of an EDPA setup is shown in Figure 1.5 which is designed to generate a four-pulse train and recombine it into a single output pulse. This is accomplished by carving the pulse burst using either an acousto-optic modulator (AOM), or amplitude EOM, then splitting the pulse train into two orthogonal polarizations. Each polarization arm goes through a phase EOM, and then is recombined via a polarizing beamsplitters (PBS), allowing for polarization control of each pulse in the burst. The combining stage is similar to what was used in Figure 1.4.

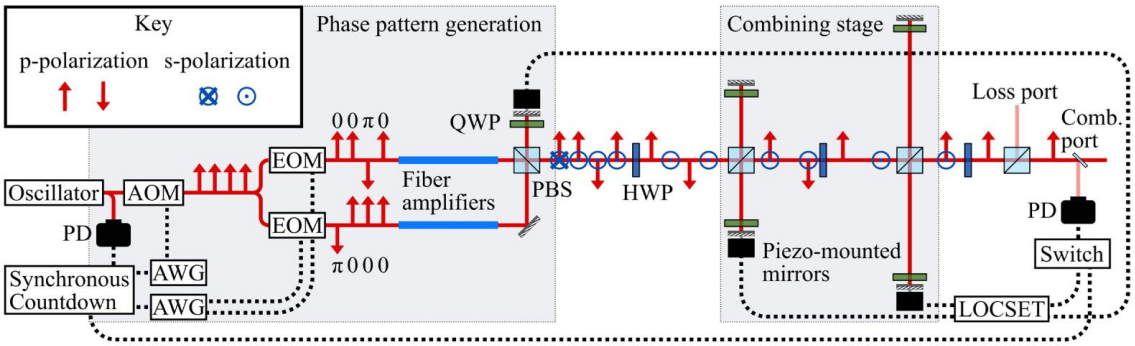


*Figure 1.5: Schematic illustration of the EDPA setup used for the combination of four temporally separated pulses from two channels. (PD: photo diode, AOM: acousto-optic modulator, AWG: arbitrary waveform generator, EOM: electro-optic modulator, QWP: quarter-wave plate, HWP: half-wave plate, PBS: polarizing beam splitter.) [20]*

EDPA solves many issues with divided-pulse amplification as a whole, and drastically simplifies the front-end of the system. However, there are limitations it still faces when operating at near-complete energy extraction. While the front-end now allows for better pre-shaping of the burst, the combining stage still has limited control of pulse burst shapes it can combine. Essentially, each delay line in the combining stage has a half-wave plate which can have its angle tuned to change the ratio of pulses it combines, meaning it can combine non-equal amplitude pulses [21]. However, since $N$ delay lines can combine $2^N$ pulses, there is a mismatch of degrees of freedom. The amplitude of each pulse entering the combining stage cannot be individually controlled and still be combinable, meaning the ideal burst shape for equal nonlinear phase in the amplifier cannot be used without significant efficiency degradation. Indeed, combining of four pulses can be well-utilized as the parameter mismatch is not too large [22], however when extended to eight pulses in the burst the efficiency suffers [23], and will continue to degrade with increasing number of pulses. Further discussion of equal-nonlinearity burst shapes and combining are discussed in Section 2.8.

In order to overcome this limitation, it is proposed to use the phase EOMs at the front of the system to apply a phase offset to some pulses in order to match the nonlinear phase at the output [20]. In theory this is a valid solution, but only if the chirped pulses in the amplifier have a perfect rectangular spectrum. Since chirped pulses map the spectral content to a temporal pulse profile, the nonlinear phase accumulated in an amplifier is given by equation (1.3), where $n_2$ is the nonlinear refractive index, $k_0$ is the wave vector, and $L_{eff}(\lambda)$ is the effective length of the fiber amplifier, determined by the inversion profile and pumping characteristics.

$$\phi_{NL}(\lambda) = n_2 k_0 I(\lambda) L_{eff}(\lambda) \tag{1.3}$$

Since the EOMs apply a roughly flat phase across the pulse, the spectrum must be flat-top in order to be able to fully compensate for the amplifier nonlinear phase mismatches. This effect becomes more pronounced the higher energy and longer burst duration is used.

### 1.5 Coherent Beam Combining

Even using coherent temporal combining to fully extract the energy from a fiber amplifier, the output energy is limited to the fiber's stored energy, which has been demonstrated to be >10 mJ [17]. In order to scale the energy further, coherent beam combining (CBC) is used. CSC splits a seed signal into many replicas, amplifies all of them in parallel, and then combines them into a single output. There are many different approaches to combining these parallel channels, such as using beamsplitters [15,23,24], diffractive optical elements [25,26], or tiled-aperture configurations [27,28]. With the use of CPSA, each of these methods can reduce the number of parallel channels required to reach a specific energy by ~100 times, as energy extraction is drastically increased. Simultaneous CPSA and CBC is demonstrated for the first time in this thesis work, and is described in Chapter 4.

### 1.6 Coherent Spectral Combining

In order to preserve the spectral bandwidth throughout the laser system and avoid gain narrowing effects, coherent spectral combining is used. This involves spectrally splitting an input into narrow-band pulses, amplifying each of these spectral channels in parallel, and recombining them in a spectral combiner [29–31]. A diagram showing this process can be seen in Figure 1.6.

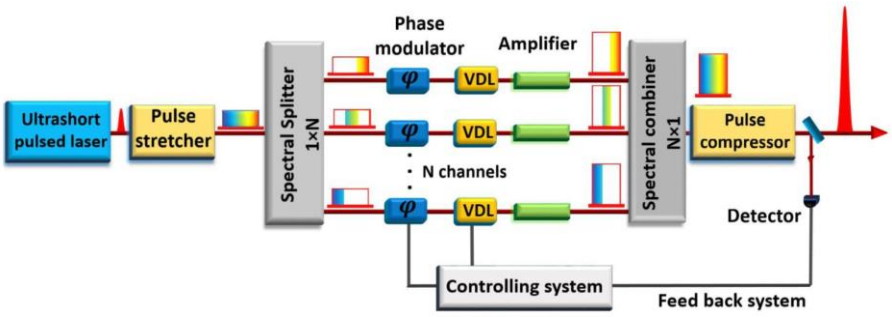


*Figure 1.6: Schematic showing coherent spectral combining system diagram [32]*

In addition to increasing the output pulse bandwidth, coherent spectral combining can also be leveraged to tailor output pulse shapes for specific applications via spectral shaping and phase control. Spectral synthesis of a flat-top, bandwidth-limited pulse for quasi-monoenergetic gamma photons via Thomson scattering is developed and demonstrated in this thesis. It is discussed in Chapter 5.

## 1.7 Applications of High Repetition Rate, High Energy Laser Sources

Multi-kHz laser sources with peak powers >100 TW are needed for many relativistic light-matter interactions. These interactions enable generation of neutron sources, x-rays [33], gamma rays [34], proton beams, or terahertz sources [35]. They are envisioned to eventually be used in linear laser plasma accelerators (LPAs), a diagram of which is shown in Figure 1.7 [36–38]. These laser sources require 1-50 kHz repetition rates, with pulses delivering >1 Joule of energy and pulse durations below 100 fs.

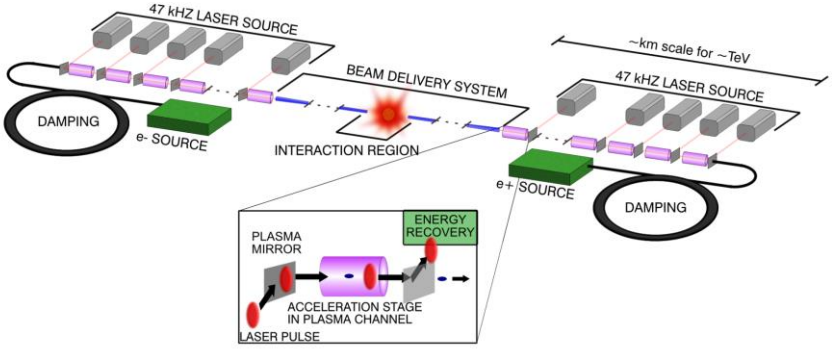


*Figure 1.7: Schematic of an LPA-based linear collider [37]*

Lasers providing these parameters will have average powers well-beyond 10 kW, meaning wall-plug efficiency is a crucial parameter. This is well suited to fiber lasers, which have high wall-plug efficiencies. Energy scaling can be achieved using the coherent combining techniques previously discussed in this chapter, requiring temporal combining of ~100 pulses and spatial combining of ~1000 parallel fiber amplifiers. We demonstrate proof-of-principle operation of these coherent combining methods, showing the scalability of the technique.

### 1.8 Overview of thesis work

CPSA has been proposed in [16], and stacking of up to 81 pulses has been demonstrated in [14]. Using these techniques, an 81-pulse burst was amplified to 10 mJ and stacked into a single pulse by John Ruppe and Hanzhang Pei [14,39]. This thesis work further develops the CPSA technique, both in its understanding and implementation. Using these newly developed aspects, simultaneous coherent beam combining and CPSA is demonstrated for the first time, where a 25 mJ burst is combined spatially from four parallel fiber channels and stacked into a single output pulse.

Specifically, the thesis reports on the following advances: CPSA was shown to be a physical implementation of a deep recurrent neural network, and analysis was done on stacking

performance when pulse burst shapes are changed and errors are applied to stacker parameters. The results of this analysis as well as methods to adaptably compensate these errors are discussed in Chapter 2. Additionally, quantification of cavity alignment tolerances was developed, and techniques to ensure the meeting of the calculated tolerances were implemented. This allows for robust, repeatable stacking performance, which is discussed in Chapter 3. These techniques were then applied at near total energy extraction, where simultaneous coherent beam combining and CPSA was demonstrated with minimal stacking efficiency degradation. A description of the system used as well as reporting of the results is covered in Chapter 4. Lastly, methods of using coherent spectral combining to synthesize pulse shapes specifically tailored for generation of quasi- monoenergetic gamma photons via Thomson scattering were developed and implemented. The methods developed and the results found are reported in Chapter 5.

# Chapter 2 Adaptable Nature of Coherent Pulse Stacking Amplification

## 2.1 Introduction

Coherent pulse stacking uses a series of Gires-Tournois Interferometer cavities to stack a burst of input pulses into a temporally combined output pulse. Stacking must achieve both high efficiency, $\eta$, and pre-pulse contrast, $\chi$. This is crucial for laser-plasma applications, as pre-pulses can distort the plasma and degrade the performance [40]. Additionally, when operating at high energies in fiber amplifiers, equal nonlinearity burst shapes must be used instead of equal-amplitude bursts, which require optimization of stacker design and stacking performance to accommodate these profiles. Lastly, errors on stacking parameters can degrade performance, and must therefore be quantified and controlled to acceptable tolerances.

This chapter investigates how to achieve high pre-pulse contrast, as well as how equal-nonlinearity burst shapes and parameter errors impact both stacking efficiency and pre-pulse contrast.

## 2.2 Coherent Pulse Stacking Using Gires-Tournois Interferometer Cavities

A stacking system is comprised of a cascaded-in-series Gires-Tournois Interferometer (GTI) cavity set. A diagram of such a cavity is shown in Figure 2.1. Each cavity contains a partially reflecting mirror, whose reflectance is denoted as $r$ for field reflectance and $R$ for intensity reflectance, where $R = \sqrt{r}$. From this value, we can calculate the mirror transmission, denoted as $T = 1 - R$ for intensity transmission and $t = \sqrt{1 - r^2}$ for field transmission. All other mirrors in the cavity should be high reflectance mirrors, with $R \approx 1$. Additionally, the GTI

has a round-trip time $\tau_{rt}$, which corresponds to the optical path length inside the cavity. For stacking purposes, this round-trip time should correspond to the repetition rate of the pulses within the burst $f_{rep}$, specifically $\tau_{rt} = m * \frac{1}{f_{rep}}$ where m is some integer number greater than or equal to 1. This ensures that after the cavity delays the laser pulse inside it, the delayed pulse properly interferes with other pulses from the burst. However, this round-trip time must also have a sub-wavelength timing mismatch $\tau_\delta$ with the repetition rate, which corresponds to a phase shift $\phi = 2\pi\delta = 2\pi\frac{\tau_\delta c}{\lambda}$ that pulses accumulate after each roundtrip in the cavity. This phase affects interference between pulses incident upon the partial reflectance mirror, and is therefore an important stacking parameter for design and control.

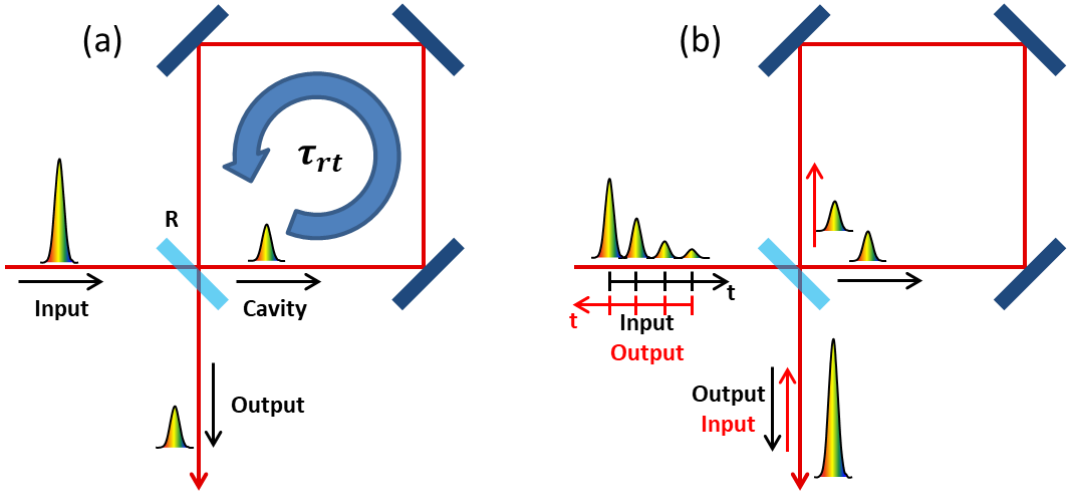


*Figure 2.1: (a) Diagram of GTI cavity with reflectivity R and round-trip time $t_{rt}$ , (b) Impulse response of cavity is time-reversible and gives optimal stacking input*

Using this, we can analyze an incident pulse with electric field $E_{in}$, which when incident upon the partial reflector will generate a cavity pulse with electric field $E_{cav} = E_{in} * it$ and an output pulse $E_{out} = E_{in} * r$.

If the cavities are assumed to have no loss or gain, i.e. the high reflectance mirrors have a value $R = 1$ and the cavity is passive, then the GTI cavity can be considered to be a linear time-

invariant (LTI) system [14]. This means the system is time-reversible, and what is obtained at the output can be sent back (after time-reversal and complex-conjugation) through the cavity to recreate the input. This is valuable for cavity design, as the impulse response of the cavity can be calculated to determine what the optimal input waveform should be to achieve stacking, as seen in Figure 2.1 (b). By propagating a single pulse through, the optimal input waveform is found, containing both pulse amplitude and phase. Additionally, since the pulse burst has a fixed repetition rate and mode-locked pulses can be treated as identical to one another, we can simulate this process using discrete time, where we only need to consider pulse amplitude and phase, and where the time step corresponds to the repetition rate of the pulses. Equation 2.1 shows the impulse response of a single cavity using this discrete time approach, where $n$ corresponds to the output pulse number, starting with $n = 1$.

$$E_{out}^{n} = \begin{cases} E_{in} * r & for\ n = 1 \\ -E_{in} * t^2 * r^{n-2} * e^{i\phi * n} & for\ n > 1 \end{cases} \tag{2.1}$$

To extend the number of pulses that can be stacked, multiple cavities can be used, where the output from one is the input to the next. An example configuration can be seen in Figure 2.2 (a), where three GTI cavities can be used to stack 7 input pulses into a single output pulse, using mirror reflectance and phase values shown in the figure. Since each cavity provides two degrees of freedom, in general $N$ cavities can stack $\sim 2N$ pulses with proper parameter selection. This means extending the pulse burst length to 100 pulses would require ~50 equal-length cavities, which is technically daunting. In order to overcome this, a mixture of cavity lengths can be used.

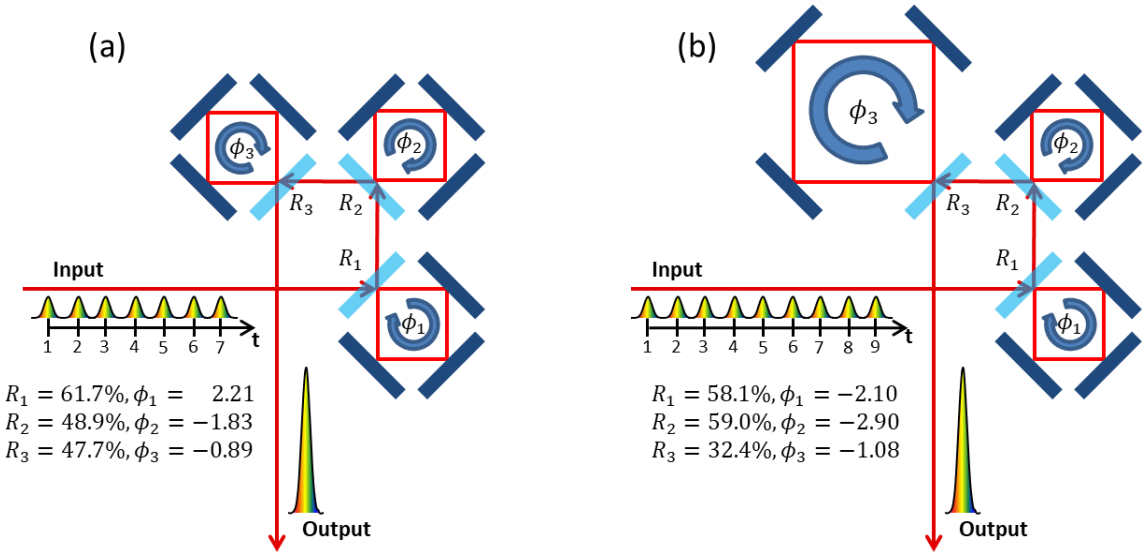


*Figure 2.2: (a) 3-GTI equal-length cavity set, able to stack 7 pulses, (b) 2+1 GTI cavity set, with two cavities with length equal to the pulse repetition rate and one cavity length twice the pulse repetition rate*

Shown in Figure 2.2 (b) is an example of multiplexing using three cavities. Two cavities, labeled 1 & 2, have round-trip length equal to the pulse repetition rate, and the third cavity labeled 3 has a round-trip length equal to twice the pulse repetition rate. This stacker configuration can be labeled 2+1, '2' indicating the number of shorter cavities, and '1' indicating the number of longer cavities. By increasing the size of one of the cavities, the number of stackable pulses increases from 7 to 9. Reflectance and phase values to achieve this are given in the figure. By using different lengths of cavities, a large numbers of pulses can be stacked with a small number of cavities, enabling scaling of CPSA to large pulse burst durations. Using multiplexing, a general rule-of-thumb is that $M$ pulses requires the stacker system to have a total round-trip length (i.e. the sum of all cavity round-trip lengths) of at least $L_{total} = \frac{M*\tau_{rep}}{2}$.

### 2.3 Stacker System Design

Proper parameter selection of cavity reflectance and phase is crucial to designing a stacker system. However, for a large number of cavities, all values in the parameter space can't

be tested as this is computationally prohibitive. To simply test 10 values for each parameter in an eight-cavity stacker, assuming each point takes 1 μs to calculate, would take $10^{16} * 1\mu s = 317\ years$. Therefore, other methods to find optimal parameters must be employed.

First, a merit function must be defined, which determines how well a given stacker system performs. When designing a cavity set, the first consideration is the efficiency of stacking, which is used as a merit function. The process for determining how well a cavity set performs is shown in Figure 2.3 for the 9-pulse stacker shown in Figure 2.2 (b). First, the impulse response of the cavity set is calculated. However, in general there is a desired input amplitude profile, which in this example is equal-amplitude. Therefore, we can change the amplitudes of the impulse response to the desired shape while keeping the phase values, and propagate this back through the stacker system after time-reversal and complex-conjugation. This results in a stacked pulse with an efficiency $\eta$, defined in Equation 2.2, where $I_{stacked}$ corresponds to the stacked pulse intensity, and $I_{out}^{n}$ is the intensity of the n[th] output pulse. This is then used to define the merit function as $Error = 1 - \eta$, which is minimized to determine optimal cavity parameters.

$$\eta = \frac{I_{stacked}}{\sum_1^N I_{out}^n} \tag{2.2}$$

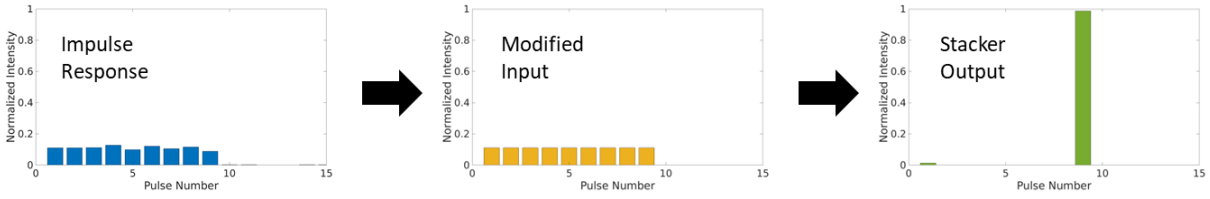


*Figure 2.3: Process of determining stacker performance by impulse response calculation*

Now that stacking performance can be quantified, the parameter space must be sampled. To do this, a Monte Carlo method is performed that randomly samples the parameter space. After enough values have been tested, the best cavity values are each optimized using an

optimization algorithm. For this, I employed a Nelder-Mead method that uses a simplex to find the optimal values, however many other methods can be used. It is possible to change the merit function and optimization process, however we have found that this approach works best to find a starting set of cavity parameters that can be further optimized or modified as needed.

### 2.4 Cavity Phase Search & Stabilization

Once the proper reflectance and phase values have been determined for a given cavity set, they need to be achieved. Mirror reflectance values can be guaranteed by a manufacturer to some specification, with tolerances further discussed in Section 2.9, however phase values for cavities need to be determined and maintained. Measuring the phase of each cavity to ensure it has the proper value is cumbersome, and unnecessary. Instead of looking at the phases of the cavities, we can instead look at the stacking efficiency and maximize the values in this way, since we know the proper phase values result in optimal stacking.

Since the cavities are passive delay lines, the average power of the burst does not change with cavity phase changes. Instead, we need a peak detection method as a feedback metric. This can either be a fast photodiode that reads the pulse burst and returns the stacked pulse intensity, or second harmonic generation (SHG), which has intensity $I_{2\omega} = n_2 I_{\omega}^2$, so it is sensitive to changes in peak power. Other metrics are also possible to use, however it must have either a global maximum or minimum that corresponds to the optimal stacking position. This metric can then be maximized or minimized to find and maintain the optimal stacking cavity phases.

In order to maximize stacking, some kind of algorithm is required to interpret the feedback metric and update the cavity phases accordingly. For this, stochastic gradient descent methods are well-suited. They randomly sample the parameter space around the current point, approximate a gradient from this, and use the gradient to determine the updated values. These

methods are model-free, meaning they do not know what the landscape looks like, and simply hill-climb to find the local maximum/minimum.

This is good to find and keep the optimal stacking position, but only if the algorithm starts sufficiently close to the global maximum. Otherwise, the algorithm can get stuck at a local maximum, and not achieve the desired stacking performance. In order to overcome this, a scan of the multi-dimensional parameter space is needed. In order to move the phases in a smooth, harmonic fashion we employ a technique called Lissajous scanning [41]. With properly chosen parameters of the Lissajous scan, the cavity phase space is sampled such that the global maximum peak is found, and once sufficiently close the stabilization algorithm turns on. Once the algorithm takes over, it climbs to the maximum stacking position and actively stabilizes cavity phases.

### 2.5 Coherent Pulse Stacking as a Deep Recurrent Neural Network

In the process of better understanding stacking cavities and how to properly design them, it was found that GTI cavity can be mathematically described as a physical implementation of a recurrent neural network. A recurrent neural network (RNN), shown in Figure 2.4, takes an input $x_t$ and a previous value from itself $c_{t-1}$, and from this calculates an output $o_t$ and its next value $c_t$. For pulse stacking, these values correspond to pulses, each with an amplitude and phase value. The GTI cavity layer $H_m^{(N)}$ corresponds to the $N^{th}$ cavity during the $m^{th}$ time-step.

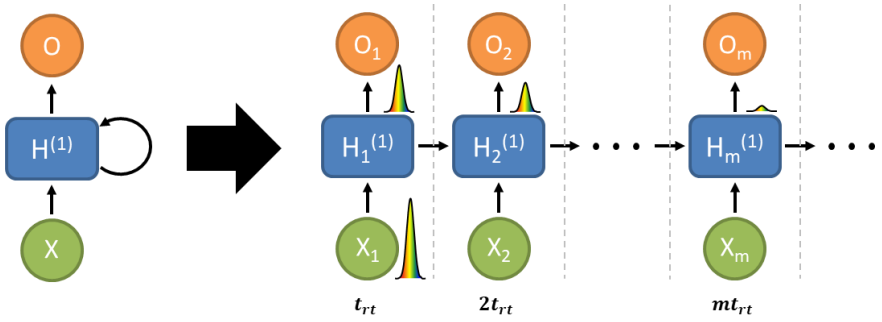


*Figure 2.4: GTI cavity as recurrent neural network with impulse response*

An equivalent layout unfolded in time is shown on the right, with an impulse response calculation being shown. Here, the GTI cavity corresponds to a computational unit shown in Figure 2.5, with weights and connections detailed in equations shown to the left of the unit. The time-dependent input and output correspond to the input and output pulse bursts, and the self-connection is the delayed cavity pulse. In this way, a GTI is equivalent to a RNN.

$$W_r = r$$
$$W_t = it = i\left(\sqrt{1-r^2}\right)$$
$$W_\phi = e^{i\phi}$$
$$\boldsymbol{o_t} = W_r \boldsymbol{x_t} + W_t \boldsymbol{c_{t-1}}$$
$$\boldsymbol{c_t} = W_\phi (W_r \boldsymbol{c_{t-1}} + W_t \boldsymbol{x_t})$$

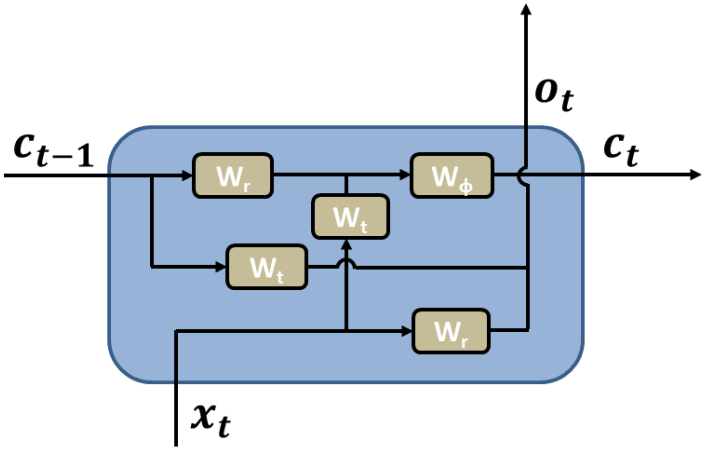


*Figure 2.5: RNN computational unit corresponding to GTI cavity*

When multiple cavities are used to form a stacker system, such as the one in Figure 2.2 (a), this corresponds to more layers in the neural network, forming a deep recurrent neural network (DRNN). A DRNN representation of the 3-cavity system discussed is shown in Figure 2.6, in which a 7-pulse input burst is being stacked into a single output pulse. Each cavity is an

additional hidden layer, and its computational cell feeds its output into the input of the next, just as a stacker system cascades GTI cavities.

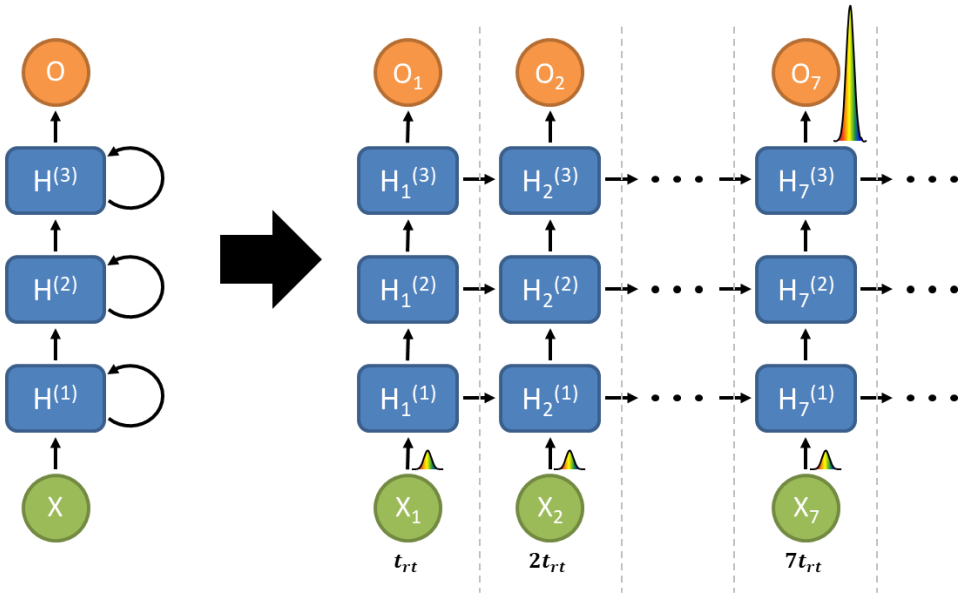


*Figure 2.6: 3-GTI stacker as deep recurrent neural network stacking 7 pulses*

Additionally, multiplexing lengths of cavities can also be cast in the DRNN framework. This does not change any of the computational cell structures, but does modify how the DRNN connects. An example of this can be seen in Figure 2.7, which models the 3-cavity multiplexed case shown in Figure 2.2 (b). In this case, the information that a layer passes on to itself is delayed further in time, corresponding to the length of the GTI cavity. With this additional piece, any given stacker system can be cast as a DRNN, with both being mathematically equivalent.

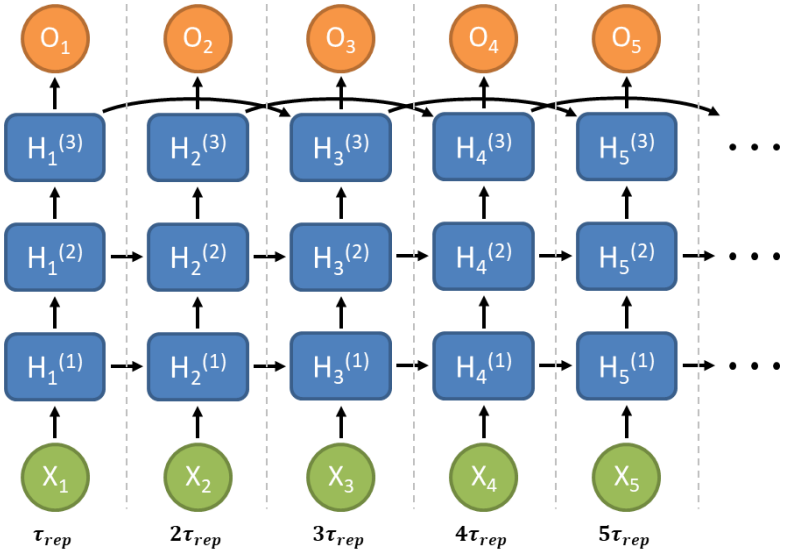


*Figure 2.7: DRNN with multiplexed lengths*

Now that it has been shown that a GTI-cavity set is a physical implementation of a DRNN, it can be seen that cavity parameter selection discussed in Section 2.3 is essentially training a neural network. Back-propagation algorithms are used to tune the weights of the neural network, which in this case correspond to the cavity reflectivity and phase, to have the system behave as desired. This is the same thing that is done when designing a cavity set, where a desired output is propagated in reverse through the system, and is used to tune the cavity parameters. Additionally, stabilization of cavity phases discussed in Section 2.4 is training the network in real-time, where weights are updated as required based on the current state output.

## 2.6 Experimental Stacking System

Our experimental stacker system consists of a 4+4 multiplexed GTI configuration, shown in Figure 2.8. This configuration is designed to stack an 81-pulse burst into a single output pulse. This design uses four cavities that have round-trip length equal to $\tau_{rt}$, which can stack 9 pulses. This will stack the incident 81-pulse burst into 9 pulses, each separated by $9 * \tau_{rt}$. Then, the other four cavities have round-trip length equal to $9 * \tau_{rt}$, which stack the remaining 9 pulses

into a single pulse. Each cavity has a mirror reflectance $R = 0.57$, as this simplifies the design substantially when ordering custom coatings while having minimal degradation of stacking performance.

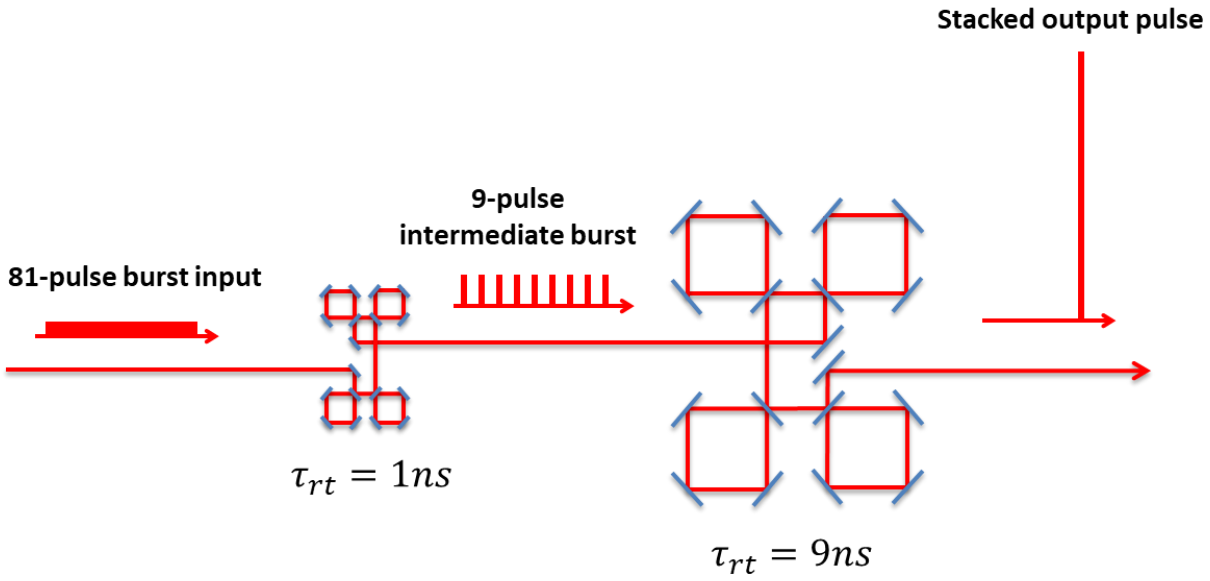


*Figure 2.8: Experimental configuration of 4+4 GTI stacker system stacking 81 pulses*

These stackers are integrated into a CPSA system shown in Figure 2.9. Here, the repetition rate of our fiber oscillator $f_{rep} = 1\,GHz$, and when carved by the electro-optic modulators (EOMs) our burst has a repetition rate $f_{burst} = 1\,MHz$. We have implemented a field-programmable gate array (FPGA) to control the system synchronously, and it is the backbone of stacking operation. It is used to apply the proper amplitude and phase profiles to the EOMs to create the proper stacking burst, and to later down-count the burst repetition rate using acousto-optic modulators (AOMs). It also controls the cavity tilts, timing, and phases, and reads the stacking burst for stabilization and diagnostics.

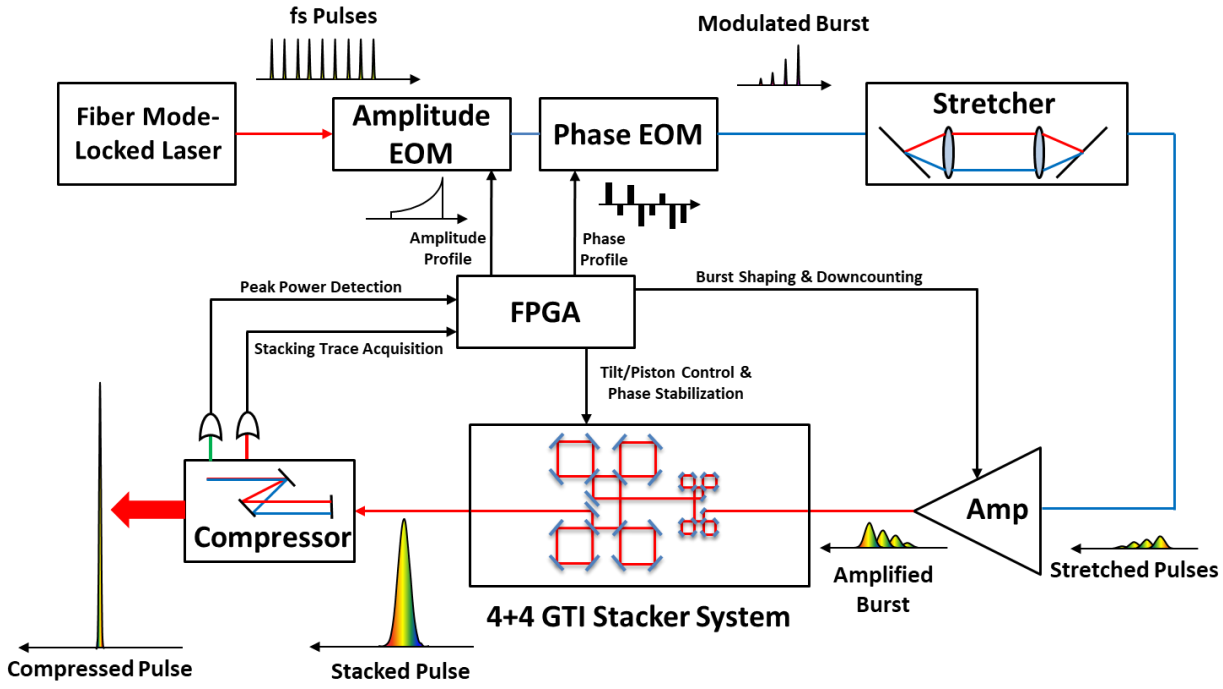


*Figure 2.9: Experimental CPSA system diagram for 4+4 stacking of an 81-pulse burst*

This stacker design is simulated to stack an 81-pulse input, which is shown in Figure 2.10. Theoretically, it has a stacking efficiency $\eta = 98.1\%$.

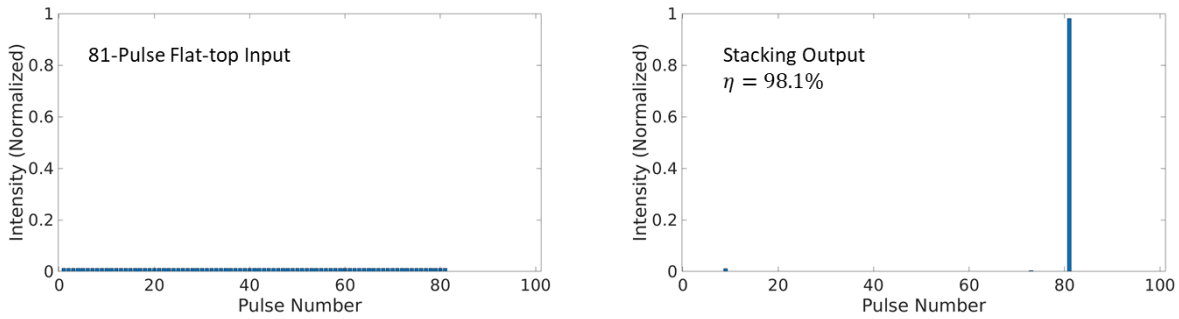


*Figure 2.10: Simulated stacking of 81 equal-amplitude pulses using experimental GTI configuration*

## 2.7 Achieving Higher Pre-pulse Contrast via Post-Pulses

In Section 2.3, the merit function concerned itself only of the stacking efficiency achieved. However, another key aspect of stacking performance is pre-pulse contrast, defined in Equation 2.3, which is the ratio of the stacked pulse to the largest pre-pulse intensity. Pre-pulses are defined as any pulse that arrives before the stacked pulse.

$$\chi = \frac{I_{stacked}}{\max_{0<n<N} I_{out}^{n}} \tag{2.3}$$

This is a very important parameter, as many laser-plasma interactions require a high pre-pulse contrast, between 20 dB and 40 dB [40]. However, the stacking shown in Figure 2.10 only has a pre-pulse contrast of $\chi = 19.3\ dB$, limited by the 9th pulse. Pre-pulse contrast can be improved by using a pulse pre-burst, which is shown in Figure 2.11. This involves using a number of pulses before the main burst which contain much less energy, but allow for higher achievable efficiency and pre-pulse contrast.

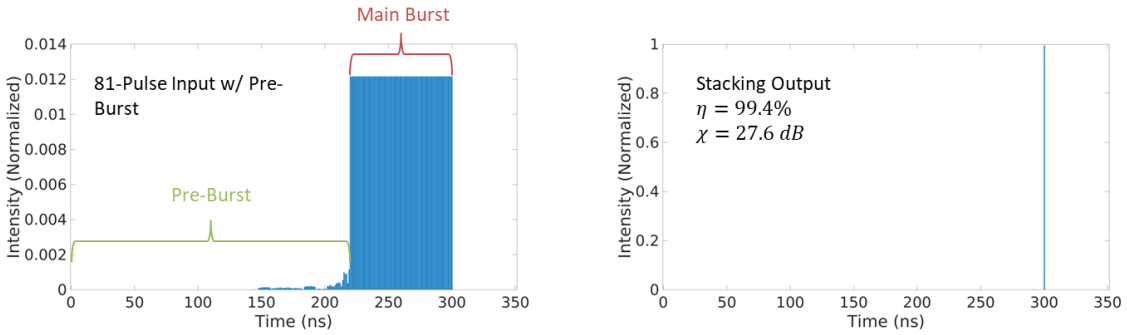


*Figure 2.11: 81-pulse input with pre-burst for better stacking, with stacked output on right*

Using a pre-burst before the main burst improves efficiency to $\eta = 99.4\%$ and pre-pulse contrast to $\chi = 27.6\ dB$. This is a substantial improvement, however pre-pulse contrast is still not as high as desired. This limitation of pre-pulse contrast arises from the fact that the amplitudes of the main burst are fixed in value, and the optimization method outlined in Section 2.3 focuses on maximizing efficiency. Instead, if pre-pulse contrast is focused on, changes to the merit function must be applied.

A method was proposed to increase pre-pulse contrast at the cost of efficiency by allowing energy to go into the post-pulses. Laser-plasma interactions generally do not care about energy after the main interaction, and therefore post-pulses will not have a detrimental effect on experimental applications. Previously, for finding optimal cavity parameters, the impulse

response of the cavity set was calculated. Instead, we can use an "augmented" impulse response, which uses small pulses before the impulse response is calculated. This, time-reversed, corresponds to post-pulses. So instead of looking for complete energy extraction, the cavities store all of the input burst energy and then the final pulse comes through to extract nearly all of the energy stored, but not all. Then the remaining pulses inside the cavities rattle down as post-pulses.

This of course requires a new metric, which is defined in Equation 2.4 and was developed by John M. Ruppe III [42]. $I_{ideal} - I_{aug}$ corresponds to the difference between each pulse in the augmented impulse response and the ideal main burst shape, and calculates the mean-squared error from this. This value should be minimized for maximum pre-pulse contrast. $I_{cavs}$ corresponds to the intensities of the post-pulses remaining in the cavities after stacking, which should be minimized for maximum stacking efficiency. Lastly, $\alpha$ is a tunable weight parameter that ranges from 0 to 1. This allows control of how much efficiency to sacrifice for pre-pulse contrast, essentially acting as a tunable knob between the two.

$$Error = (1-\alpha)\sum\left(I_{ideal} - I_{aug}\right)^2 + \alpha\sum(I_{cavs})^2 \tag{2.4}$$

By exploring different values of $\alpha$, we can generate a tradeoff curve of efficiency to pre-pulse contrast, which is shown in Figure 2.12. Using the experimental 4+4 GTI setup described in Section 2.6 using reflectance values $R = 0.57$ for all cavities, the pre-pulse contrast tradeoff can be seen following the blue points. The orange points change one longer cavity in the 4+4 configuration to have a reflectance value of $R = 0.75$, and keep all the rest at $R = 0.57$. Lastly, the yellow points vary the reflectance of each cavity to its optimal point, which gives insight on best possible performance.

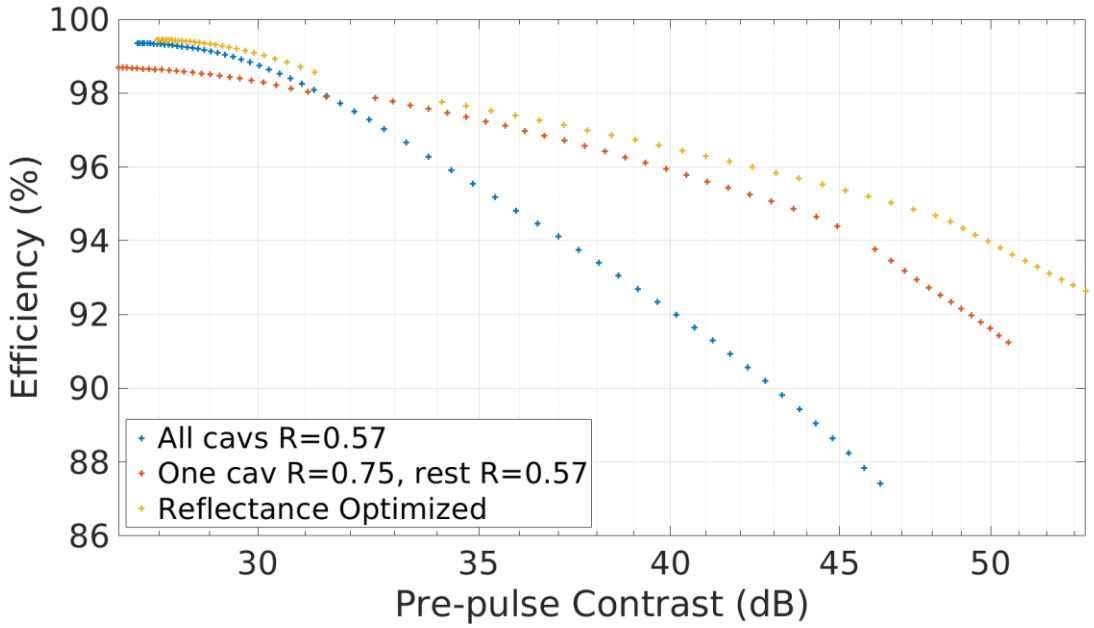


*Figure 2.12: Efficiency tradeoff with pre-pulse contrast for 81-pulse stacking using 4+4 stacker, blue points use R=0.57 for all cavities, orange points use R=0.75 for one cavity and R=0.57 for other seven, and yellow points optimize cavity R values*

In order to achieve a pre-pulse contrast of $\chi = 40\ dB$, the efficiency must drop to $\eta = 92\%$. This specific stacking scenario can be seen in Figure 2.13.

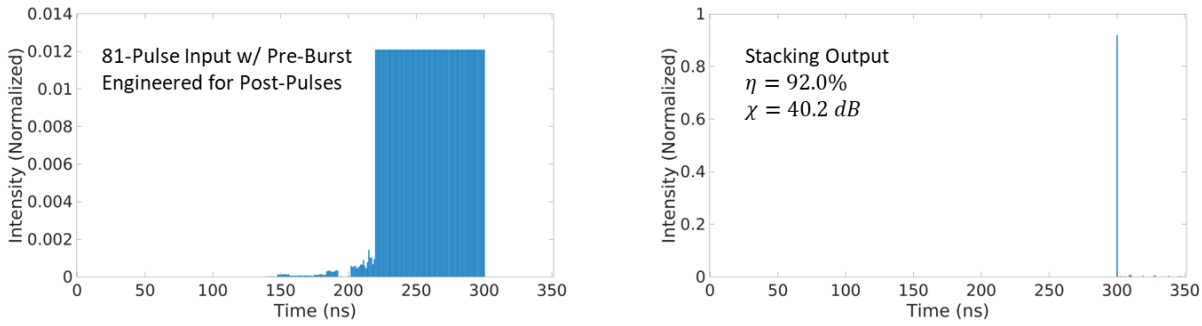


*Figure 2.13: Simulated stacking for 40dB pre-pulse contrast using 4+4 GTIs all with reflectance R=0.57*

When analyzing pre-pulse contrast to this high of a value, it is often more useful to look at the stacking output on a logarithmic scale. The stacking output for both the pre-burst waveform optimized for efficiency and the pre-burst waveform designed for 40 dB pre-pulse contrast are plotted in Figure 2.14. As can be seen, pre-pulses are substantially suppressed when post-pulses are allowed to occur, however stacking efficiency suffers.

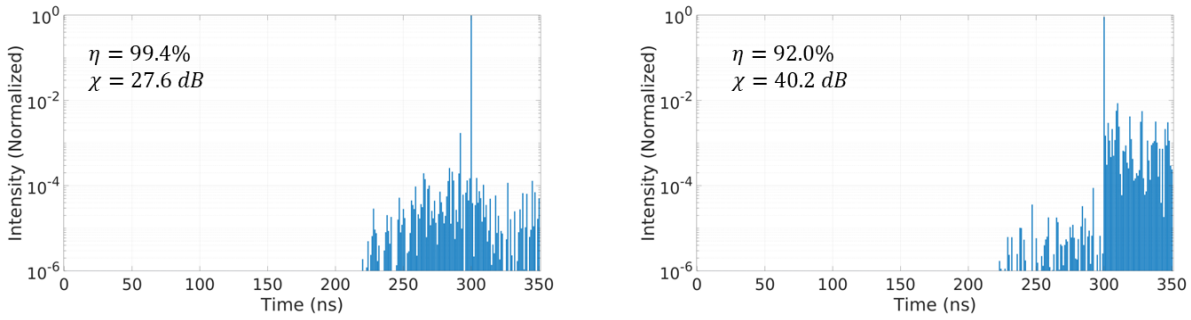


*Figure 2.14: Different pre-pulse tradeoff stacking outputs plotted on a logarithmic scale*

## 2.8 Adapting to Different Input Pulse Burst Shapes

Many stacking scenarios do not want to use equal-amplitude input pulse bursts, and instead wish to shape them for their application. For example, when amplifiers are operated at high energy, a flat-top burst will have very high nonlinear phase at the end of the burst, and each pulse in the burst will have different nonlinear phase. This can be seen in Figure 2.15, where the nonlinear phase shift is expressed as a B-integral

$$B = \frac{2\pi}{\lambda} \int n_2 I(z) dz$$

Instead, the burst must be shaped such that each pulse in the burst accumulates the same nonlinear phase, which means stacking needs to be able to accommodate non-equal-amplitude input burst shapes.

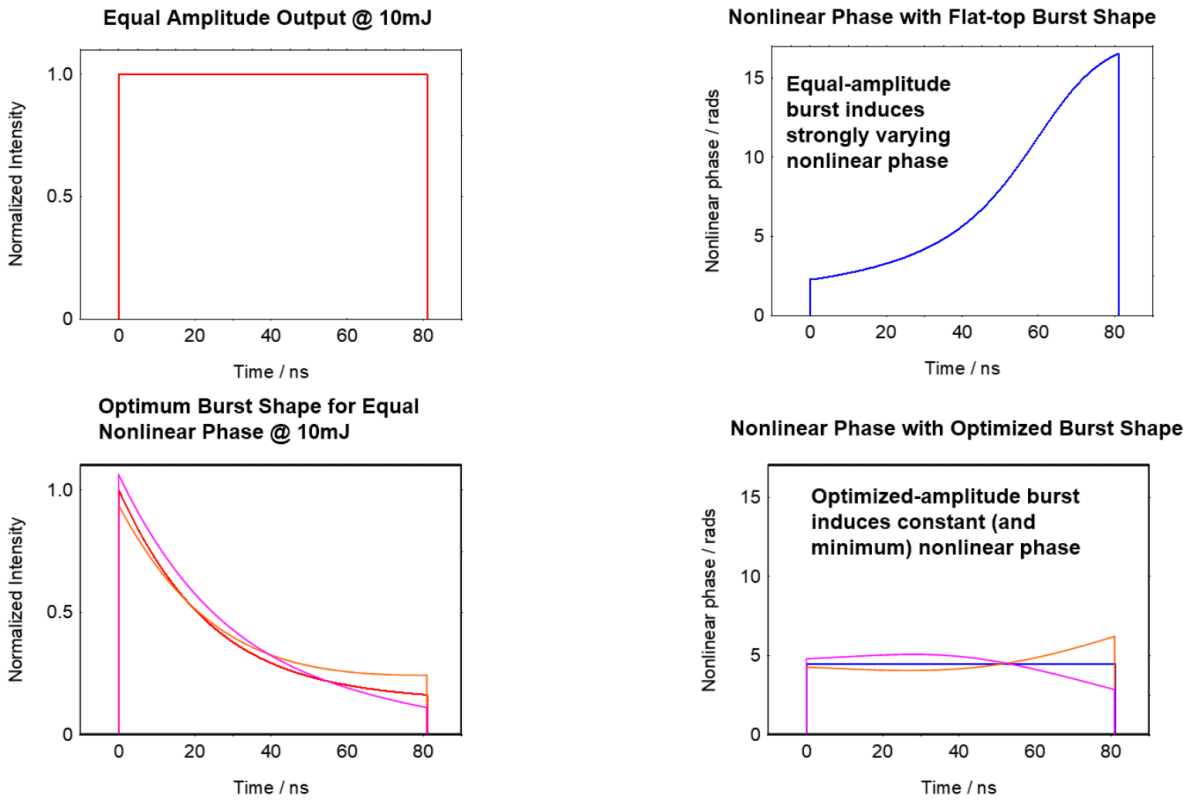


*Figure 2.15: Optimal input pulse burst shape for equal-nonlinearity [39], pink and orange curves represent deviation from the optimum burst shape, resulting in non-flat nonlinear phase across the burst*

Stacking using the experimental 4+4 stacker system is shown in Figure 2.16. The input burst is an equal nonlinear phase profile with nonlinear phase $\phi_{NL} = \pi$. The stacking efficiency drops from 99.5% to 95.4%, and pre-pulse contrast from 27.6 dB to 20.2 dB. Stacking performance decrease is expected; the input burst shape is far from the ideal flat-top profile, however with a large degree of saturation, the stackers are still able to stack fairly well.

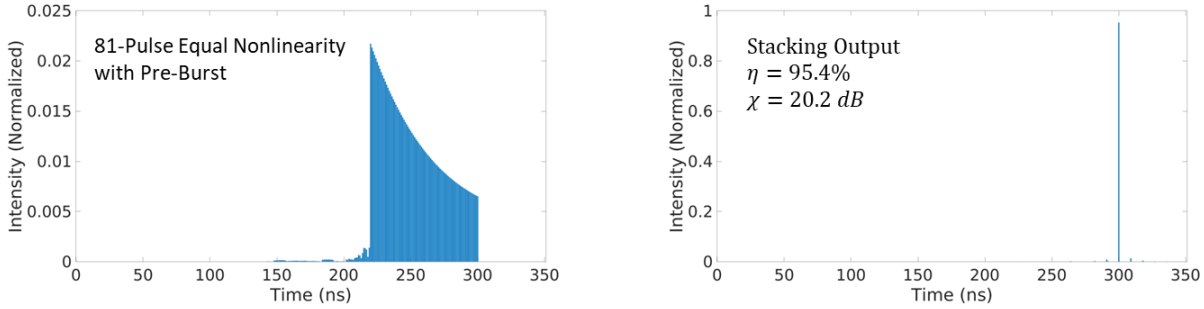


*Figure 2.16: Equal nonlinear phase burst shape stacked with a pre-burst, optimized for efficiency*

However, as discussed in Section 2.7, we can trade-off stacking efficiency for pre-pulse contrast by allowing post-pulses. A plot of the efficiency vs. pre-pulse contrast for the equal nonlinearity burst input is shown in Figure 2.17.

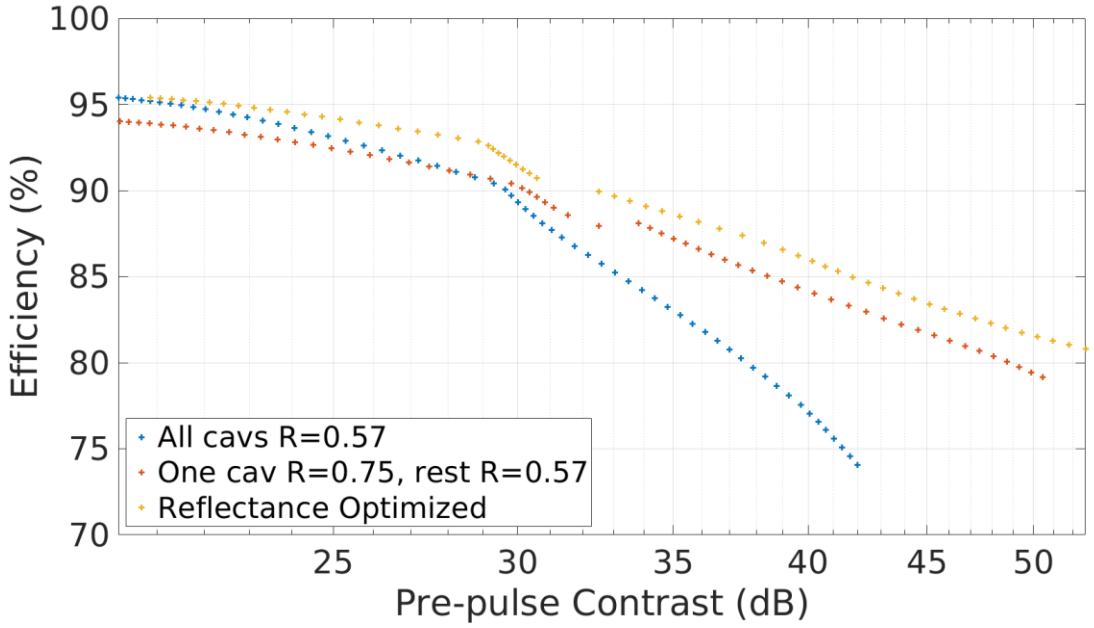


*Figure 2.17: Efficiency tradeoff with pre-pulse contrast for 81-pulse stacking using 4+4 stacker with equal nonlinear phase input burst, blue points use R=0.57 for all cavities, orange points use R=0.75 for one cavity and R=0.57 for other seven, and yellow points optimize cavity R values*

Once again, we can tune how much efficiency we are willing to sacrifice in order to achieve higher pre-pulse contrast. From the graph, we can see that to obtain a pre-pulse contrast of 30 dB, the efficiency will drop to 89.3%, a decrease of 6%. This stacking scenario is shown in Figure 2.18. Beyond 30 dB pre-pulse contrast, there appears to be a roll-off, and the slope of efficiency vs. pre-pulse contrast gets much steeper. This means to achieve 40 dB pre-pulse contrast, the efficiency degrades to 77.1%. This is a large tradeoff, however the option to get higher pre-pulse contrast still exists. The maximized efficiency and 30 dB pre-pulse contrast stacking scenarios are plotted on a logarithmic scale in Figure 2.19.

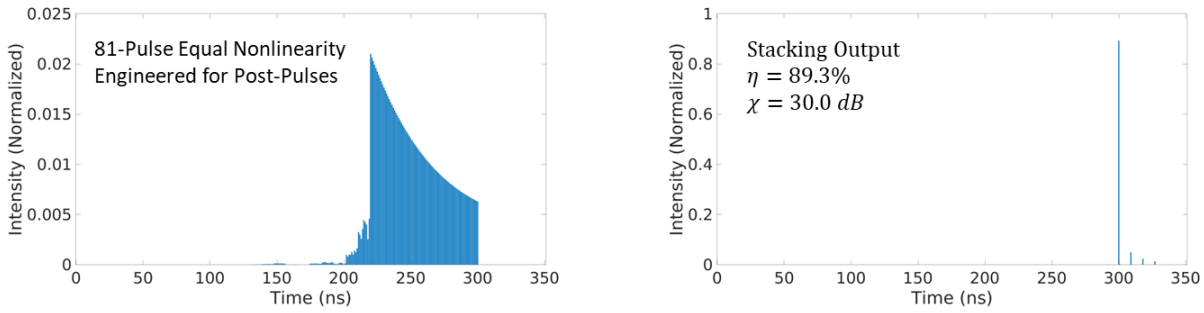


*Figure 2.18: Simulated stacking for 30dB pre-pulse contrast using 4+4 GTIs all with reflectance R=0.57 and a main burst amplitude profile for equal nonlinear phase*

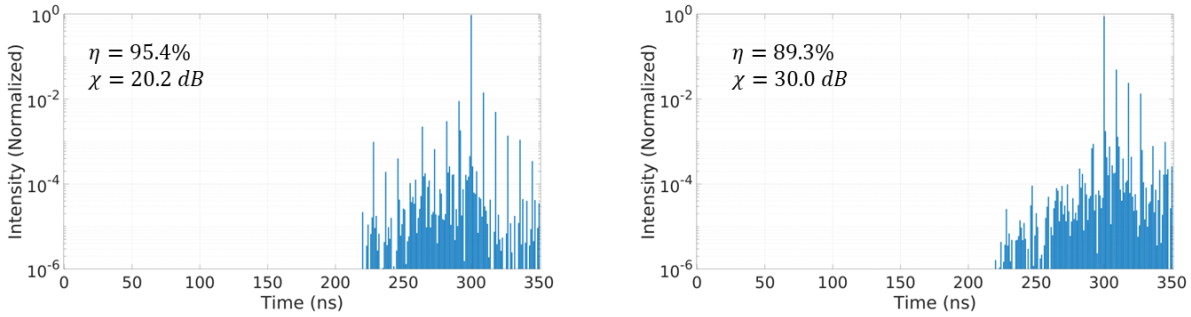


*Figure 2.19: Different pre-pulse tradeoff positions for equal nonlinear phase stacking*

## 2.9 Stacking Parameter Error Analysis & Pulse Phase Optimization

Up until now, design of a stacker system has assumed the ability to exactly prescribe the values of each pulse and cavity parameter. However, in real systems, there are uncertainties in these values, and their exact specifications can't be guaranteed. Therefore, it is important to analyze the impact that errors have on these parameters, namely on input pulse intensity, input pulse phase, and on cavity reflectance. Cavity phase is actively stabilized, and therefore does not have fixed errors associated with it.

In order to analyze the impact of errors on stacking performance, both on efficiency $\eta$ and on pre-pulse contrast $\chi$, random errors are applied to each parameter individually. Pulse errors have a normal distribution with zero mean and specified standard deviation for each of the parameters ($\sigma_\phi$ for pulse phases, and $\sigma_I$ for pulse intensities). Reflectance errors have a uniform,

zero mean distribution, such that $-\sigma_R < \Delta R < \sigma_R$, where $\Delta R$ is the applied reflectance error and $\sigma_R$ is the error bound. A uniform distribution of errors is used for reflectance since manufacturers have tolerance ranges specified, so parameter values are guaranteed within a certain window. All pulse phases, pulse intensities, or mirror reflectivities are perturbed using this distribution of errors, and the impact on stacking is analyzed. The experimental 4+4 case discussed in Section 2.6 is used, with 81-pulse equal-intensity stacking at maximum efficiency as well as the $\chi = 40\ dB$ pre-pulse contrast tradeoff point discussed in Section 2.7. The results of this are shown in Figure 2.20 and Figure 2.21 for the maximum efficiency and 40 dB pre-pulse contrast cases, respectively.

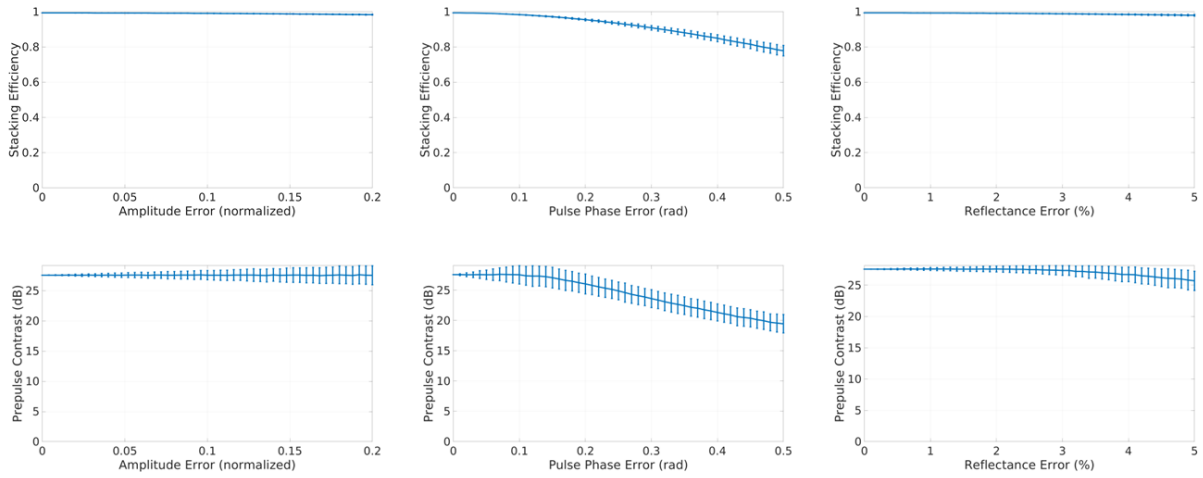


*Figure 2.20: Analysis of the impact of errors on stacking using 81-pulse equal-amplitude burst optimized for efficiency*

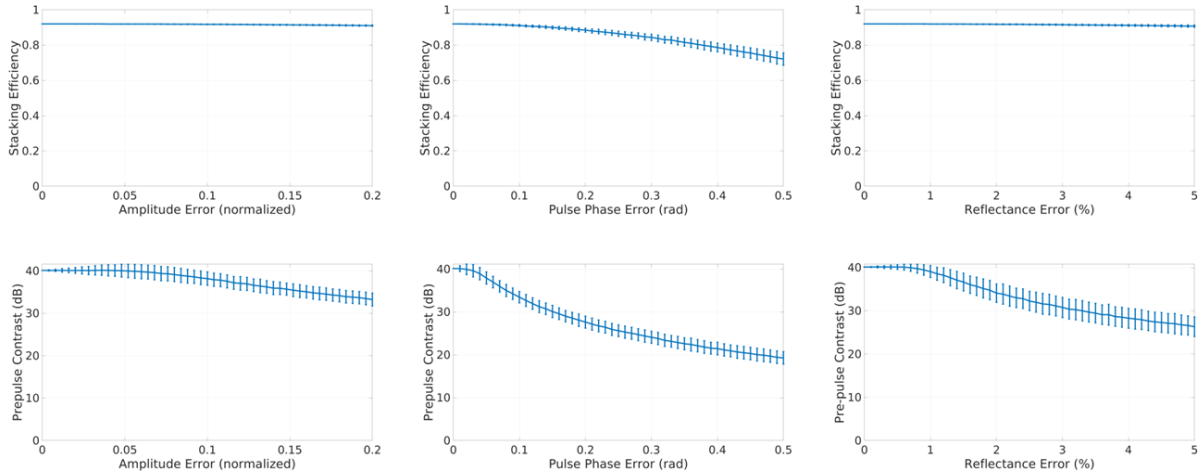


*Figure 2.21: Analysis of the impact of errors on stacking using 81-pulse equal-amplitude burst with 40 dB pre-pulse contrast*

Pulse intensity error has a negligible effect on stacking performance, even when an error of 20% of the pulse intensity is applied. Reflectance error is plotted out to 5% error, however tolerances can be guaranteed down to 1% accuracy. This means that reflectance error is also not that detrimental. The largest impact on stacking comes from pulse phase error, which is consequently also the most difficult to ensure is correct. In order to maintain good stacking quality even at high pre-pulse contrast operation, an accuracy of better than 0.05 radians needs to be achieved. However, directly measuring the pulse phase is not trivial to do. Therefore, other methods need to be used to ensure proper pulse phases are applied.

Optimization of pulse phases can be applied during stacking operation. While actively stabilizing cavity phases as discussed in Section 2.4, the pulse phases can be optimized to maximize stacking performance. By changing the pulse phase values on a much slower time-scale than the stabilization, the effect of these changes can be observed independently from the cavity phases. This enables correction of pulse phase errors in order to reach the required accuracies for high stacking performance. Once found, these values only need to be updated if system parameters change. Work on implementing these optimization routines is ongoing.

## 2.10 Conclusion

GTI cavities are shown to be physical implementations of a recurrent neural network, providing further insight into design and optimization strategies going forward. Additionally, further design of the stacking system is explored, investigating pre-pulse contrast improvement via post-pulse control, as well as stacking of equal-nonlinearity bursts. An analysis on the impact of errors on stacking performance was done, with methods suggested to meet the required parameter accuracies. This demonstrates the adaptable nature of the CPS technique, and provides the framework for implementation of high-performance stacking systems that are able to achieve high pre-pulse contrast with equal-nonlinearity burst shapes for laser-plasma applications.

# Chapter 3 Development of High-Precision Stacking Techniques for Robust High-Energy Operation

## 3.1 Introduction

The implementation of CPSA in a real laser system has a number of practical challenges associated with it. In Chapter 2, a number of assumptions were made about the stacking system. Specifically, it was assumed that the cavity round-trip length perfectly matched that of the pulse repetition rate, that that the cavity beam overlaps with the reference beam in both angle and transverse position, and that the pulse repetition rate is fixed. Each of these effects can have a detrimental effect on stacking performance, and it is important to investigate the impact of these errors as well as develop methods to ensure the required accuracies are met.

The errors in a GTI cavity can be isolated to three sources: beam overlap mismatch $\Delta x$, angular misalignment $\Delta\alpha$, and cavity round-trip length mismatch (piston error) $\Delta L$. Examples of each of these errors are shown in Figure 3.1. Each of these errors correspond to the error after one round-trip inside of a GTI-cavity. Multiple round-trips can compound the errors, increasing their impact on stacking. A rigorous method to quantify the impact on stacking each of these errors has, as well as techniques to ensure that the errors are minimized, are critical for implementing a stacking system.

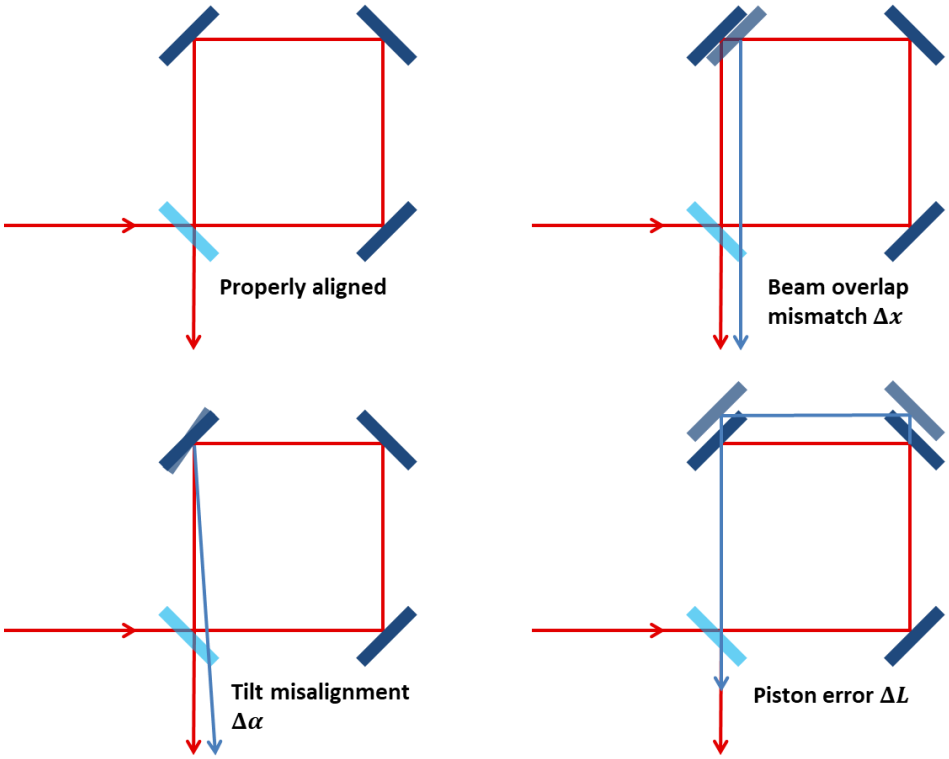


*Figure 3.1: GTI cavity misalignments shown, where the red path is properly aligned and the blue path shows deviation due to misalignment*

### 3.2 Quantification of Cavity Implementation Errors

Misalignment errors can be analyzed as a cumulative sum of all mirrors for a cavity, where the cavity as a whole has some errors per round-trip. This is because errors caused by one mirror can be corrected by other mirrors in the system, and therefore what we are primarily concerned with is the resulting error once the pulse leaves the cavity. Therefore, we can calculate errors relative to the reference path, which is the ideal path through the cavity, instead of looking at individual mirror errors. A simplified method of looking at errors induced by a mirror can be seen in Figure 3.2, where we can instead cast these errors relative to their impact relative to the reference path instead of on mirror misalignments.

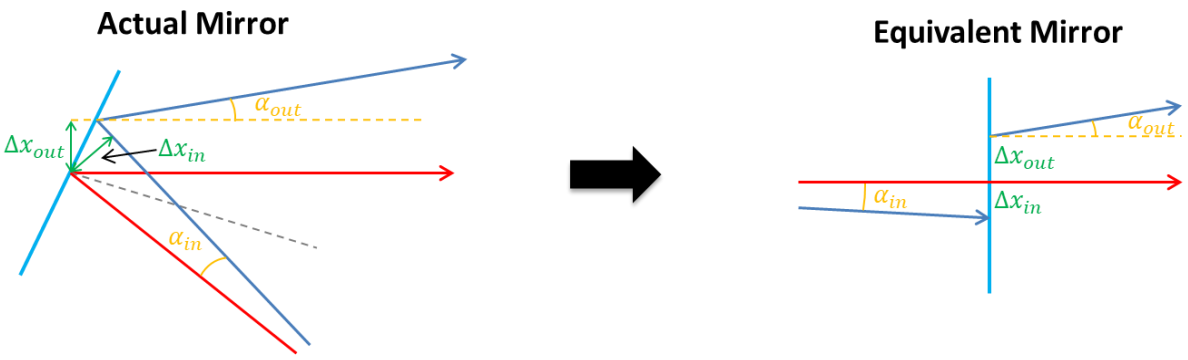


*Figure 3.2: A simplified diagram of errors caused by mirror errors*

Using this approach of casting them with an equivalent mirror, we can consider all the possible errors a mirror has, and quantify the impact relative to the reference path. A diagram of this can be seen in Figure 3.3, where reference path errors for beam overlap mismatch, tilt misalignment, and piston error are illustrated and quantified. Mirror errors can be described by two errors, a tilt error $\Delta\beta$ and a piston error $\Delta d$. Tilt is assumed to cause no displacement error, i.e. the mirror gimbals around the center, and piston error is assumed to be a longitudinal shift of the mirror that causes a path length change. Transverse shifting of a mirror will not cause misalignments, however it may cause clipping, so care should be taken to ensure that beams are in the center of mirrors. Additionally, as can be seen, propagating through free-space only impacts beam overlap errors, and this is only if a tilt error is already present.

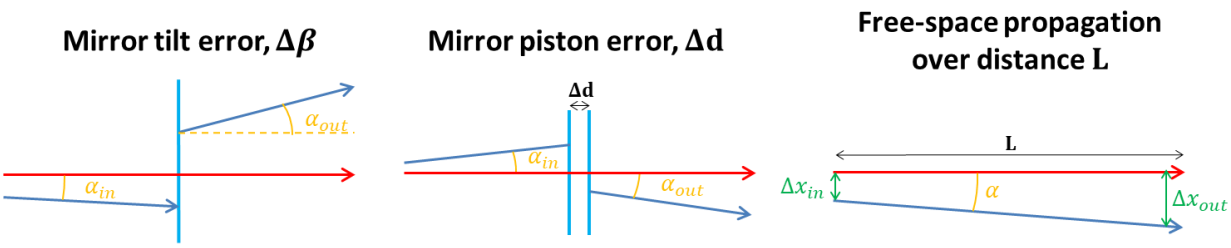


$$\alpha_{out} = -\alpha_{in} + 2\Delta\beta \quad \Delta x_{out} = -\Delta x_{in} \quad \Delta L = 0$$

$$\alpha_{out} = -\alpha_{in} \quad \Delta x_{out} = -\Delta x_{in} \quad \Delta L = 2\Delta d\cos(\alpha_{in})$$

$$\alpha_{out} = \alpha_{in} \quad \Delta x_{out} = \Delta x_{in} + L\sin(\alpha_{in}) \quad \Delta L = 0$$

*Figure 3.3: Errors caused by mirror tilt, mirror piston error, and free-space propagation are shown with equivalent mirror diagrams, and the impact on beam overlap mismatch, tilt misalignment, and piston error are quantified for each case*

Now that the impact of mirror errors on the reference path has been quantified, the effect on interference can be calculated. It is important to know the efficiency of interference $\eta$ in the presence of sub-optimal conditions. It has been established that Gaussian beam interference has efficiency degradations, which are shown in Equations 3.1-3.3 [14], and temporal pulse interference with a time-delay has an efficiency degradation $\eta_{piston}$ shown in Equation 3.4, assuming Gaussian temporal envelopes.

$$\eta_{tilt} \approx 1 - \frac{(kw_0\Delta\alpha)^2}{4} \tag{3.1}$$

$$\eta_{overlap} \approx 1 - \frac{\left(\frac{\Delta x}{w_0}\right)^2}{4} \tag{3.2}$$

$$\eta_{diffraction} \approx 1 - \frac{\left(\frac{z_1 - z_2}{\sqrt{2}z_R}\right)^2}{4} \tag{3.3}$$

$$\eta_{piston} \approx e^{-\frac{(\tau_1 - \tau_2)^2}{8\tau_{coh}^2}} \tag{3.4}$$

Here, $w_0$ is defined as the 1/e$^2$ beam radius, $k$ is the wave vector defined as $k = \frac{2\pi}{\lambda}$, and $z_R$ is the Rayleigh length of the beam defined as $z_R = \frac{1}{2}kw_0^2$. $z_1$ and $z_2$ correspond to the distance travelled from the beam waist location by each of the two interfering beams. $\tau_{coh}$ is the coherence length of the transform-limited pulse, determined by the pulse bandwidth, and $\tau_1$ and

$\tau_2$ correspond to the timing error of the two interfering pulses, defined by $\tau_i = \frac{\Delta L_i}{c}$, where $c$ is the speed of light in free-space.

These provide the framework for calculating stacking efficiency in the presence of errors, as they enable quantification of the impact of errors when two pulses with their own sets of errors interfere at the exit to the stacker system. Using this approach, we can calculate all of the sub-pulses that will exit a stacking system. Taking for example a 4-cavity stacker and calculating the impulse response, the first output pulse would be the reflection from each of the partial reflectors. The second output pulse would consist of four sub-pulses, consisting of one round-trip in each cavity. The third output pulse would be made up of 16 sub-pulses, consisting of two round-trips in the first cavity, one in the first and one in the second, so on and so forth. This can quickly be identified as a permutation problem, where all possible combinations of round-trips inside each cavity must be considered, and each sub-pulse must then interfere with every other sub-pulse in the same time slot, resulting in the output pulse for that specific time slot.

### 3.3 Impact of Cavity Implementation Errors on Stacking Performance

Analyzing the 4+4 cavity configuration discussed in Section 2.6, we can look into specific system parameters and how they impact stacker tolerances. First, we determine a beam size for our stacker system. This involves calculation of the effect of diffraction on stacking performance, which has been analyzed before and is shown in Figure 3.4 [14]. Knowing that for our longest cavity set, the cavity length $L = 2.7m$, and assuming the Rayleigh length must be 20 times longer than this length, we get a resulting beam radius of $w_0 \approx 3mm$.

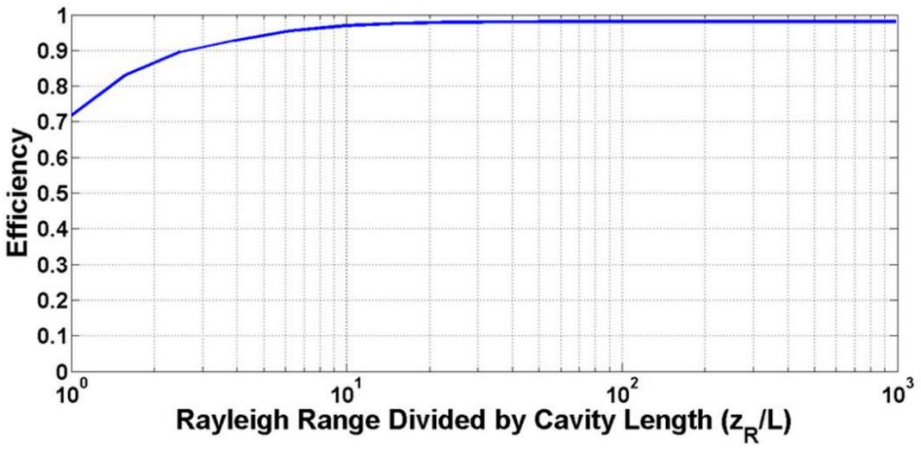


*Figure 3.4: Effect of diffraction on stacking efficiency for 4 GTI-cavities stacking 9 input pulses [14]*

Using a laser-induced damage threshold (LIDT) of $LIDT = 10\,\frac{J}{cm^2}$ and a beam radius of $w_0 = 3mm$, assuming a Gaussian beam, an optical damage threshold of $LIDT * \frac{beam\ area}{2} = \frac{10J}{cm^2}\frac{\pi(0.3cm)^2}{2} = 1.41\,J$ is calculated, which for our current experiments is acceptable and allows us to operate with 1" mirror diameters, however will have to be addressed in future systems.

Additionally, as can be seen in Equations 3.1 & 3.2, the efficiency loss due to tilt error is directly proportional to the beam size, and efficiency loss due to overlap error is inversely proportional. For example, using a beam radius $w_0 = 3mm$, the stacking efficiency is much more sensitive to tilt errors than to beam overlap errors. For these simulations, the central wavelength of the spectrum is taken as $\lambda_0 = 1.03\mu m$, and a bandwidth of $\Delta\lambda = 30nm$ is used, which corresponds to a coherence time $\tau_{coh} = 100fs$. With these system parameters in place, we can now analyze the effect of cavity errors on stacking efficiency.

When calculating the interference of all the sub-pulses for a given time slot, a straightforward computation runs into a limit. For the experimental 4+4 cavity configuration, an 81-pulse train input with eight cavities would result in over $1.7 * 10^{72}$ sub-pulses. This, of course, is not feasible to implement, as the simulation would never finish. Instead, we can

truncate the number of round-trips considered inside of a cavity, such that after a certain number of round-trips the pulse is considered to be low-enough intensity that it does not impact stacking. A plot showing this can be seen in Figure 3.5 [39], where the number of cumulative round-trips is changed and the stacking efficiency and simulation time are measured for each case. A truncation length of 15 is chosen such that impact on stacking performance is minimal and simulations can be done in a timely manner.

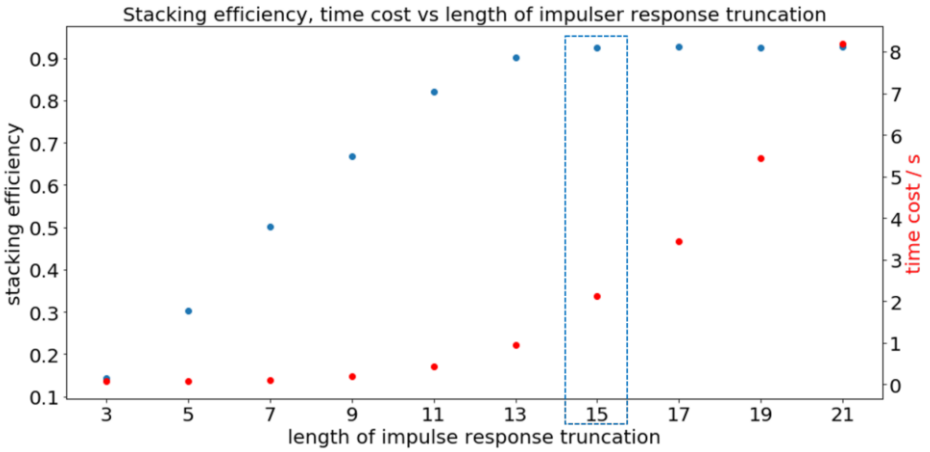


*Figure 3.5: Impulse response truncation length impact on stacking efficiency (blue) and simulation time (red) [39]*

The geometry of the cavities needs to be considered as well, as if there are an even or odd number of reflections in the cavity, the alignment tolerances will change for the in-plane axis. However, the out-of-plane axis will behave like the even number of reflections case. Since the even case is the more sensitive of the two, alignment accuracy must be sufficiently high such that the out-of-plane axis is properly aligned, and therefore only the more stringent even number of reflections is considered.

Now that all of the simulation considerations have been taken care of, errors can be applied to cavities and the impact of stacking performance can be analyzed. Mirror tilt and piston errors are applied in a zero-mean normal distribution with standard deviation values $\sigma_{tilt}$ and $\sigma_{piston}$ for the tilt and piston errors, respectively. These errors are applied over many trials, and

the stacking efficiency for each case is calculated. The effects of these errors can be seen in Figure 3.6, with the stacking efficiency averaged over 40 trials for each distribution of errors.

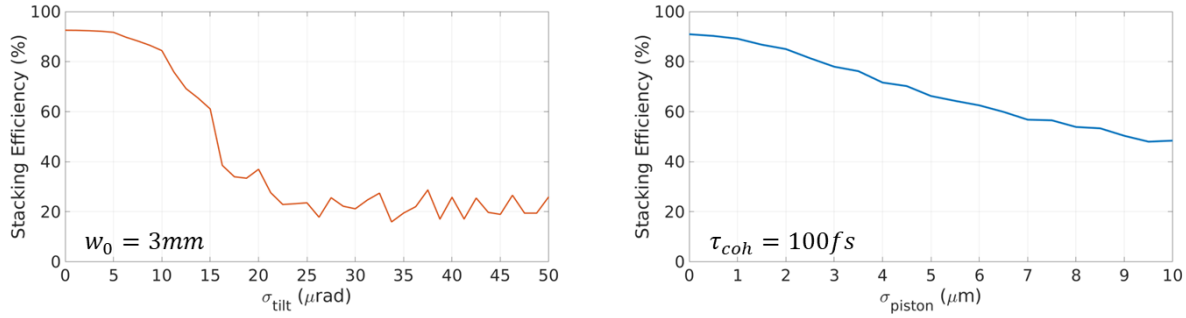


*Figure 3.6: Stacking efficiency for different error distributions of tilt error (left) and piston error (right)*

This informs us what stacking performance we can expect to achieve, on average, given these errors. However, we are also interested in the repeatability of the stacking, and therefore can analyze the distribution of efficiencies for each error magnitude. The stacking efficiencies with error bars corresponding to standard deviation of efficiencies can be seen in Figure 3.7, and with error bars corresponding to the maximum and minimum efficiency observed in Figure 3.8.

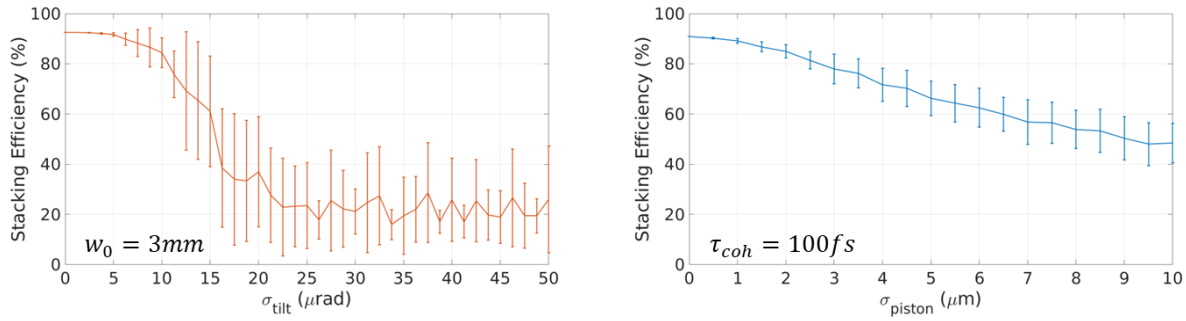


*Figure 3.7: Stacking efficiency with error bars corresponding to standard distribution of efficiencies for different error distributions of tilt error (left) and piston error (right)*

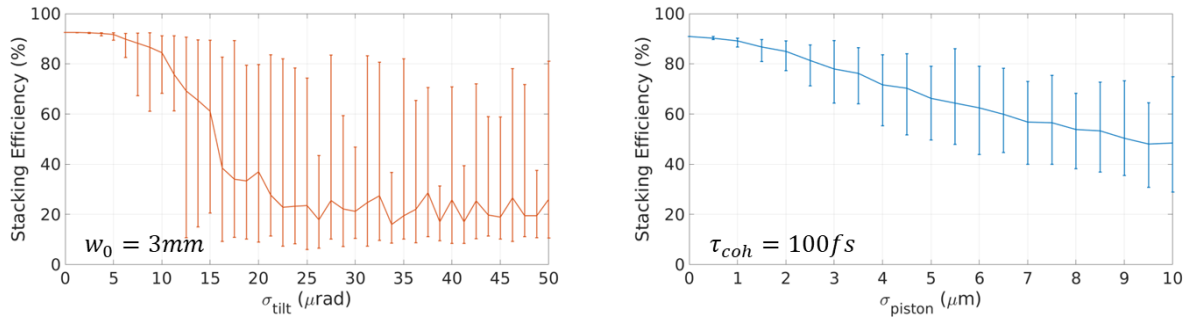


*Figure 3.8: Stacking efficiency with error bars corresponding to maximum and minimum efficiency observed for different error distributions of tilt error (left) and piston error (right)*

By looking not just at the average, but at the distribution of efficiencies, we gain insight into both the required alignment accuracies and the methods used. For example, even with rather large tilt errors, good stacking efficiency can be achieved if the right conditions are met, but on average the result is poor. This means for repeatability, the accuracy requirement is ~5 µrad. This also shows that alignment must be done for each cavity individually, as there appears to be a coupling between cavity tilt errors that can be perceived as the correct alignment. For piston error, an accuracy of ~1 µm is required, which is less than one wavelength, meaning the only misalignment is the phase of the cavity itself.

### 3.4 Cavity Tilt Alignment Techniques

In order to meet the tilt requirement outlined in Section 3.3, an alignment metric is required that can achieve <5 µrad for each cavity consistently. The rough alignment procedure involves using a CMOS camera to look at beam overlap in the near-field and far-field. Amplified stimulated emission (ASE) must be used for this process, as if there is any loss in the cavity such as clipping on optics, spatial fringes will distort the beam center and therefore the alignment accuracy. However, ASE is not coherent with itself when delayed like mode-locked pulses are, therefore it can be used to overlap the beams without interference effects.

First, the cavity is blocked, and the camera is placed far away from the exit of the cavity, which will be referred to as the far-field. The beam-tracking software on the camera zeros the beam position, then the cavity is opened and multiple round-trips will be seen on the camera. The average of these round-trips is shown, and in this way all of the round-trips can be made to overlap in the far-field. This process is then repeated in the near-field, and iterated back and forth until the overlap is sufficiently good. Obviously, this is not an accurate alignment method. The alignment accuracy is not easily quantifiable, it uses qualitative judgment for when alignment is good enough, and is an overall slow process. While this can, and should, still be used for rough alignment, a more accurate method is desired for high accuracy and precision such that optimal stacking can be achieved consistently.

Methods have been proposed for automated alignment of spatial combining channels using spatial interference fringes [43], however temporal combining cannot directly use these techniques. They leverage the existence of spatial fringes across the beam from wavefront tilt caused by angular misalignment to co-align the channel. However, a cavity that does not have losses (i.e. is not clipping on optics) can't use this, as when the burst is integrated it does not have spatial fringes present. Instead, it simply changes how energy is distributed in time. Therefore, instead of using an average power detector to align the beams, single-cavity stacking is employed, and fast detection of the pulse train is used to analyze the stacked pulse. Stacking of a single cavity is shown in Figure 3.9, using a cavity reflectance value $R = 0.57$, as this is the value in the final experimental 4+4 stacker system. Since the reflectance is chosen for 81-pulse stacking and not single-cavity, an odd input shape must be used corresponding to the impulse response of a single cavity, however it is suitable for alignment purposes.

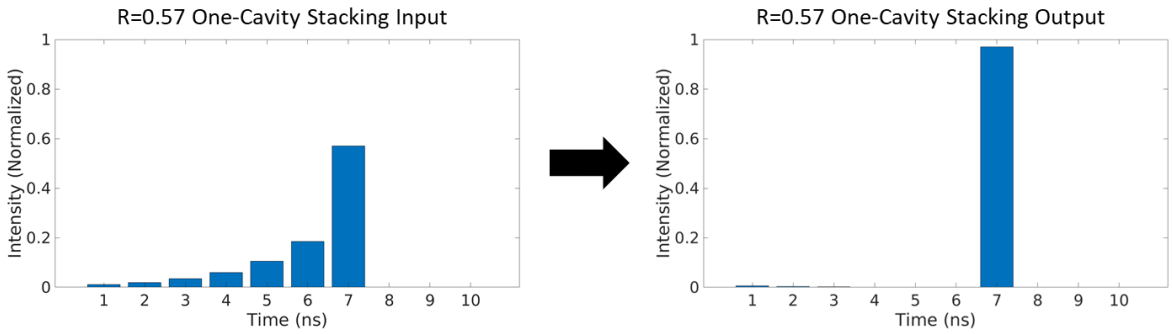


*Figure 3.9: Single-GTI stacking using a reflectance $R = 0.57$ and phase $\delta = 0$ with input (left) and output (right) shown*

Now, we need to know how tilt misalignment affects single-cavity stacking. Defining a sub-pulse as $E^m(x) = E_0^m(x) * e^{i(kxsin\theta_m)+\phi_m}$, where $E_0^m(x)$ is the field amplitude as a function of beam position, $k$ is the wave vector, $x$ is the horizontal position of the beam, $\theta_m$ is the angle relative to the reference path, and $\phi_m$ is the accumulated phase. For this analysis, it is assumed a Gaussian beam of beam radius $w_0 = 3mm$ is used. Using this, the sum of $N$ sub-pulses with angular tilt can be calculated using

$$I(x) = \sum_{m=1}^{N}\sum_{n=1}^{N} E^m(x)E^{n*}(x) = \sum_{m=1}^{N}\sum_{n=1}^{N} E_0^m(x)E_0^n(\mathrm{x})\cos\left(kx(\sin\theta_m - \sin\theta_\mathrm{n}) + \phi_m - \phi_n\right)$$

where m and n are iterator variables. Using this equation, we can take the same sub-pulse approach used in calculating cavity errors, and calculate the intensity for each output pulse as a function of beam position. This can be seen in Figure 3.10, where the stacked pulse intensity and the sum of reject pulse intensities are plotted for different cavity misalignments. Reject pulses are defined as any pulse in the output train that is not the stacked pulse. From this, we can see that indeed, the average power of the burst does not change with angular misalignment. However, the stacked pulse intensity does, so we can use this to properly align our cavities.

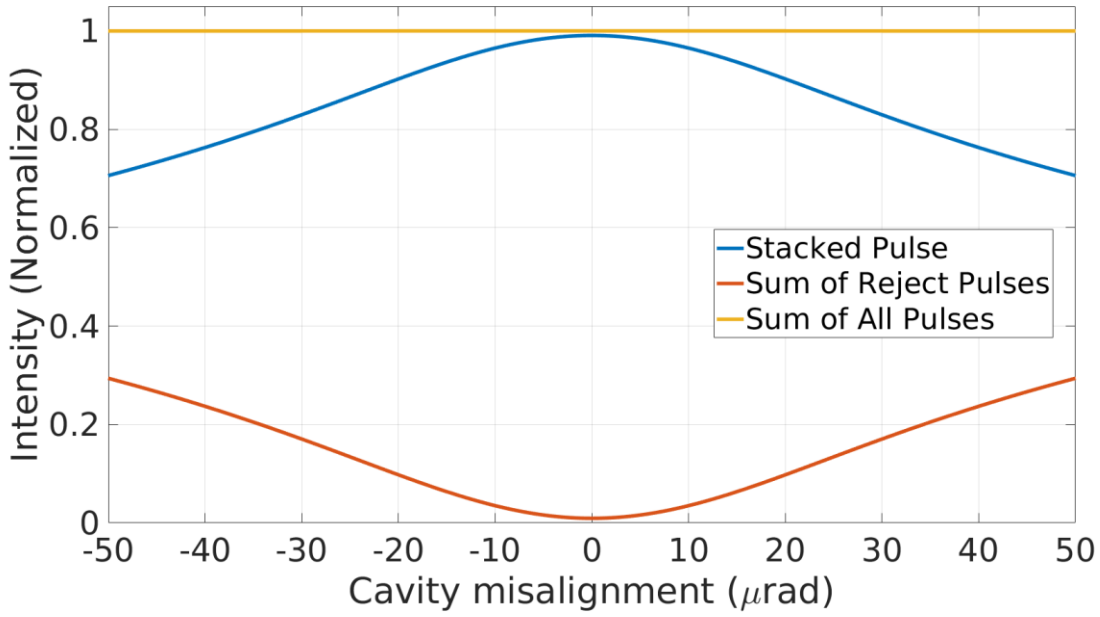


*Figure 3.10: Intensity of stacked pulse and reject pulses as a function of cavity tilt error, assumes proper cavity phase is applied*

Using this information, we can design an alignment technique that will both meet the required accuracy and be an automated process, speeding up alignment and increasing both accuracy and precision. First, a single cavity is stacked using the waveform shown in Figure 3.9, and this stacking is maintained at a fast loop speed (>100 Hz). Then, at a slower loop speed (~5 Hz), the tilt of both the x-axis and y-axis of the cavity are optimized using the stochastic parallel gradient descent (SPGD) algorithm. The 2-D landscape is shown in Figure 3.11, where it can be seen that the optimal tilt position is both the global maximum and the only local maximum. Therefore, SPGD will converge to the correct cavity alignment.

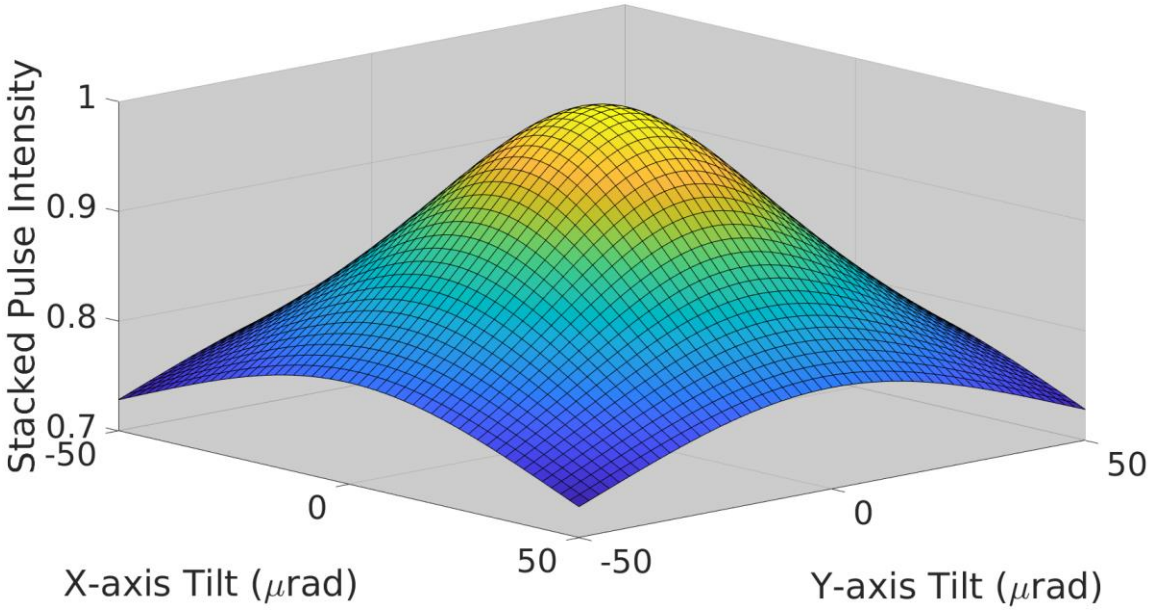


*Figure 3.11: Surface plot of the singe-cavity stacked pulse intensity for cavity misalignment in the x and y axes*

The convexity of this landscape can be investigated, to determine the alignment accuracy achievable. Assuming an RMS amplitude noise of 1% from the laser system, which corresponds to noise levels measured in our experimental system, an accuracy of $\pm 6\,\mu rad$ can be achieved, which is close to the requirements described in the previous section.

### 3.5 Cavity Timing Alignment Techniques

In addition to tilt alignment, cavity round-trip timing accuracy also needs to be quantified, and techniques developed to ensure it meets the required tolerances. Round-trip error comes from the fact that a fixed delay results in a spectral-dependent phase. If we assume the cavity has a round-trip error $d$, then for a pulse with electric field $E^m(\lambda) = E_0^m(\lambda) * e^{i\left(\frac{2\pi}{\lambda}d\right)+\phi_m}$ we find the phase of the pulse is wavelength-dependent. We also define the spectral intensity $E_0(\lambda)$ to be a super Gaussian of the second order, as this roughly approximates what we experimentally use. This means that all wavelengths cannot be simultaneously phase-matched to

the proper stacking position, causing what we describe as “spectral fringes”. While these are not true fringes in the sense of plane-wave interference, they do follow the same logic, as a phase shift across the spectrum causes constructive and destructive interference at intervals. Therefore, we can apply similar techniques to align the timing of the cavities, and even use this to automate the alignment similar to what is described in the previous section.

Rough alignment of the cavity timing is achieved by scanning the cavity length in one direction and watching the spectral beating pattern. Similar to the tilt alignment case, spectral beating will only be observed if there is some mechanism of loss in the cavity, otherwise the integrated burst spectrum will not change. Since spectrometers are generally much slower than the pulse burst duration, they can’t be used for cavity piston alignment. Instead, using a fast photodiode before the compressor that has rise and fall times much faster than the pulse duration, the spectrum can be viewed on a fast oscilloscope. This is due to the temporal chirp providing a one-to-one mapping of the spectrum to the temporal pulse profile. This allows us to look at spectral beating effects, and determine the timing mismatch. Seen in Figure 3.12, spectral beating of two pulses is shown for changing path-length differences.

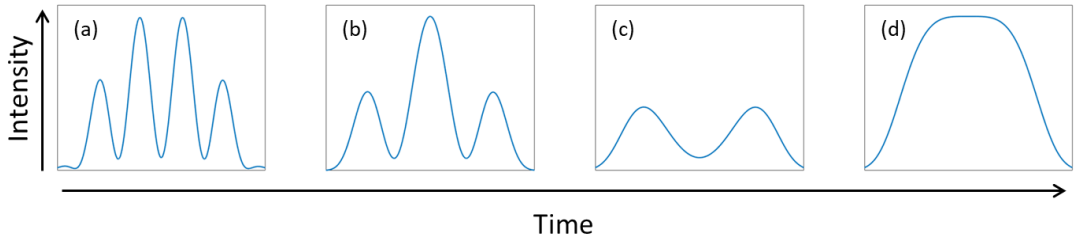


*Figure 3.12: Simulation of spectral beating of two pulses interfering with path length difference of (a) 500µm, (b) 300 µm, (c) 100 µm, (d) 0 µm*

By eliminating the spectral beating, the cavity length can be properly aligned. The spectral beating is obvious when far away from the proper timing location, however it can be difficult to tell what the optimal cavity length is when it is close. Seen in Figure 3.13, the spectral beating

pattern must be observed while scanning the cavity length in a linear fashion and seeing of the pattern moves from left to right, or right to left. This is time consuming, and is once again up to the judgment of the person aligning. Instead, we would like a method that is repeatable, fast, and accurate.

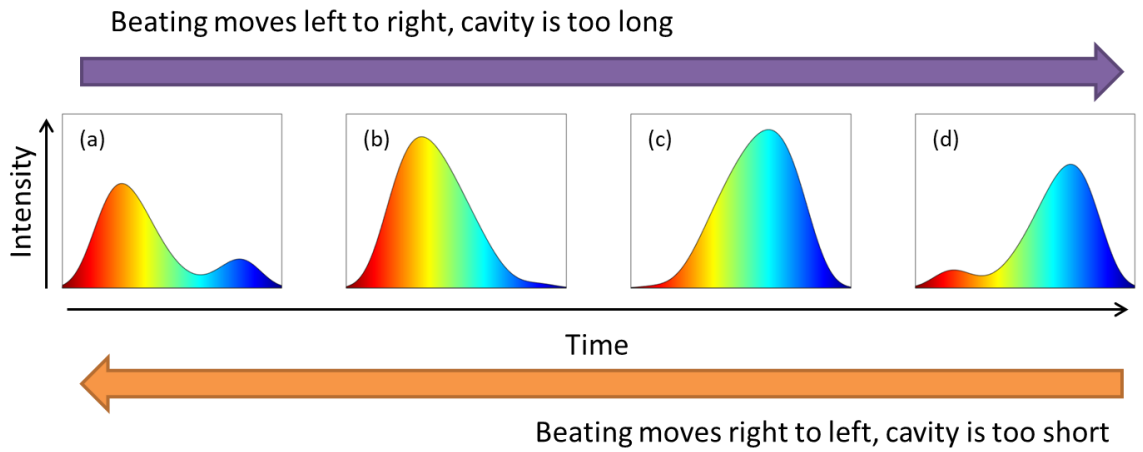


*Figure 3.13: Simulation of spectral beating pattern as cavity length is scanned, direction of beating indicates if cavity-oscillator mismatch is positive or negative*

Similar to the tilt alignment case, methods for automating round-trip alignment have been developed for spatial coherent combining techniques [44], however they can't be used because again the time-integrated burst has no spectral beating. So we can once again employ the same techniques used, where single-cavity stacking is leveraged in order to align the timing of the cavities. We define for the spectral case the sum of N sub-pulses as

$$I(\lambda) = \sum_{m=1}^{N}\sum_{n=1}^{N} E^{m}(\lambda)E^{n^*}(\lambda) = \sum_{m=1}^{N}\sum_{n=1}^{N} E_0^{m}(\lambda)E_0^{n}(\lambda)\cos\left(\frac{2\pi}{\lambda}(d_m - d_n) + \phi_m - \phi_n\right)$$

which allows us to determine the intensity of every pulse for different cavity round-trip errors. A plot of this can be seen in Figure 3.14, showing the stacked pulse intensity, the resulting sum of reject pulse intensities, and the sum of all pulses over different cavity piston errors. Cavity phase is assumed to be the correct stacking value as piston values are changed.

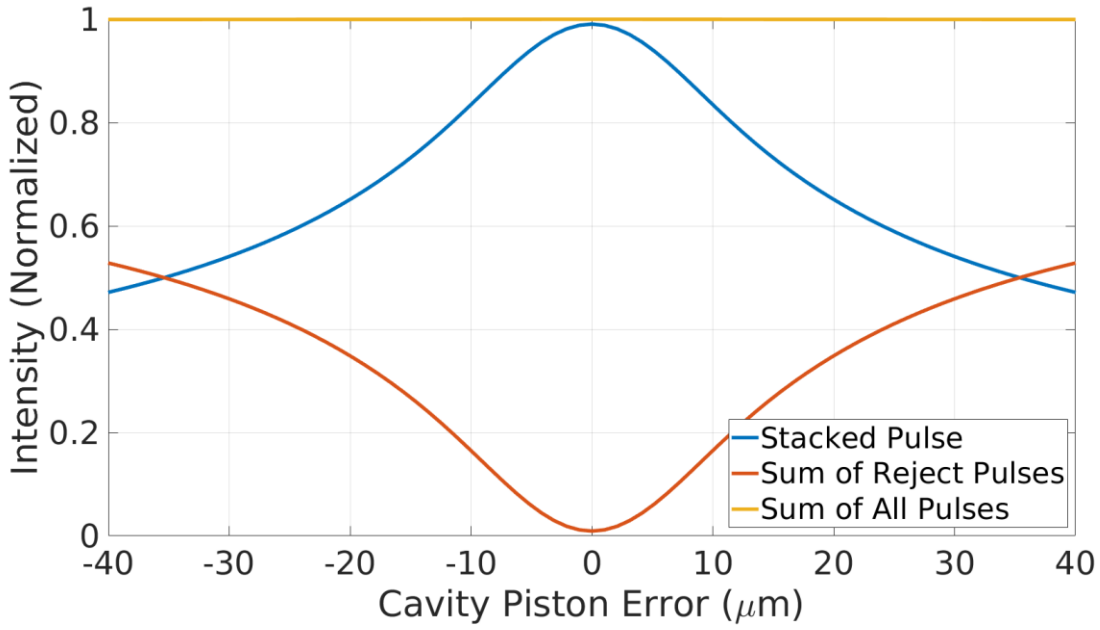


*Figure 3.14: Intensity of stacked pulse and reject pulses as a function of cavity piston error, assumes proper cavity phase is applied*

Unlike the previous tilt case, the cavity round-trip time and phase are linked together, meaning one cannot actively maintain single-cavity stacking while slowly adjusting the round-trip length. Instead, $2\pi$ "jumps" are taken, where the cavity is moved by one full wave, the phase is re-stabilized, and the stacked pulse value is taken once again. Large jumps like this are important, as if less than a $\pi$ step is taken, the phase stabilization will bring the stacking back to the original stacking position. Therefore, if we instead stride through the landscape with these so-called $2\pi$ jumps, once again assuming an RMS amplitude noise level of 1%, a round-trip accuracy of <2 μm can be achieved, which places us in the range that phase stabilization takes over. Therefore, using this method we can both automate the piston alignment process, making it much faster, as well as increase its accuracy and precision, ensuring good quality consistent stacking.

### 3.6 Mode-Locked Laser Timing Stabilization

Section 3.5 details how the cavities can have their round-trip time accurately aligned such that it matches the repetition rate of the oscillator, however we also need to ensure that the pulse repetition rate is also stable. If timing jitter is present, this will introduce both piston and phase errors on the stacking performance.

Timing jitter is a very important parameter for stacking performance, as the cavity must exactly match the repetition rate of the mode-locked laser source. However, it is especially important for multiplexed cavities, which have a round-trip length $\tau_{rt} = m * \frac{1}{f_{rep}}$, meaning that a cavity that is m-times longer than the repetition rate will consequently be affected by timing jitter m-times more. In order to overcome this, the oscillator cavity is actively stabilized to a highly stable RF source. A diagram showing the stabilization scheme of the mode-locked laser is shown in Figure 3.15.

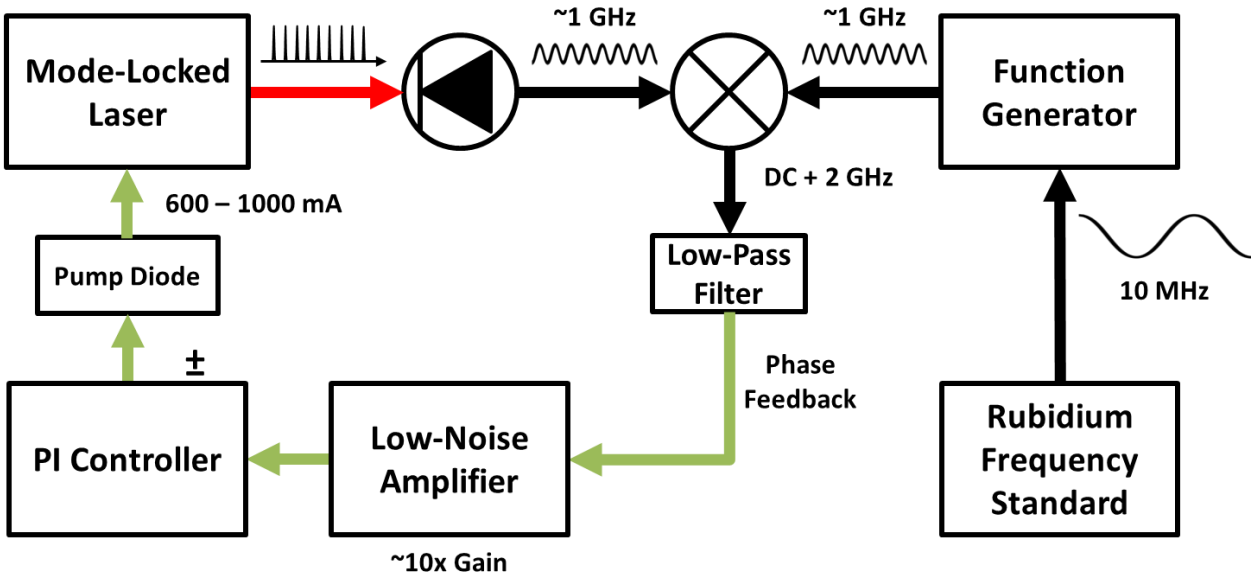


*Figure 3.15: Stabilization of mode-locked oscillator is achieved by matching repetition rate to RF source via modulating a pump diode current to change the timing in the cavity*

The mode-locked laser produces a pulse train at a repetition rate $f_{rep}$, which for our oscillator, is ~1 GHz. This pulse train is incident upon a photodiode, producing a sine wave at the repetition rate. This is then mixed with a sine wave generated from an RF function generator, which is very close to $f_{rep}$. The RF function generator is referenced to a rubidium frequency standard in order to maintain stability over long periods of time. These two mixed RF signals then produce an output $\left(f_{rep} + f_{RF}\right) + (f_{rep} - f_{RF})$, which is then low-pass filtered to give only the beat signal of the two frequencies. This is used as a phase feedback to make a phase locked loop (PLL), which can be stabilized to fix the frequency of the laser. A low-noise amplifier is used to increase the voltage of the signal, and it is fed into a PI controller. The frequency roll-off of the controller is set to 100 kHz, as this is the maximum frequency modulation of the pump current allowed by the controller. The output voltage is limited to ±1 V, again determined by the pump diode controller, to modulate the pump diode anywhere between 600 mA and 1000 mA. By modulating the current of the pump diode, the repetition rate of the oscillator can be controlled on a fast timescale, enabling a drastic decrease in noise.

In order to test the effectiveness of the feedback method, a long cavity (round-trip time $\tau_{rt} = 9 * \frac{1}{f_{rep}}$) is stacked using a single-cavity stacking profile. Then, as stacking is maintained, the phase of the cavity is tracked to see how much it needs to move to maintain stacking. This is performed both with stabilization turned off and turned on, and is shown in Figure 3.16. As can be seen, this provides a drastic decrease to the phase drift of the oscillator, and the cavity barely needs to move in order to maintain stacking. This allows us to achieve better stacking stability and maintain timing alignment throughout the day and even day-to-day.

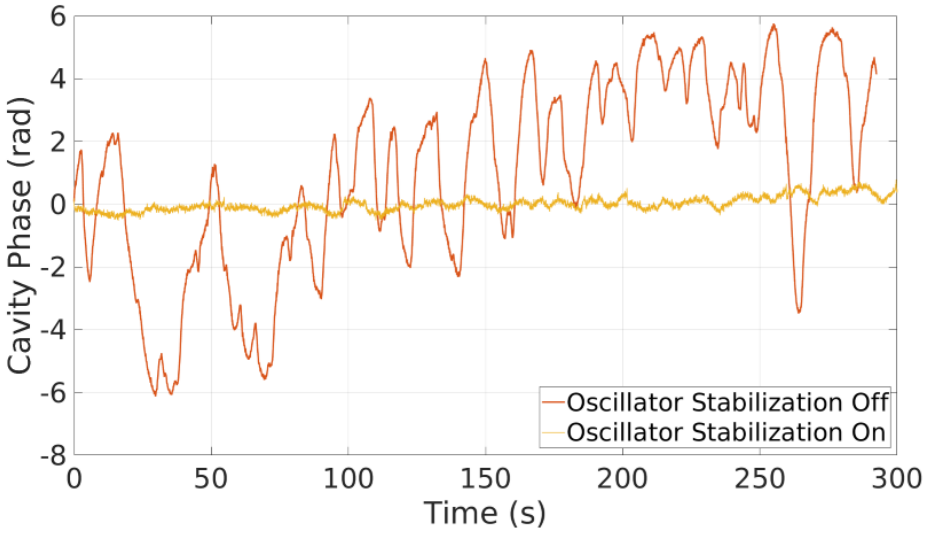


*Figure 3.16: Phase tracking of long cavity with oscillator stabilization enabled and disabled*

### 3.7 High-Efficiency Repeatable Stacking

With the new automated alignment procedures discussed in Sections 3.4 & 3.5, high accuracy stacking alignment can be achieved on a repeatable basis. One such stacking trace is shown in Figure 3.17.

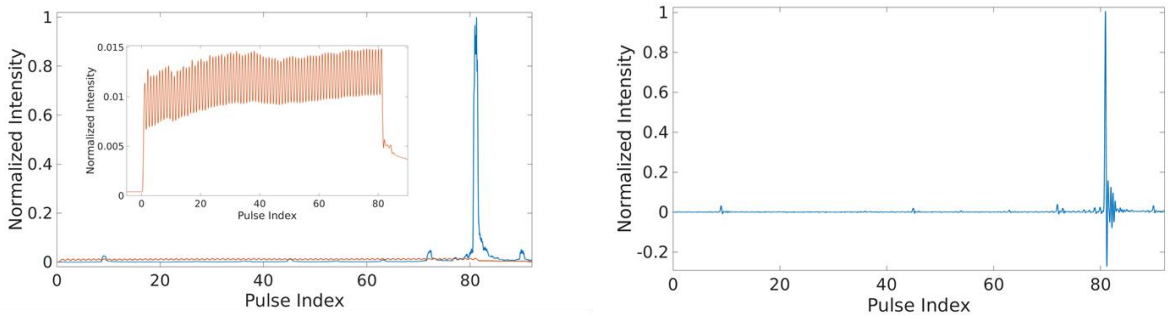


*Figure 3.17: Low-power stacking measured with high efficiency (left) stacking trace measured with fast photodiode before compressor, with inset of input burst shape in orange also plotted on the same scale as stacked burst, (right) stacking trace measured with 2.5 GHz photodiode after compressor*

The output stacked burst is measured both before and after compression, both to validate the measurement and because each measurement gives us insight into the stacking performance. Before compression, a very fast (>12.5 GHz) photodiode is used to map the spectrum of each pulse to the time domain, shown in Figure 3.17. After compression, a slower (2.5 GHz)

photodiode is used, and since the compressed pulses are much shorter than the response time of the detector, each pulse generates an impulse response of the detector as seen in Figure 3.17, which is why ringing and negative voltages are observed. Due to the high contrast ratio between the stacked pulse and the rejected pre-pulses, many of the non-stacked pulses are below the noise floor of our detection scheme. This poses a challenge in accurately measuring the stacking performance, so a low-pass Butterworth filter is applied to the measured trace in order to reduce white noise but keep the 1 GHz frequency components.

Stacking efficiency is measured using the compressed photodiode trace because the stretched photodiode can have spectral beating, resulting in shaped pulses, making calculation difficult. With the compressed photodiode, each pulse generates the impulse response of the detector, so only the peaks of the pulses need to be considered. Stacking efficiency is calculated by taking the ratio of the stacked pulse to the sum of the pre-pulse train, specifically according to $\eta = \frac{I_{stacked}}{\sum_1^N I_{out_n}}$ where N is the number of input pulses. Using this method, we calculate a stacking efficiency of 83%, and in the absence of errors we simulate a stacking efficiency of 98%. Stacking of this efficiency is repeatable day-to-day, and can be quickly recovered using the automated alignment methods mentioned before.

The pulse duration is measured during stacking as well, and can be seen in Figure 3.18. It is important to note that while stacking is running, the pulse duration does not get longer, and therefore it can be seen that stacking does not affect the compressed pulse. This is critical for applications, in which distortions to the compressed pulse shape would be detrimental to performance.

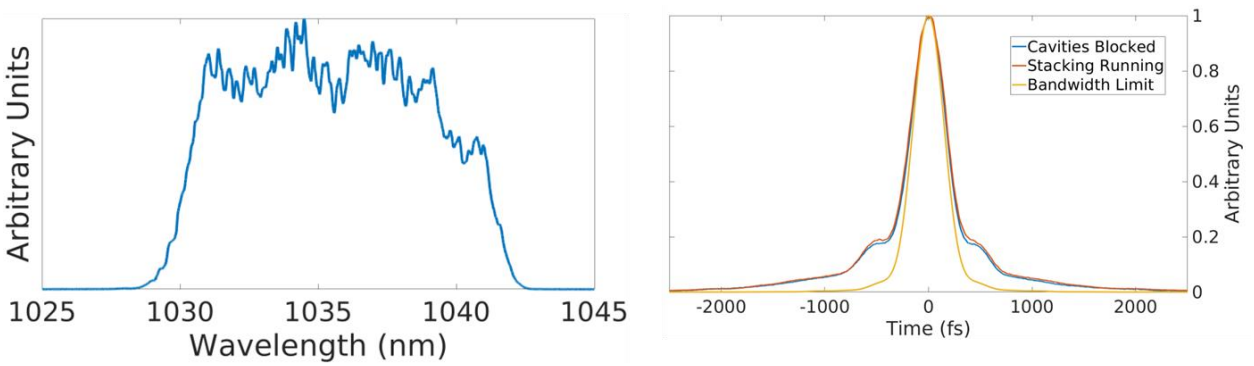


*Figure 3.18: (left) Measured spectrum of low-power stacking output, (right) autocorrelation at low-power both with stacking running and with all cavities blocked, also plotted is the autocorrelation of the calculated transform-limited pulse*

### 3.8 Robust Stacking Performance

By locking of the mode-locked seed laser using the techniques described in Section 3.6, highly stable stacking operation is achieved. On a particularly bad day, oscillator stabilization was intentionally disabled and stacking was performed with and without its assistance. The stacked pulse stability can be seen in Figure 3.19.

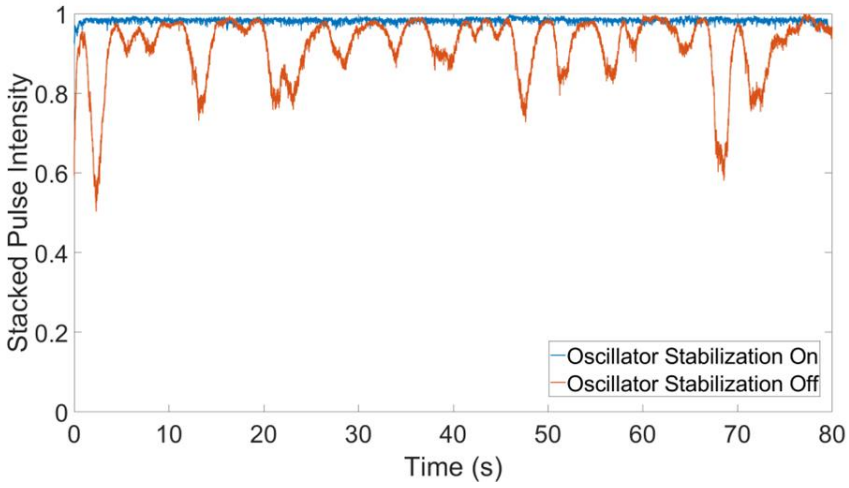


*Figure 3.19: Stacked pulse intensity measured during active stacking operation with the oscillator stabilization enabled (blue) and disabled (orange)*

Without locking of the seed source, the drift can cause quite high instability, and the magnitude of this drift changes from day-to-day, meaning stacking performance would literally be dependent upon the weather. Instead, with oscillator stabilization, a measured RMS of less than

1% can be seen in Figure 3.20. A cutout of 6 minutes is shown here, however active stacking was shown to be maintained for over an hour before the experiment was turned off, demonstrating this can be used over long periods of times for experimental applications.

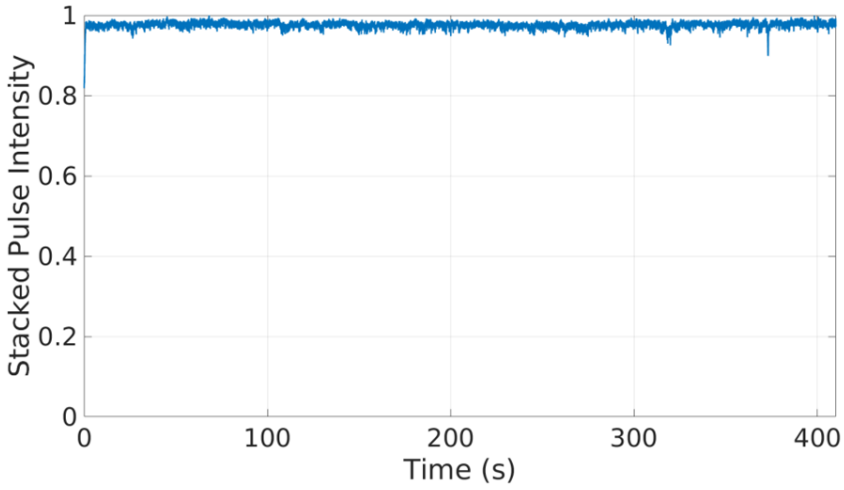


*Figure 3.20: Stacked pulse stability with RMS <1% over 6 minutes*

## 3.9 Conclusion

The tools developed in this chapter enable the performance of high efficiency and robustly stable stacking over long durations of time in a manner that is repeatable for day-to-day operation. Quantification of the required angular and piston alignment tolerances were determined, and techniques to meet these required accuracies were developed and implemented. Additionally, the developed techniques also enable faster and more consistent alignment. Stabilization of the mode-locked oscillator was shown to be crucial to stacking performance, and was implemented, resulting in robust and stable stacking operation.

# Chapter 4 System-Level Demonstration of Simultaneous Coherent Beam Combining & Coherent Pulse Stacking Amplification

## 4.1 Introduction

Coherent beam combining (CBC) of fiber lasers allows scaling of average power and energy beyond what a single fiber amplifier can provide. This allows fiber lasers to be used in light-matter interactions requiring high peak powers (>10 TW) while still providing high wall-plug efficiency (>50%) and enabling high repetition rates (1-50 kHz). However, when operating at high peak power, only a fraction of the total stored energy can be extracted from the fiber amplifier, as seen in Figure 1.2 and discussed in Section 1.2.

Coherent pulse stacking amplification (CPSA) effectively stretches the chirped pulse to longer durations, enabling complete energy extraction from the final fiber amplifiers and, consequently, reducing the required number of fiber channels. In this chapter, we demonstrate for the first time system-level operation of simultaneous CBC & CPSA with pulse energies per channel close to the stored energy limit, laying the groundwork to further scaling of number of spatial channels, combined pulse energies and power, and stacked pulse durations. The work presented in this chapter is done jointly with Alexander Rainville, who primarily focused on the coherent beam combining, pulse burst nonlinear phase calculations, and high-energy compression, while my focus was on CPSA, stabilization, and system controls.

## 4.2 Coherent Beam Combining & CPSA Demonstration System

The experimental layout of simultaneous coherent beam combining (CBC) & coherent pulse stacking amplification (CPSA) is shown in Figure 4.1. Similar to the low-power system demonstration, first a 1 GHz mode-locked fiber oscillator produces a train of output pulses, each one ~80 fs in duration. A pair of amplitude and phase electro-optic modulators create the stacking burst of 81 pulses at a burst repetition rate $f_{burst} = 1\ MHz$, pre-shaping the burst to compensate for gain saturation effects. This burst is then stretched to a stretched pulse duration of ~1 ns, making the burst effectively 81 ns long. The burst is then amplified and down-counted through a series of amplifiers and acousto-optic modulators (AOMs). As the peak power of the burst increases, the mode-field diameter of the fiber amplifiers is also increased to avoid nonlinear effects. Finally, the burst exits the last pre-amplifier at its final repetition rate of 1-10 kHz, and is split into parallel fiber amplifiers in the spatial combining setup. This is then recombined, stacked, and compressed into a single output pulse.

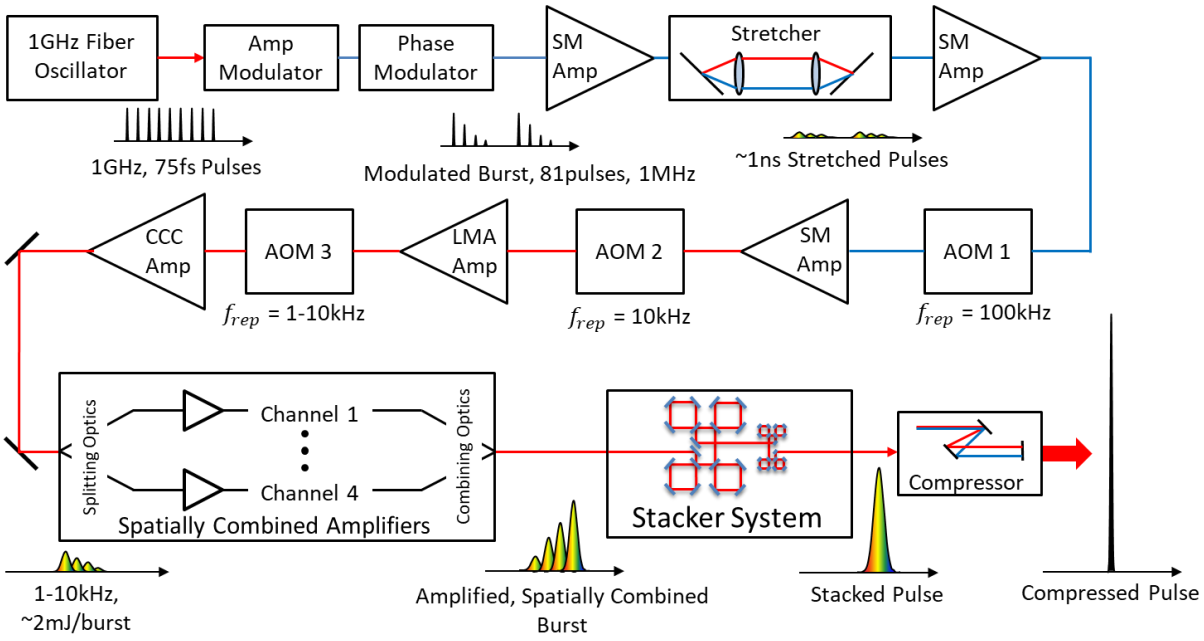


*Figure 4.1: Experimental setup for simultaneous coherent beam combining and coherent pulse stacking amplification*

### 4.3 High Energy CPSA System Diagram

The stacking system was redesigned for operation at high power, with careful consideration of damage thresholds, clear aperture size, and optical geometry of the cavities. A schematic of this system is shown in Figure 4.2, and Figure 4.3 shows a picture of the stackers taken from above with the beam paths both inside and outside the cavities drawn. The entire stacker is roughly 2.5 feet by 3.5 feet when designed this way, making it compact and easily able to fit on a breadboard.

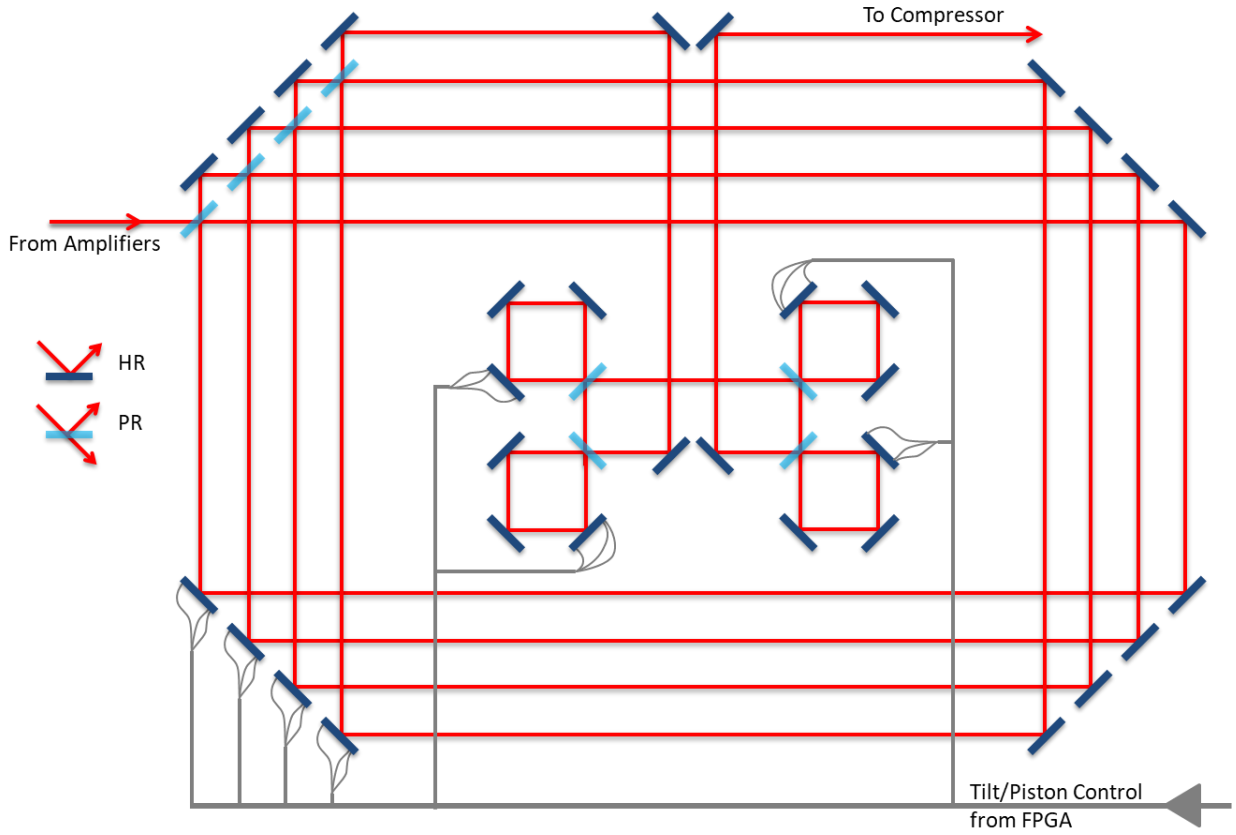


*Figure 4.2: Diagram of stacker system designed for high-power operation, with high-reflectance and partial-reflectance mirrors labeled and control of cavity tilt & piston mirrors shown*

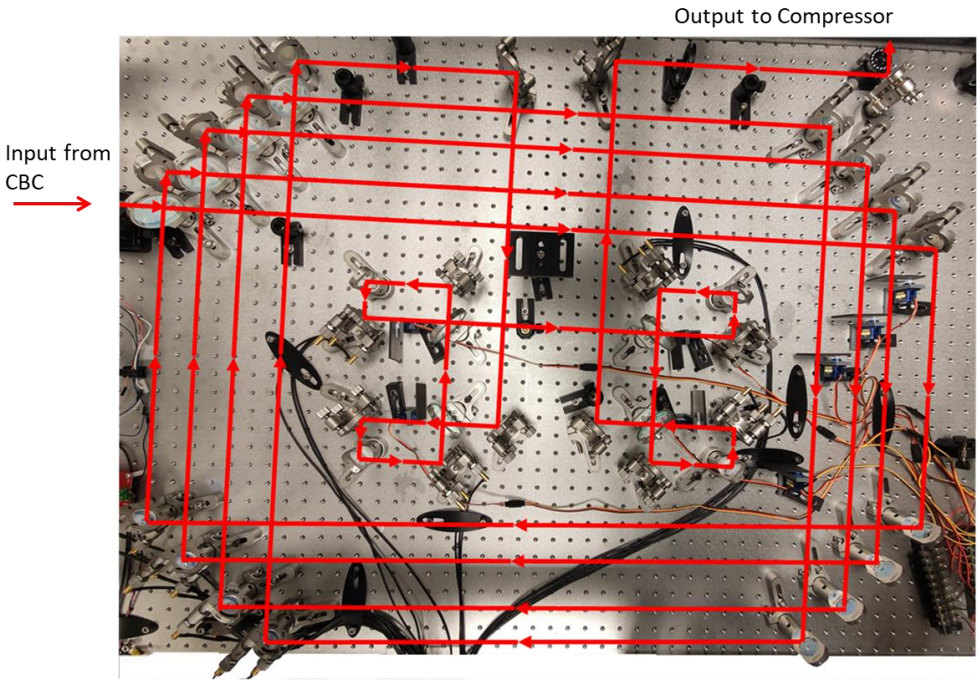


*Figure 4.3: Picture of high-power stacking layout, with optical path drawn for the reference path and the cavities.*

Previous iterations of stacker design had a number of issues and limitations that this new design addresses. Firstly, all cavities consist of an even number of reflections. This is important, as if an odd number of reflections are used, the beam will flip left/right after each round-trip. In theory this isn't a problem assuming a perfect Gaussian beam is used, however if the beam has any asymmetry this can cause stacking degradation. Secondly, 2-inch diameter partially-reflecting mirrors are used to avoid clipping of the beam on entering and exiting the cavities. This is important for throughput efficiency, as well as for stacking performance. These custom beamsplitters have a reflectance $R = 0.57$, whereas in previous designs the values were vastly different from optimal design due to manufacturer uncertainties. Thirdly, very highly reflecting mirrors with low GDD being used (042-1030HHR) inside the cavities, increasing throughput and stacking performance. Lastly, mirrors and partial-reflectors all have a laser-induced damage threshold $LIDT = 10\frac{J}{cm^2}$, which using a beam radius $w_0 = 3mm$, corresponds to an optical damage threshold of 1.41 J. This allows spatial combining to scale to ten channels, providing 100

mJ and still operating ten-times below the damage threshold. In future systems with higher energies, the beam size will need to be increased.

In addition to these optical changes, control changes have also been improved, with individual control of piezoelectric knobs in the cavity, enabling automated tilt control in addition to piston. This allows us to implement the alignment procedures outlined in Sections 3.4 and 3.5, achieving greater accuracy. Also implemented is automated blocking and unblocking of each cavity, controlled by the operator. This means during high-power operation cavities can be controlled without disturbing the experiment.

### 4.4 Coherent Beam Combining Setup

The coherent beam combining (CBC) setup consists of four parallel chirally coupled core (CCC) fiber amplifiers, with splitting and combining optics before and after the setup, respectively. A diagram of this setup can be seen in Figure 4.4, where a series of half-wave and quarter-wave plates are used to split the input into four spatial copies. Piezoelectric mirrors at the input are used to control the phase of each spatial channel, and a series of 50/50 beamsplitters are used as combining elements at the output. A 4% wedge is used to sample the output for controls feedback.

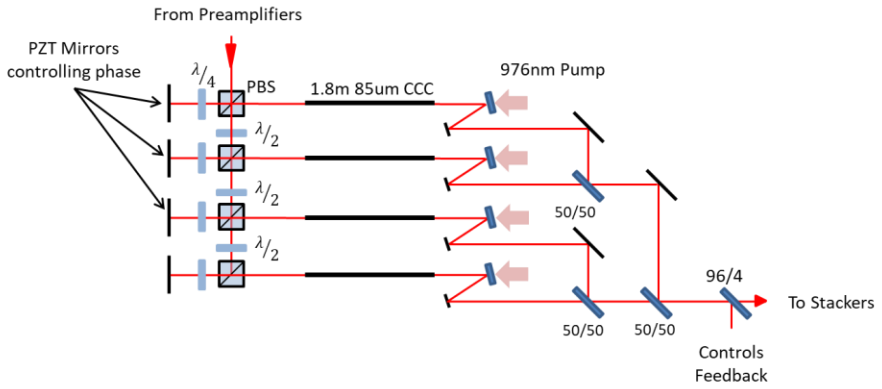


*Figure 4.4: Diagram of spatial combining setup with four parallel amplification channelswhere 50% beamsplitters are used as the combining elements, courtesy of Alexander Rainville [45]*

### 4.5 Pulse Burst Control with FPGA-Based Controls Scheme

Having precise control over all of the aspects and devices in the system is crucial to operating with simultaneous CBC & CPSA. A modified diagram of Figure 4.2 can be seen below in Figure 4.5 which outlines the controls used in the operation of the system. Using a field-programmable gate array (FPGA), synchronous and precise control of all the devices is enabled.

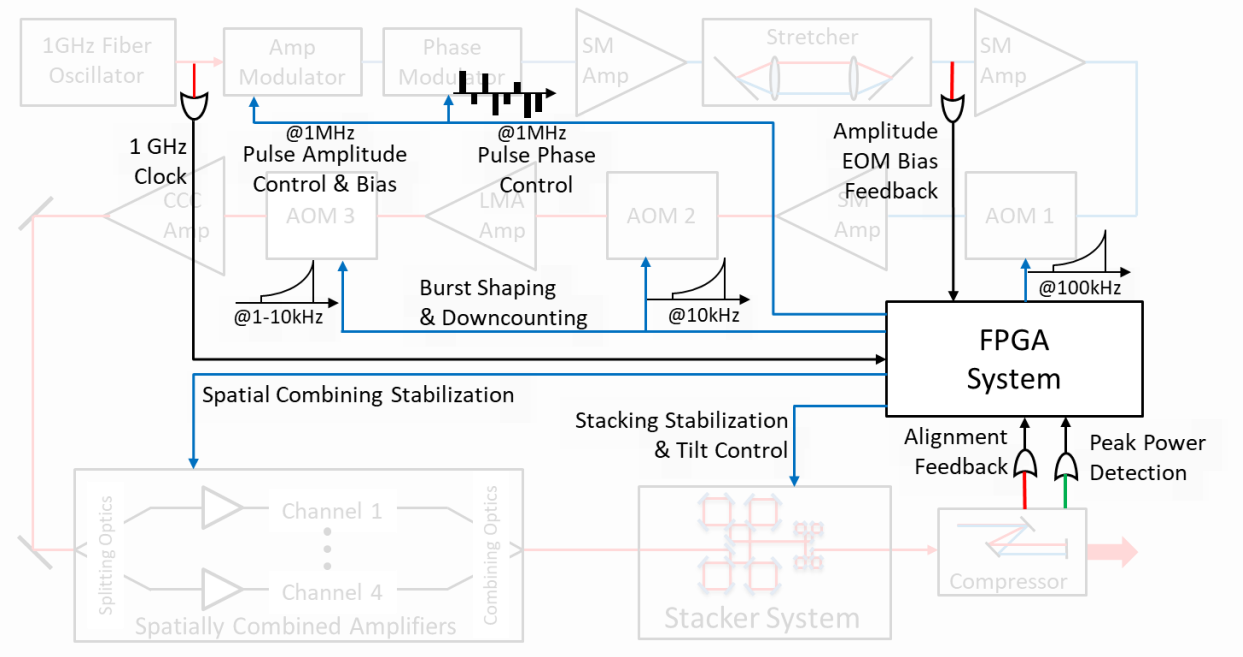


*Figure 4.5: FPGA-based controls schematic of CBC & CPSA system*

The FPGA is clocked using the pulse train output of the oscillator, meaning it operates synchronously with the pulses with low jitter (<200 fs). Then, the FPGA outputs fast (1 GS/s) DAC outputs to control the amplitude and phase electro-optic modulators (EOMs). Since the FPGA creates the burst, it can also set the burst repetition rate to whatever value is desired. Here, we use $f_{burst} = 1\ MHz$. After the stretcher, a feedback photodiode is used to ensure the bias of the amplitude EOM is properly set. In the amplification stages, the acousto-optic modulators are written to with fast DAC outputs such that the burst is not only down-counted, but also shaped. By applying a ramped window to the AOM, the front of the pulse is able to be dampened to

compensate for gain saturation effects occurring in the pre-amplifier stages. Each of the three AOMs used can have a uniquely controlled shape and delay, allowing for precise burst shape control throughout the system. Finally, synchronous reading of second harmonic generation (SHG) as well as acquisition of the pulse train using 1 GS/s ADCs are used as feedback for different controls schemes, such as stabilization of stacking and stacker alignment.

### 4.6 High-Power Alignment Techniques

Alignment techniques for high-precision stacker alignment have been developed in Sections 3.4 & 3.5, however they require using a single-cavity stacking profile. At high energy, such a profile cannot be used, as it would have much too high peak power for the final amplification stages and could cause damage. Instead, what can be done is appending the single-cavity stacking profiles after the main burst, seen in Figure 4.6. Because two different length cavities are used (1 ns and 9 ns round-trip times), two different alignment bursts are required.

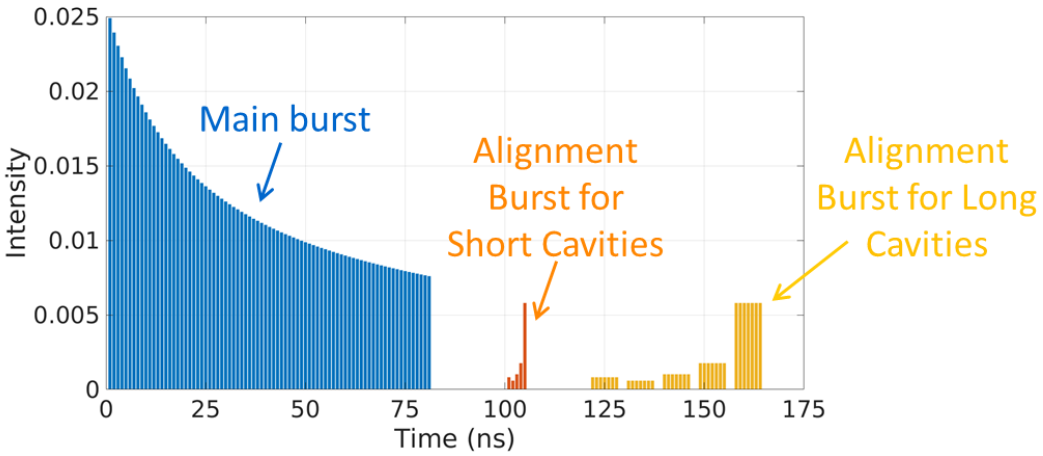


*Figure 4.6: Single-cavity stacking profiles appended after main stacking burst can be used to align cavities during high-power operation*

By appending the bursts after the main sequence of pulses, they can either be carved out by an AOM after alignment is finished, or left where they are and will simply manifest as post-pulses, which for most laser-plasma interactions do not matter. However, SHG cannot be used

during single-cavity stacking, as the main burst has much more power than the alignment bursts and the proper stacking position will not be found. Instead, we can use a 2 GHz photodiode that is input into the FPGA to read the pulse burst, and implement the alignment techniques this way. This enables us to perform both tilt and timing control of the cavities with the high-energy burst shape, providing a method for achieving good stacking and quick realignment if necessary.

### 4.7 Demonstration of Simultaneous CPSA & CBC

Simultaneous CPSA & CBC has been demonstrated with spatial combining of four amplifier channels operating at a variety of burst energy levels. For all of the following results the output burst repetition rate is 2 kHz. First, we test operation with only 1 mJ out of each amplifier, in order to determine a baseline for stacking using this new system. This stacking can be seen in Figure 4.7, with the stretched measurement on the left with an inset of the input burst, and the compressed measurement on the right. This stacking has a calculated stacking efficiency $\eta = 79.1\%$, which is only slightly degraded from the low-power results reported in Section 3.7, providing a solid benchmark for stacking while scaling channel energies further.

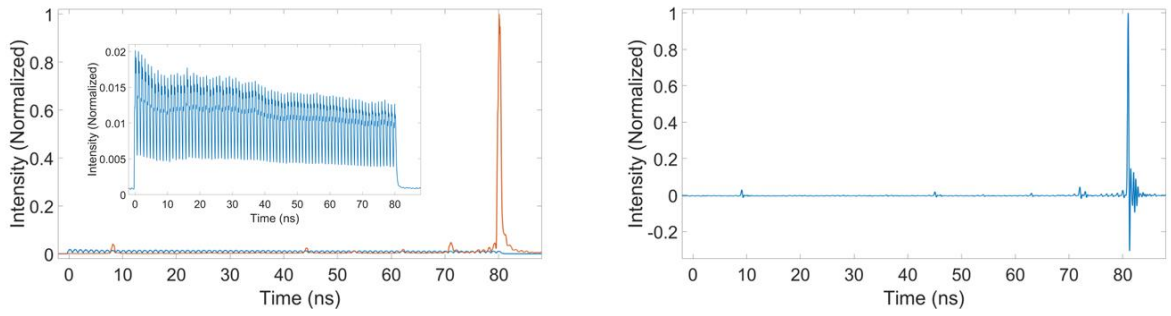


*Figure 4.7: Stacking of 1mJ per channel, (left) stacking trace measured with fast photodiode before compressor in orange, with inset of input burst shape in blue also plotted on the same scale as stacked burst, (right) stacking trace measured with 2.5 GHz photodiode after compressor*

Next, we can look at how a saturated burst shape affects stacking operation. The energy is scaled to 5 mJ per channel and stacked, shown in Figure 4.8. As the burst becomes more

saturated, we see a decrease in the stacking efficiency, dropping to $\eta = 69.6\%$. It is worth noting that, due to the spectral-temporal mapping of the stretched pulses, we can see the spectral shape of the reject pulses are not the same as the stacked pulse. This indicates some spectral effects are occurring, pointing to cavity timing errors, non-flat nonlinear phase across the burst, or spectral shape changes across the burst. These effects need to be further investigated in order to increase stacking efficiency with high saturation.

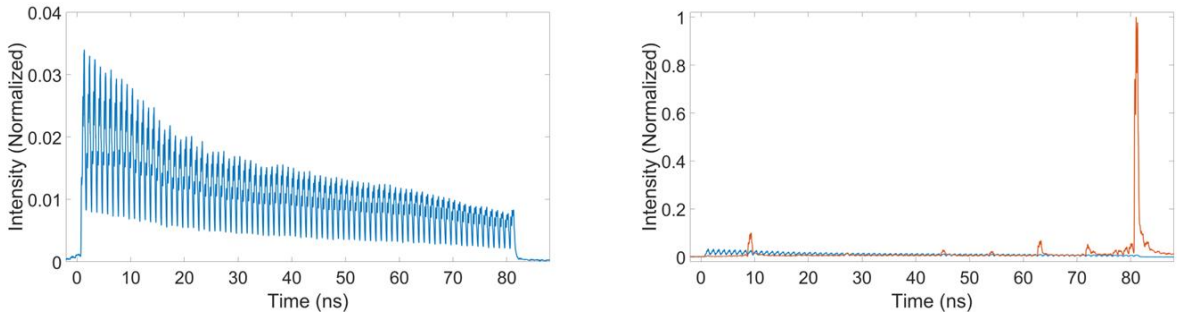


*Figure 4.8: Stacking of 5mJ per channel, (left) pulse burst input into the stacker system, (right) stacking output in orange measured with stretched photodiode with input burst scaled appropriately*

Lastly, we scale the energy to a record pulse energy per channel of 7 mJ in the spatial combining setup, and analyze what impact spatial combining has on stacking performance. In Figure 4.9, both single-channel and four-channel operation are stacked and measured. The single-channel operation achieves a stacking efficiency of $\eta = 70.5\%$, and four-channel combining operation achieves a stacking efficiency of $\eta = 69.3\%$. This efficiency difference is negligible, and is within the tolerance of day-to-day operation. This means spatial combining stabilization does not degrade stacking performance, which demonstrates the viability of this approach.

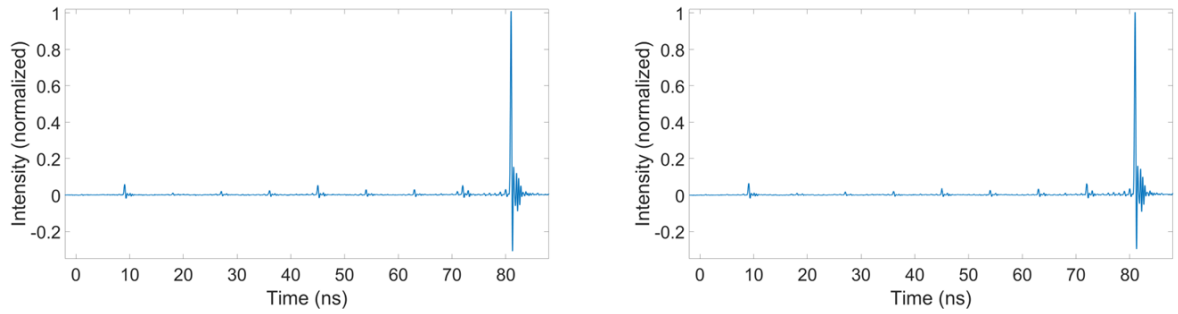


*Figure 4.9: Stacking of 7mJ per channel, with (left) single and (right) four-channel output from the spatial combining setup, measured with compressed photodiode*

Operating at 7 mJ from a fiber amplifier, a compressed pulse duration of 360 fs is measured. Similar to low-power operation, stacking does not change the compressed pulse duration. Additionally, while running at 7 mJ per channel with 4-channel combining, stacked pulse stability is measured and shown in Figure 4.10. Over the 6 minutes shown, the stacked pulse normalized RMS is 2.2%, demonstrating good stability while spatial combining is running with high energy per channel.

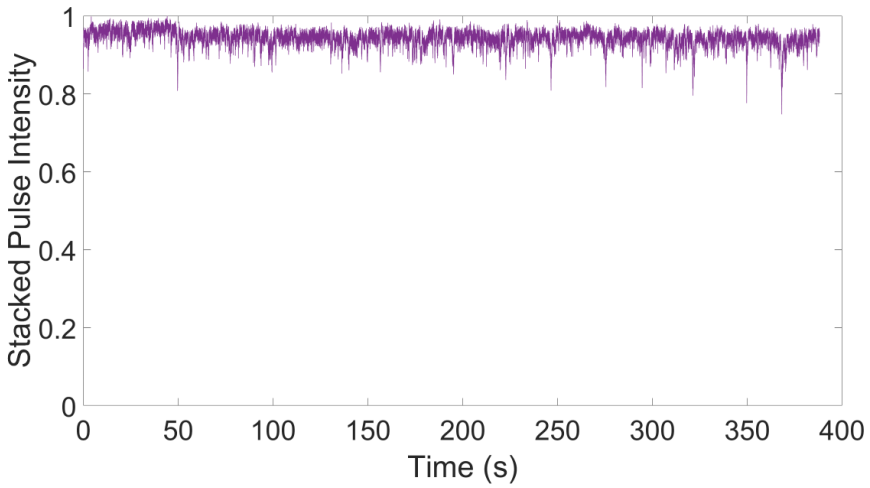


*Figure 4.10: Stacked pulse intensity during 4-channel spatial combining of 7mJ per burst and stacking*

## 4.8 Conclusion of CPSA & CBC System

Simultaneous CPSA & CBC has been demonstrated to be a feasible and scalable approach to increasing energy outputs at high repetition rates. When operating at low

nonlinearity (1 mJ per channel), stacking efficiency only slightly degrades from low-power performance. Upon scaling energies and consequently saturation and nonlinear phase, stacking efficiency lowers some, however this is expected due to non-equal amplitude burst shape. The systems are able to run together with low noise, indicating stability of performance. A record pulse energy per channel is spatially combined with four parallel channels and stacked into a single output pulse with high efficiency. This demonstrates the scalability of this approach, paving the way to scale the number of spatial channels to ten, and achieve 100 mJ output that is spatially and temporally combined.

# Chapter 5 Spectral Synthesis of Pulses via Coherent Spectral Combining

## 5.1 Introduction

Radiography, Z-determination, and active interrogation require quasi-monoenergetic directional gamma ray sources, the leading of which is Thomson scattering. This implementation of Thomson scattering generates high-energy radiation by scattering a laser beam with a head-on electron beam, causing a relativistic Doppler shift of the photons, generating a backwards scattered gamma ray source [46]. Using typical laser drivers in a Thomson scattering system generates gamma photons in a broader spectrum than is required, resulting in reduced contrast and larger doses required. Thus, a quasi-monoenergetic gamma photon source is desirable, which can be generated through specifically tailored optical driving pulses. The desired optical pulse profile is flat-top, bandwidth-limited, 1-10 ps in duration with short rise and fall times, containing around 1 Joule of energy at multi-kilohertz repetition rate. This keeps the interaction in the linear regime, where the energy of scattered gamma rays directly corresponds to the optical pulse envelope.

We propose a laser architecture that will allow for the generation of these driving pulses that is directly compatible with current technologies using coherent beam combining (CBC) and coherent pulse stacking amplification (CPSA). We show how such a system can be integrated and operated in a CPSA laser system, and demonstrate with a proof-of-principle system spectral synthesis of the required spectrum.

## 5.2 Proposed Laser System Architecture

As has been discussed in Chapters 2 & 4 in this thesis, coherent spatial and temporal combining pave the way to high repetition-rate high-energy laser driver sources. These techniques overcome the limitations of fiber amplifiers, specifically their limited transverse aperture size and nonlinear phase accumulation while keeping their advantages, such as high wall-plug efficiency and repetition rates. Integrated with this approach, one can also use coherent spectral combining to synthesize pulse shapes tailored to specific applications.

It is well known that for generation of a near-mono energetic spread of scattered photons in Thomson scattering, the scattering laser pulse must have a pulse duration from 1-10 ps, should be bandwidth-limited (i.e. narrowband), and should as closely resemble a rectangular pulse as possible (i.e. flat-top with fast rise and fall times) [46–48]. However, achieving these parameters in a system delivering 1 Joule pulses at multi-kHz repetition rates poses two major challenges. Firstly, since the desired pulse duration is 1-10 ps, most of the energy is contained within ~3-0.3 nm. This means using conventional CPA methods to stretch the pulse to ~1 ns would require stretchers and compressors that are more than 10 meters long, which is highly impractical. Secondly, because the pulse must have fast rise and fall times, much more spectral content is required to shape the pulse. Therefore, when one stretches the main spectral peak to ~1 ns, the other spectral features must also be accommodated, increasing grating sizes to over 1 meter and further complicating the system.

We address these challenges by leveraging coherent spectral combining along with CPSA. By splitting spectral components into different spectral slices, each spectral component can be amplified and shaped individually, and can be comprised of either a single amplifier stage or an array of fiber amplifier spatially combined, as seen in Figure 5.1. Then, by using CPSA to

increase the energy by a factor of 10, the stretcher/compressor would only require stretching to ~100 ps instead of the typical ~1 ns duration of conventional CPA systems. This enables using stretchers/compressors on the order of 1 meter, and easily manufacturable grating sizes, overcoming the stated challenges and enabling this laser driver design.

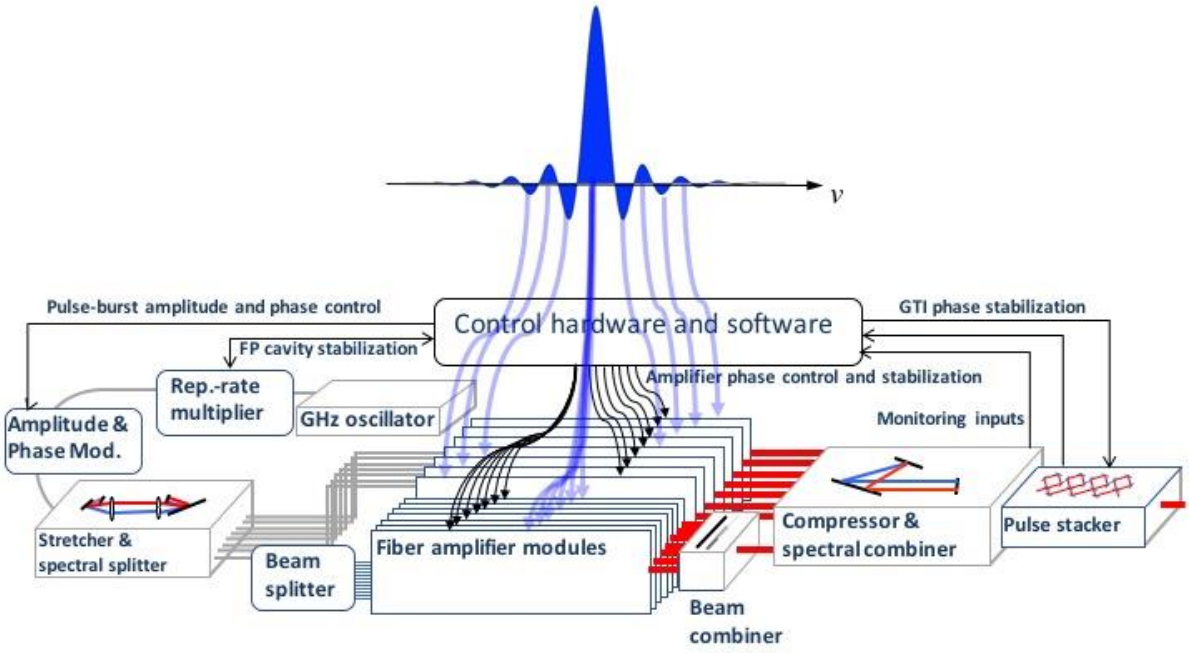


*Figure 5.1: Proposed laser system architecture for synthesis of flat-top bandwidth-limited driver pulses*

Since the ideal pulse shape is a rectangular function with fast rise and fall times and no ripple on top, the corresponding required spectrum to synthesize is a sinc function, shown in Figure 5.2 (a). Here, the pulse duration $\Delta T_p$=1-10 ps, and the pulse rise time $\Delta T_F$=0, as it is instantaneous. This corresponds to the main spectral feature having a bandwidth of $\Delta\nu = 2/\Delta T_P$, which for our specified pulse results in $\Delta\lambda$=3-0.3 nm. However, in order to achieve this ideal pulse shape, an infinitely wide spectrum is required, which is not possible to achieve. The spectrum will be truncated by the grating size, resulting in a finite spectral width, which causes slower rise times and ripple on top of the pulse, as seen in Figure 5.2 (b). The rise times of the

pulse correspond to the spectral width of the function inversely according to $\Delta\nu_{total} = 1/\Delta T_F$. Finite rise times are an unavoidable consequence of having a finite bandwidth, however it is acceptable as long as the rise times are sufficiently shorter than the pulse duration, $\Delta T_F \ll \Delta T_P$. However, amplitude fluctuations on the amplitude of the pulse are very detrimental to the generation of quasi-monoenergetic gamma photons. In order to overcome this limitation, one can apply a smooth envelope to the truncated spectrum, slightly increasing the rise time of the pulse in order to drastically decrease the ripple, as seen in Figure 5.2 (c). This allows us to synthesize a flat-top, bandwidth-limited pulse with a truncated spectrum.

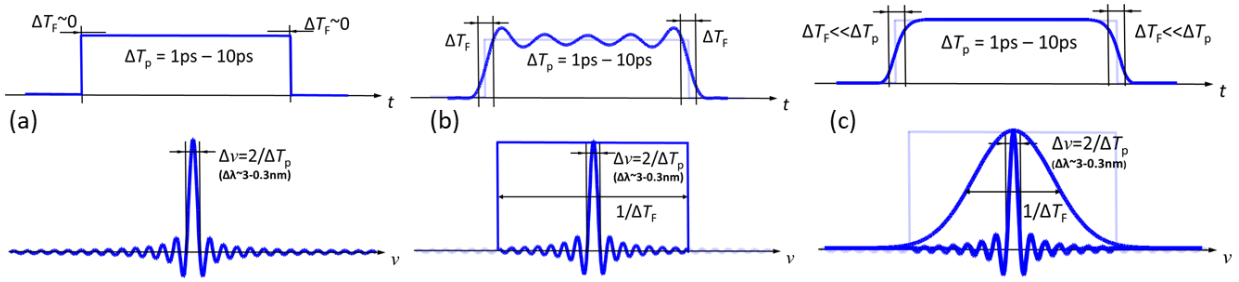


*Figure 5.2: (a) Ideal pulse shape and corresponding spectrum, (b) Truncation of spectrum results in finite rise times and ripple, (c) Smoothing of spectrum reduces ripple*

The required spectral shape being derived from a sinc function is uniquely well-suited to coherent spectral combining. Since the spectral intensity goes to zero between the lobes of the sinc function, it forms natural cutoff points to create disjoint spectral channels. Each channel is comprised of a lobe of the sinc function, with the central lobe twice as wide as the rest. Since the central channel has >95% of the total energy of the pulse for this application, only the central spectral channel requires spatial combining, the rest can use a single fiber amplifier to reach their required energy levels.

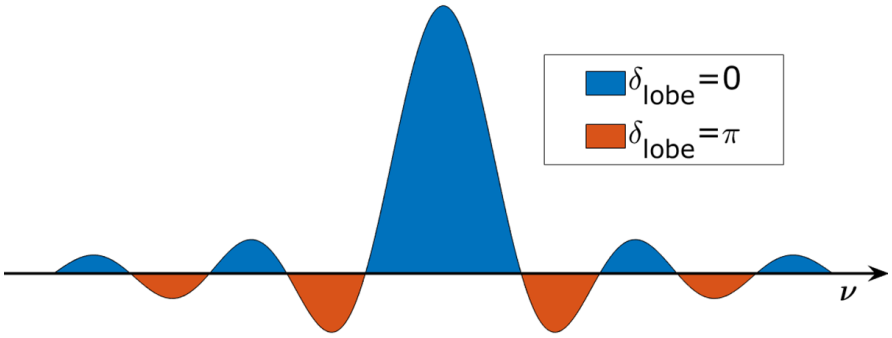


*Figure 5.3: Sinc spectrum with proper phasing to synthesize flat-top pulses*

In order to synthesize the proper pulse shape, each spectral channel needs to be correctly phased relative to the other channels. As can be seen in Figure 5.3, every lobe of the sinc function must have a $\pi$ phase shift relative to its adjacent lobes. Because the absolute phase of the spectrum is irrelevant, we can assume the central lobe has a phase $\delta = 0$. Lobes going out to higher and lower frequencies from the central lobe then have a repeating phase pattern of $\pi$,0, $\pi$,0,… extending on for as many spectral channels as the system has. It is important to have a stabilization scheme to maintain the proper phases of these spectral channels, as will be discussed later in this chapter.

## 5.3 Coherent Spectral Combining Proof-of-Principle System

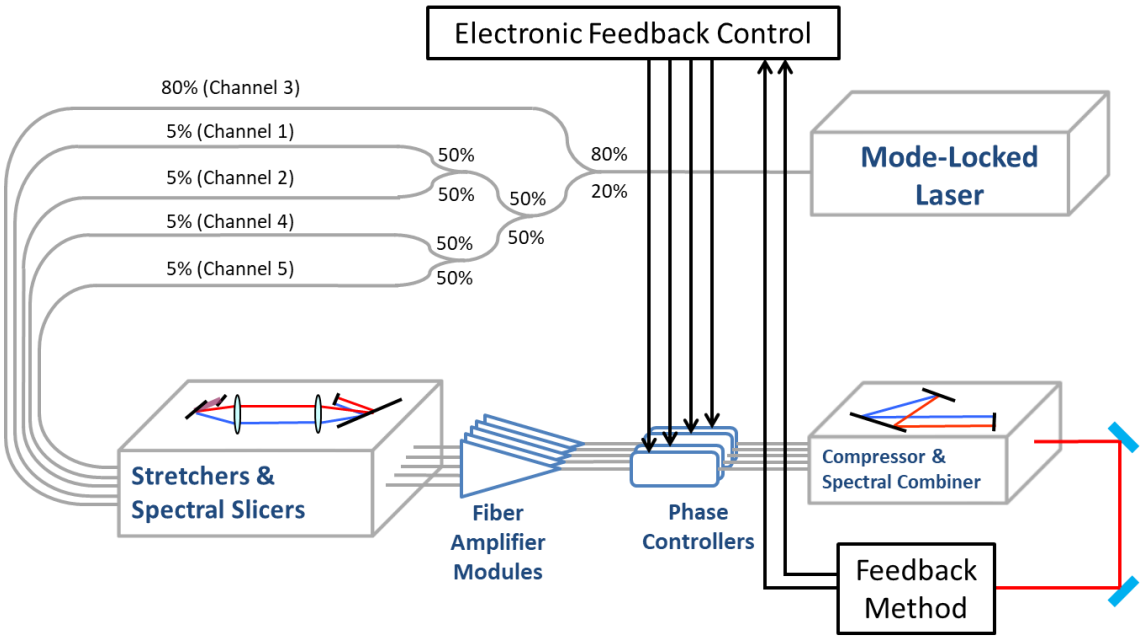


*Figure 5.4: Proof-of-principle Coherent Spectral Combining System*

In order to demonstrate the validity of this approach, a proof-of-principle system is proposed that is designed to synthesize 1 ps pulses using five spectral channels. The layout of this system can be seen in Figure 5.4, which includes the key components of spectral coherent combining. A mode-locked laser seeds the system, and is split into five parallel fibers. The central lobe contains 80% of the original power, and the other four side lobes each contain 5% of the power. This splitting ratio is due to the majority of the power ideally being in the central lobe when recombined. Then, each channel enters its own stretcher, where the pulses are both stretched to 100 ps and spectrally shaped to their corresponding sinc lobes. Each channel is amplified then sent through fiber phase shifters to control each lobe's phase relative to the central channel. Lastly, all five channels enter a compressor where the pulses are re-compressed and combined into a single output. This output can then be used to provide feedback for the phase controllers to keep the pulse shape properly stabilized. The designed spectrum and its

corresponding ideal pulse are shown in Figure 5.5. The spectrum is shaped with a Gaussian envelope to smooth amplitude ripple on top of the pulse, resulting in a 1 ps pulse with 3% ripple and a rise and fall time of 0.23 ps. To achieve faster rise and fall times, more spectral channels would need to be added.

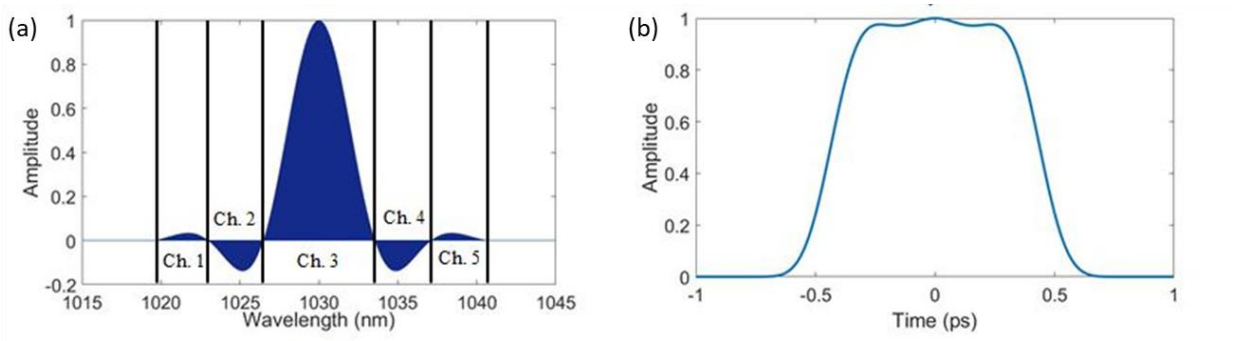


*Figure 5.5: (a) Proof-of-principle five-channel spectrum, (b) Ideal pulse shape for five-channel spectrum*

## 5.4 Spectral splitting & combining

While the sinc shape of the spectrum provides natural separation points for the spectral channels, the spectral features are still very narrow, with the central lobe being 6 nm and the side lobes being 3 nm edge-to-edge. Having multilayer-coating optical filters corresponding to each of these channels is not trivial to design, and would require a unique custom part for each channel. Instead, we can exploit the fact that there is a strong spatial chirp in both the stretcher and compressor after two passes on a grating. At this point, spatial filtering techniques can be employed to shape each spectral channel to its specific profile. A Martinez-style stretcher with spatial filtering of the spatially chirped beam is shown in Figure 5.6 (a) [5]. At the retro-reflecting mirror of the stretcher, a spatial filter can be inserted to shape the spectrum to its desired shape. In the demonstration system, the spatial filter is comprised of two razor blades, each with an adjustable position and angle, as shown in Figure 5.6 (b). The angle and horizontal position of each razor blade are denoted by $\alpha_n$ and $x_n$, respectively. The beam diameter is

denoted by $D_0$, and the central position of the beam is $x_0$. The resulting output spectrum after filtering is expressed in Equation 5.1.

$$P(\lambda) = \frac{P_0}{2}\left\{erf\left[\frac{\sqrt{8}}{D_0}(x_2 - x_0)sin\alpha_2\right] - erf\left[\frac{\sqrt{8}}{D_0}(x_1 - x_0)sin\alpha_1\right]\right\} \quad (5.1)$$

With the proper selection of razor blade angle and position, each spectral channel can be tailored to its specific desired shape.

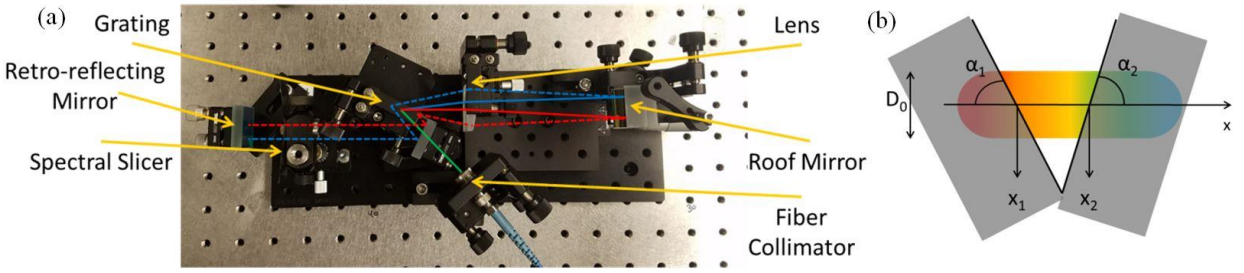


*Figure 5.6: (a) Annotated image of a stretcher with spectral filtering, dashed lines correspond to beams displaced to a different height by the roof mirror, (b) Spectral shaping using two razor blades with adjustable position and angle*

After each spectral channel has proper shaping, their relative intensities need to be adjusted. This is accomplished by varying the amount of amplification each channel sees in its respective amplifier, enabling control of relative channel powers.

Once each channel has its proper shape and amplitude, they are all sent into a Treacy-style compressor [6]. As can be seen in Figure 5.7, all of the spectral channels enter the grating aligned parallel to one another, and are incident upon the grating pair. Since each spectral channel corresponds to a disjoint portion of the spectrum, meaning their spectral content does not overlap, they each emerge at a different height corresponding to their wavelength. This can be leveraged to combine the channels by using a cascaded roof mirror in the compressor. Each channel is reflected using a right-angle prism mirror into a single, continuous chirp that contains the entire spectrum. It then passes through the grating pair again, resulting in a compressed and combined output.

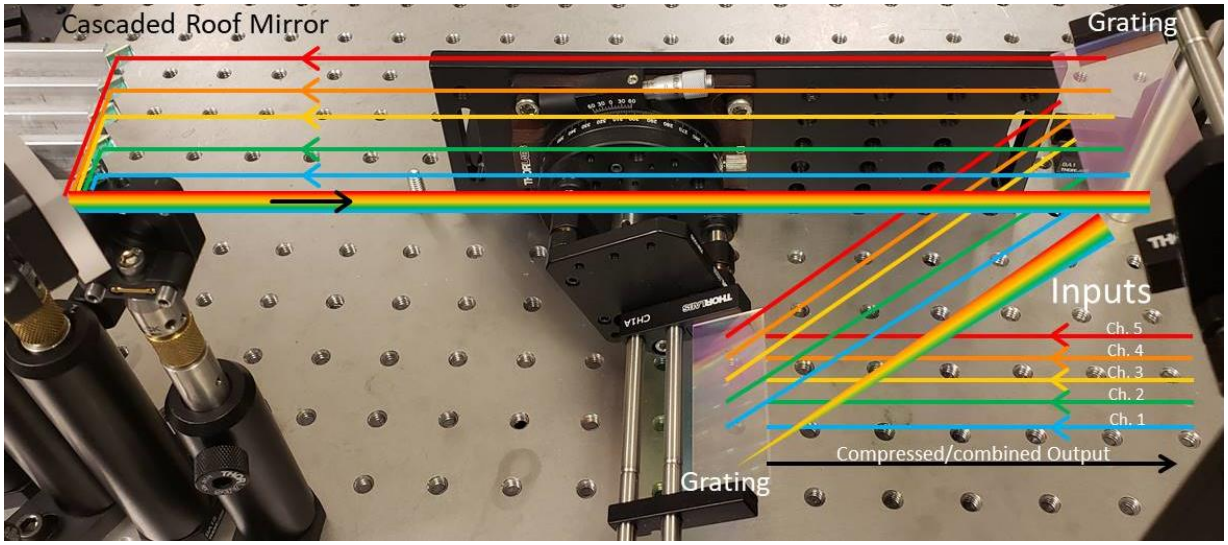


*Figure 5.7: Spectral channels are combined in the compressor utilizing spatial chirp*

## 5.5 Experimental Demonstration of spectral shaping & combining

Using the proof-of-principle system mentioned above, we have demonstrated spectral synthesis of the spectrum corresponding to flat-top, bandwidth-limited pulses. The measured spectrum is shown in Figure 5.8 (a) plotted on a linear scale, with the insert plotted on a logarithmic scale. As can be seen, the side lobes contain very little of the overall power in the pulse. Figure 5.8 (b) shows the calculated pulse shape assuming proper phasing of the channels for the full spectrum, as well as for only the central lobe. The predicted pulse using the full spectrum has less than 4% ripple on its top, and a rise/fall time of 0.27 ps. This is close to the best possible performance using five spectral channels, with the ideal case having 3% ripple and 0.23 ps rise/fall time. If only the central channel is considered, the resulting pulse has a duration of 0.7 ps and a rise/fall time of 0.47 ps. This demonstrates how important the side lobes are to proper pulse synthesis, as even though they contain <4% of the overall power, they are crucial to fast rise times. The addition of more spectral channels would allow for a further decrease in rise time.

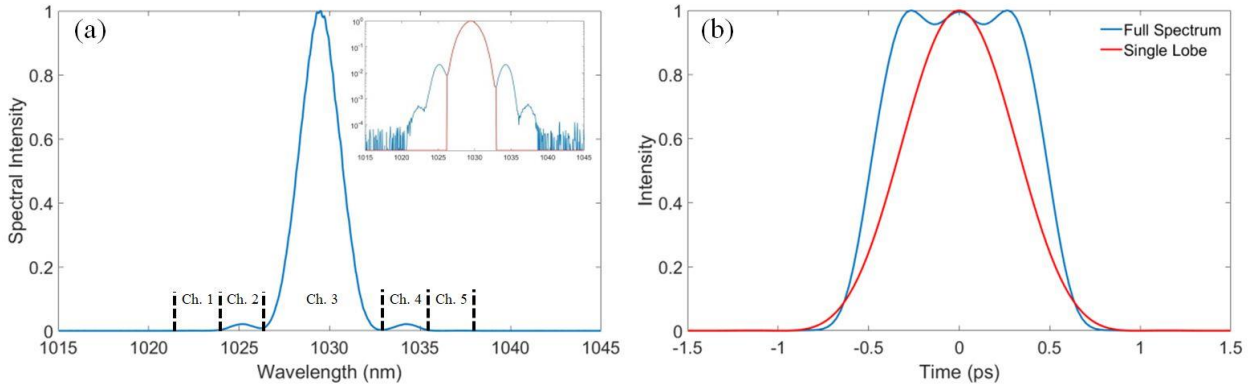


*Figure 5.8: (a) Measured spectrum from combined output of compressor, insert is plotted on logarithmic scale, (b) Calculated output pulse from measured spectrum assuming proper channel phasing*

## 5.6 Phase stabilization of Pulse Shape

Once proper spectral shaping is achieved, the relative phases of the spectral channels need to be stabilized to their correct values. As stated previously, for a sinc-function spectrum, the proper phasing is a $\pi$ phase shift between adjacent channels. Since the absolute phase of the pulse is unimportant, we can assume that the central channel has a phase $\delta_3 = 0$, and all other channels are phased relative to this.

Control of the phase of each channel is important as well. This can be achieved a number of ways, all with their own advantages and drawbacks, however we primarily look at using piezo-electric chips made from lead zirconate titanate (PZT). This allows a control voltage to correspond to a mechanical movement on a fast (kHz) timescale, enabling phase control. Piezos can be utilized to push a mirror forward and backward, or to stress a fiber and cause stress-induced birefringence to change the optical path length. In this system, we propose using fiber phase-shifters that utilize stress-induced birefringence, which enable feedback at >20 kHz speeds, and give a controllable phase range of $>8\pi$.

The most important aspect for phase stabilization of the spectral channels is the feedback mechanism. This poses a challenge, as using an ultrafast time-domain measurement of a few-

picosecond pulse, or alternatively a spectral-domain measurement of the phases of different channels is technically daunting and has speed limitations associated with it. A combined feedback metric would be preferred, however conventional feedback metrics used for other coherent combining methods such as CPSA and CSC do not result in the desired pulse shape. The average power of the output does not change with phase changes to the channels, and maximizing the peak power of the pulse does not give the optimal shape either.

Since the pulse is intended to minimize ripple on top of the profile, one approach is to minimize peak power. This can be accomplished by using second harmonic generation (SHG) and minimizing the resulting signal. For this analysis, a beta barium borate (BBO) crystal is considered, with a thickness of 1 mm such that the entire spectrum is properly phase-matched. Then, to ensure this is a valid feedback metric, the 4-dimensional phase space is scanned and the SHG is calculated for each pulse shape. 2D slices of this scan are shown in Figure 5.9, where each axis corresponds to the deviation from idea phase for one of the spectral channels. As shown in Figure 5.5, channels are numbered 1 to 5 with increasing wavelength. The central channel is numbered channel 3, and its phase remains fixed at 0 in this simulation, as only relative phases need to be considered when analyzing pulse shape. Only three slices are shown in Figure 5.9 due to the symmetry of the parameter space. For example, comparing channels 1 & 2 results in the same curve as comparing channels 1 & 4, 2 & 5, and 4 & 5. Thus, these three slices give insight to the majority of the parameter space, allowing us to get a sense of the high-dimensional parameter space. Of course, the entire parameter space is simulated and checked for global and local maxima/minima, to ensure that no undesirable points exist that could obstruct the stabilization algorithm.

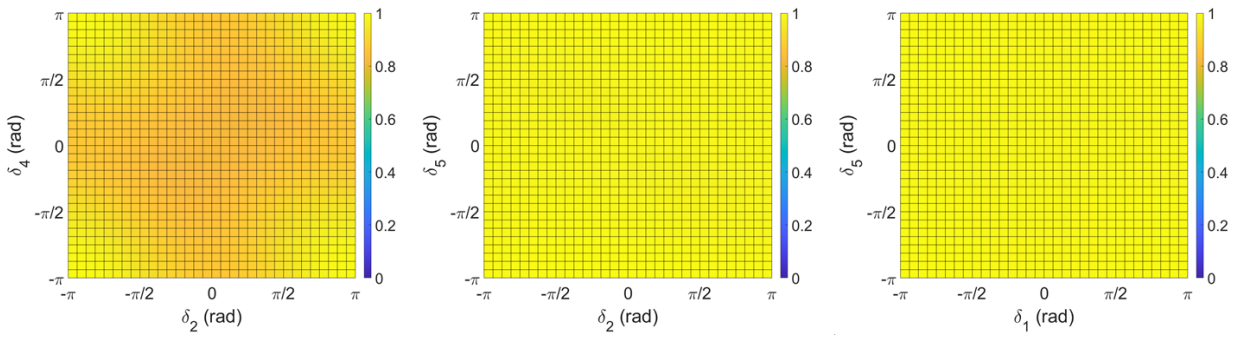


*Figure 5.9: 2D cross-sections of phase parameter space for SHG, from left to right comparing channels 2 & 4, channels 2 & 5, and channels 1 & 5*

Since each axis denotes the deviation from idea phase, the central point is the desired phase for flat-top pulse synthesis. And indeed, we find that the desired pulse shape is both the global minimum and the only local minimum, meaning in theory minimization of SHG could be used to stabilize the pulse shape. However, in order for a feedback metric to stabilize well, it must be sensitive to parameter changes. We will analyze this by looking at the contrast, defined in Equations 5.2 and 5.3 for the two inner and outer spectral channels, respectively. It is useful to analyze the spectral channels in pairs around the central channel due to the inherent symmetry of the parameter space.

$$C_{inner} = 1 - \frac{min\,(SHG(\delta_2,\delta_4))}{max\,(SHG(\delta_2,\delta_4))} \tag{5.2}$$

$$C_{outer} = 1 - \frac{min\,(SHG(\delta_1,\delta_5))}{max\,(SHG(\delta_1,\delta_5))} \tag{5.3}$$

Using these, we find $C_{inner} = 17.7\%$ and $C_{outer} = 1.6\%$. These contrast ratios are quite small, meaning minimization of SHG is not a sensitive feedback method, and is not suitable to this application.

Instead of minimizing SHG, we can go further and use fourth harmonic generation (FHG) as a feedback metric. Again, the phase parameter space is scanned in all four dimensions, and slices of the channel phases are shown in Figure 5.10.

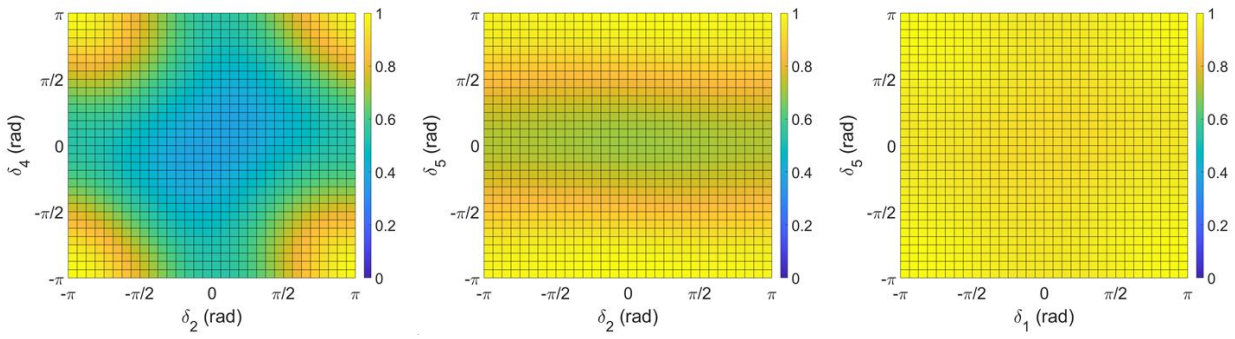


*Figure 5.10: 2D cross-sections of phase parameter space for FHG, from left to right comparing channels 2 & 4, channels 2 & 5, and channels 1 & 5*

The parameter space topography is almost identical to the SHG case, except with increased contrast. Using FHG, we calculate contrast ratios of $C_{inner} = 62.4\%$ and $C_{outer} = 8.47\%$. This is substantially improved, and promising. However, spectral filtering methods can be used to increase the contrast further.

Modification of the spectrum used as phase stabilization feedback can allow for an even more sensitive feedback metric. Specifically, the outer channels contain so little of the total power (<1%) that they have rather small impacts on the FHG. This can be addressed by dampening the central and inner channel intensities via spectral filtering. This makes the outer channels have a larger impact on the overall pulse, as can be seen in Figure 5.11. By dampening the central channel to 25% of its designed power and the inner channels to 50% of their designed power, the FHG contrast becomes $C_{inner} = 74\%$ and $C_{outer} = 20.7\%$. Once again, the entire parameter space is searched, and the flat-top pulse shape remains both the global minimum and the only local minimum. This means by spectral filtering the feedback input to dampen the large spectral features and using FHG, a suitable feedback metric for stabilization of spectral channel phases can be generated.

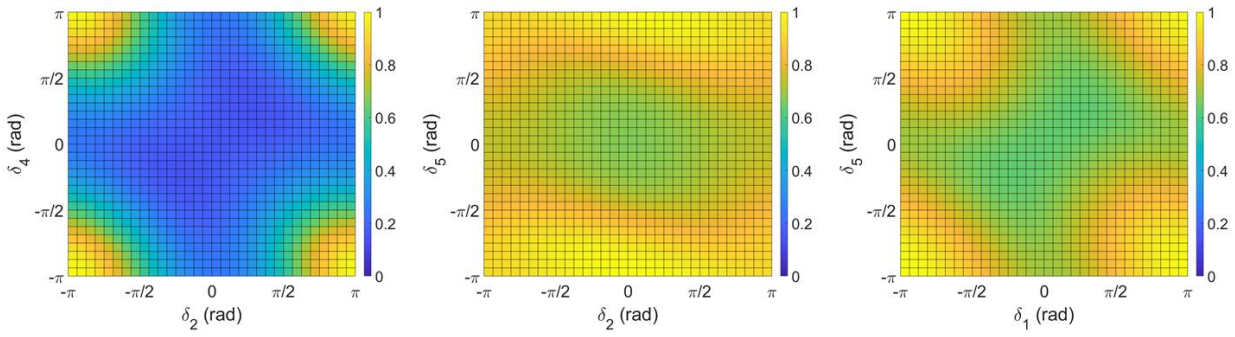


*Figure 5.11: 2D cross-sections of phase parameter space for FHG with dampening of spectral lobes, from left to right comparing channels 2 & 4, channels 2 & 5, and channels 1 & 5*

## 5.7 Spectral Synthesis Conclusion

Coherent spectral combining can be used to synthesize specific laser-driver pulse shapes tailored for applications, specifically shown here for flat-top bandwidth-limited pulses. Methods for spectral shaping, combining, and phasing are shown that are directly compatible with coherent beam combining and coherent pulse stacking amplification fiber laser systems. Spectral splitting and combining of the proper spectrum for flat-top 1-10 ps pulses is demonstrated in a test system, and a phase stabilization method is proposed.

# Chapter 6 Conclusions & Future Work

## 6.1 Conclusions

This thesis work has developed theoretical understanding and experimental techniques for robust, repeatable high-efficiency coherent pulse stacking amplification (CPSA). These advancements have allowed for simultaneous coherent beam combining and CPSA to be demonstrated for the first time with record high energy per fiber while maintaining high stacking efficiency.

Theoretical understanding of CPSA has been further developed, providing the framework for higher stacking efficiencies and pre-pulse contrast to be achieved, and exposing the adaptability of the technique. A GTI stacker system was shown to be mathematically equivalent to a deep recurrent neural network, which provides better understanding of cavity design as well as cavity phase stabilization. Coherent pulse stacking was shown to be able to stack different input burst shapes with only a minor degredation of efficiency and pre-pulse contrast, showing its adaptable nature. Additionally, a method for achieving higher pre-pulse contrast by allowing post-pulses was further developed both for an equal-amplitude input as well as for an equal nonlinear phase input. Errors on stacking parameters are analyzed, and both pulse phase errors are shown as the primary source of degredation. Optimization of pulse phases is proposed as a solution to this problem.

Stacking alignment errors were quantified using a mathematical model to determine the resulting stacking efficiency loss. From this, required alignment tolerances were derived. Techniques to meet these tolerances were developed and implemented, increasing alignment

accuracy of tilt alignment to <5 μrad and piston alignment to <2μm. Additionally, the repetition rate of the mode-locked laser seed was fixed to a highly stable RF frequency standard, which reduced jitter and drift of the system, and enabled stable operation. High efficiency stacking of >80% stacking efficiency was shown to be repeatable and robust, with stabilization noise of <1% RMS.

Simultaneous coherent beam combining and CPSA is demonstrated using four spatial channels and a 4+4 stacker system. Automated alignment techniques are implemented for high-power operation, and a complex control system is built to enable stacking burst creation, shaping, alignment, and stabilization. Using these, a record high 7 mJ per fiber is spatially combined and stacked into a single pulse with 70% stacking efficiency and stabilization noise of 2.2% RMS. Spatial combining and stacking are shown to not have a detrimental effect on stacking efficiency compared to single-channel operation. This paves the way for achieving 100 mJ pulses at multi-kHz repetition rates.

Methods for shaping an output pulse to be flat-top and bandwidth-limited in an energy-scalable manner were developed and demonstrated. A spectral sinc function corresponding to flat-top bandwidth-limited pulses was experimentally synthesized in a chirped pulse amplification system demonstration. A phase feedback method for stabilization of spectral channel phases was derived, enabling a process for the creation of the desired pulse shape.

### 6.2 Future Work

There are many next steps to take to further improve stacking performance. A pulse pre-burst can be included during stacking, enabling higher efficiency and pre-pulse contrast. This will require splitting part of the seed off and shaping it separately to avoid gain saturation effects, however it can drastically improve pre-pulse contrast which is important for many laser-matter

interactions. Additionally, stacking can be extended to a higher number of pulses by exploring other multiplex stacker designs. This would allow for operation at a lower level of saturation in the amplifiers, resulting in lower nonlinear phase accumulated by the burst which should increase stacking efficiency.

Pre-pulse contrast can be a major factor for light-matter interactions, and using a pre-burst may not be sufficient on its own. If higher pre-pulse contrast is required, nonlinear effects can be used to reduce the peak power of the pre-pulses, increasing the ratio. Additionally, designs are being explored to use a few cavities to re-shape the equal nonlinear phase burst into a flat-top burst. This would allow the stackers to operate much closer to the ideal case, increasing both efficiency and pre-pulse contrast.

In addition to stacking improvements, a larger number of spatial amplifier channels can be used to further increase output pulse energies. This will allow for bursts >100 mJ to be synthesized in a manner that is stackable into a single pulse, resulting in a high-energy laser source at multi-kHz repetition rates. The work done in this thesis provides the foundation upon which these goals can be achieved.

## Bibliography


1. T. H. Maiman, "Stimulated Optical Radiation in Ruby," Nature **187**(4736), 493–494 (1960).
2. W. E. Lamb, "Theory of an Optical Maser," Phys. Rev. **134**(6A), A1429–A1450 (1964).
3. L. E. Hargrove, R. L. Fork, and M. A. Pollack, "Locking of He-Ne Laser Modes Induced by Synchronous Intracavity Modulation," Appl. Phys. Lett. **5**(1), 4–5 (1964).
4. D. Strickland and G. Mourou, "Compression of amplified chirped optical pulses," Opt. Commun. **56**(3), 219–221 (1985).
5. O. E. Martinez, J. P. Gordon, and R. L. Fork, "Negative group-velocity dispersion using refraction," JOSA A **1**(10), 1003–1006 (1984).
6. E. Treacy, "Optical pulse compression with diffraction gratings," IEEE J. Quantum Electron. **5**(9), 454–458 (1969).
7. C. N. Danson, C. Haefner, J. Bromage, T. Butcher, J.-C. F. Chanteloup, E. A. Chowdhury, A. Galvanauskas, L. A. Gizzi, J. Hein, D. I. Hillier, N. W. Hopps, Y. Kato, E. A. Khazanov, R. Kodama, G. Korn, R. Li, Y. Li, J. Limpert, J. Ma, C. H. Nam, D. Neely, D. Papadopoulos, R. R. Penman, L. Qian, J. J. Rocca, A. A. Shaykin, C. W. Siders, C. Spindloe, S. Szatmári, R. M. G. M. Trines, J. Zhu, P. Zhu, and J. D. Zuegel, "Petawatt and exawatt class lasers worldwide," High Power Laser Sci. Eng. **7**, e54 (2019).
8. H. T. Nguyen, J. A. Britten, T. C. Carlson, J. D. Nissen, L. J. Summers, C. R. Hoaglan, M. D. Aasen, J. E. Peterson, and I. Jovanovic, "Gratings for high-energy petawatt lasers," in *Laser-Induced Damage in Optical Materials: 2005* (SPIE, 2006), **5991**, pp. 488–495.
9. "Chirped-Pulse Amplification – Laboratory for Laser Energetics," (n.d.).
10. W. Li, Z. Gan, L. Yu, C. Wang, Y. Liu, Z. Guo, L. Xu, M. Xu, Y. Hang, Y. Xu, J. Wang, P. Huang, H. Cao, B. Yao, X. Zhang, L. Chen, Y. Tang, S. Li, X. Liu, S. Li, M. He, D. Yin, X. Liang, Y. Leng, R. Li, and Z. Xu, "339 J high-energy Ti:sapphire chirped-pulse amplifier for 10 PW laser facility," Opt. Lett. **43**(22), 5681–5684 (2018).
11. E. Sistrunk, D. A. Alessi, A. Bayramian, K. Chesnut, A. Erlandson, T. C. Galvin, D. Gibson, H. Nguyen, B. Reagan, K. Schaffers, C. W. Siders, T. Spinka, and C. Haefner, "Laser Technology Development for High Peak Power Lasers Achieving Kilowatt Average Power and Beyond," in *Short-Pulse High-Energy Lasers and Ultrafast Optical Technologies* (SPIE, 2019), **11034**, p. 1103407.
12. X. Ma, C. Zhu, I.-N. Hu, A. Kaplan, and A. Galvanauskas, "Single-mode chirally-coupled-core fibers with larger than 50μm diameter cores," Opt. Express **22**(8), 9206–9219 (2014).
13. J. Limpert, F. Stutzki, F. Jansen, H.-J. Otto, T. Eidam, C. Jauregui, and A. Tünnermann, "Yb-doped large-pitch fibres: effective single-mode operation based on higher-order mode delocalisation," Light Sci. Appl. **1**(4), e8–e8 (2012).
14. J. Ruppe, "Theoretical and Experimental Foundations of Coherent Pulse Stacking Amplification," Thesis (2017).

15. A. Rainville, M. Chen, M. Whittlesey, Q. Du, and A. Galvanauskas, "22mJ Coherent Beam Combining from Three 85μm Core CCC Fiber Amplifiers," in *2021 Conference on Lasers and Electro-Optics (CLEO)* (2021), pp. 1–2.
16. T. Zhou, J. Ruppe, C. Zhu, I.-N. Hu, J. Nees, and A. Galvanauskas, "Coherent pulse stacking amplification using low-finesse Gires-Tournois interferometers," Opt. Express **23**(6), 7442–7462 (2015).
17. H. Pei, J. Ruppe, S. Chen, M. Sheikhsofla, J. Nees, Y. Yang, R. Wilcox, W. Leemans, and A. Galvanauskas, "10mJ Energy Extraction from Yb-doped 85μm core CCC Fiber using Coherent Pulse Stacking Amplification of fs Pulses," in *Laser Congress 2017 (ASSL, LAC) (2017), Paper AW4A.4* (Optica Publishing Group, 2017), p. AW4A.4.
18. S. Zhou, F. W. Wise, and D. G. Ouzounov, "Divided-pulse amplification of ultrashort pulses," Opt. Lett. **32**(7), 871–873 (2007).
19. M. Kienel, A. Klenke, T. Eidam, S. Hädrich, J. Limpert, and A. Tünnermann, "Energy scaling of femtosecond amplifiers using actively controlled divided-pulse amplification," Opt. Lett. **39**(4), 1049–1052 (2014).
20. H. Stark, M. Müller, M. Kienel, A. Klenke, J. Limpert, and A. Tünnermann, "Electro-optically controlled divided-pulse amplification," Opt. Express **25**(12), 13494–13503 (2017).
21. M. Kienel, A. Klenke, T. Eidam, M. Baumgartl, C. Jauregui, J. Limpert, and A. Tünnermann, "Analysis of passively combined divided-pulse amplification as an energy-scaling concept," Opt. Express **21**(23), 29031–29042 (2013).
22. M. Kienel, M. Müller, A. Klenke, J. Limpert, and A. Tünnermann, "12 mJ kW-class ultrafast fiber laser system using multidimensional coherent pulse addition," Opt. Lett. **41**(14), 3343–3346 (2016).
23. H. Stark, J. Buldt, M. Müller, A. Klenke, A. Tünnermann, and J. Limpert, "23 mJ high-power fiber CPA system using electro-optically controlled divided-pulse amplification," Opt. Lett. **44**(22), 5529–5532 (2019).
24. M. Müller, C. Aleshire, L. H. Stark, J. Buldt, A. Steinkopff, E. Haddad, F. Legare, A. Klenke, A. Tünnermann, and J. Limpert, "10.4 kW 12-channel ultrafast fibre laser," in *Laser Congress 2020 (ASSL, LAC) (2020), Paper ATu4A.2* (Optica Publishing Group, 2020), p. ATu4A.2.
25. Q. Du, D. Wang, T. Zhou, D. Li, and R. Wilcox, "81-beam coherent combination using a programmable array generator," Opt. Express **29**(4), 5407–5418 (2021).
26. D. Wang, Q. Du, T. Zhou, D. Li, and R. Wilcox, "Stabilization of the 81-channel coherent beam combination using machine learning," Opt. Express **29**(4), 5694–5709 (2021).
27. I. Fsaifes, L. Daniault, S. Bellanger, M. Veinhard, J. Bourderionnet, C. Larat, E. Lallier, E. Durand, A. Brignon, and J.-C. Chanteloup, "Coherent beam combining of 61 femtosecond fiber amplifiers," Opt. Express **28**(14), 20152–20161 (2020).
28. P. Ma, H. Chang, Y. Ma, R. Su, Y. Qi, J. Wu, C. Li, J. Long, W. Lai, Q. Chang, T. Hou, P. Zhou, and J. Zhou, "7.1 kW coherent beam combining system based on a seven-channel fiber amplifier array," Opt. Laser Technol. **140**, 107016 (2021).
29. W. Chang, T. Zhou, L. A. Siiman, and A. Galvanauskas, "Femtosecond pulse spectral synthesis in coherently-spectrally combined multi-channel fiber chirped pulse amplifiers," Opt. Express **21**(3), 3897–3910 (2013).
30. P. Rigaud, V. Kermene, G. Bouwmans, L. Bigot, A. Desfarges-Berthelemot, D. Labat, A. L. Rouge, T. Mansuryan, and A. Barthélémy, "Spatially dispersive amplification in a 12-

core fiber and femtosecond pulse synthesis by coherent spectral combining," Opt. Express **21**(11), 13555–13563 (2013).
31. F. Guichard, M. Hanna, L. Lombard, Y. Zaouter, C. Hönninger, F. Morin, F. Druon, E. Mottay, and P. Georges, "Spectral pulse synthesis in large-scale ultrafast coherent combining systems," Eur. Phys. J. Spec. Top. **224**(13), 2545–2549 (2015).
32. H. Fathi, M. Närhi, and R. Gumenyuk, "Towards Ultimate High-Power Scaling: Coherent Beam Combining of Fiber Lasers," Photonics **8**(12), 566 (2021).
33. S. Hädrich, J. Rothhardt, M. Krebs, F. Tavella, A. Willner, J. Limpert, and A. Tünnermann, "High harmonic generation by novel fiber amplifier based sources," Opt. Express **18**(19), 20242–20250 (2010).
34. K. Ta Phuoc, S. Corde, C. Thaury, V. Malka, A. Tafzi, J. P. Goddet, R. C. Shah, S. Sebban, and A. Rousse, "All-optical Compton gamma-ray source," Nat. Photonics **6**(5), 308–311 (2012).
35. N. V. Vvedenskii, A. I. Korytin, V. A. Kostin, A. A. Murzanev, A. A. Silaev, and A. N. Stepanov, "Two-Color Laser-Plasma Generation of Terahertz Radiation Using a Frequency-Tunable Half Harmonic of a Femtosecond Pulse," Phys. Rev. Lett. **112**(5), 055004 (2014).
36. W. Leemans and E. Esarey, "Laser-driven plasma-wave electron accelerators," Phys. Today **62**(3), 44–49 (2009).
37. C. Benedetti, S. S. Bulanov, E. Esarey, C. G. R. Geddes, A. J. Gonsalves, A. Huebl, R. Lehe, K. Nakamura, C. B. Schroeder, D. Terzani, J. van Tilborg, M. Turner, J.-L. Vay, T. Zhou, F. Albert, J. Bromage, E. M. Campbell, D. H. Froula, J. P. Palastro, J. Zuegel, D. Bruhwiler, N. M. Cook, B. Cros, M. C. Downer, M. Fuchs, B. A. Shadwick, S. J. Gessner, M. J. Hogan, S. M. Hooker, C. Jing, K. Krushelnick, A. G. R. Thomas, W. P. Leemans, A. R. Maier, J. Osterhoff, K. Poder, M. Thevenet, C. Joshi, W. B. Mori, H. M. Milchberg, M. Palmer, J. G. Power, and N. Vafaei-Najafabadi, "Linear colliders based on laser-plasma accelerators," (2022).
38. F. Albert, M. E. Couprie, A. Debus, M. C. Downer, J. Faure, A. Flacco, L. A. Gizzi, T. Grismayer, A. Huebl, C. Joshi, M. Labat, W. P. Leemans, A. R. Maier, S. P. D. Mangles, P. Mason, F. Mathieu, P. Muggli, M. Nishiuchi, J. Osterhoff, P. P. Rajeev, U. Schramm, J. Schreiber, A. G. R. Thomas, J.-L. Vay, M. Vranic, and K. Zeil, "2020 roadmap on plasma accelerators," New J. Phys. **23**(3), 031101 (2021).
39. H. Pei, "High Fidelity Coherent Pulse Stacking Amplification with Intelligent System Controls," Thesis (2021).
40. H. Daido, M. Nishiuchi, and A. S. Pirozhkov, "Review of laser-driven ion sources and their applications," Rep. Prog. Phys. **75**(5), 056401 (2012).
41. J. Wang, G. Zhang, and Z. You, "Design rules for dense and rapid Lissajous scanning," Microsyst. Nanoeng. **6**(1), 1–7 (2020).
42. J. Ruppe, personal communication (2017).
43. G. D. Goodno and S. B. Weiss, "Automated co-alignment of coherent fiber laser arrays via active phase-locking," Opt. Express **20**(14), 14945–14953 (2012).
44. S. B. Weiss, M. E. Weber, and G. D. Goodno, "Group delay locking of coherently combined broadband lasers," Opt. Lett. **37**(4), 455–457 (2012).
45. M. Whittlesey, A. Rainville, C. Pasquale, M. Chen, S. Chen, Q. Du, and A. Galvanauskas, "Simultaneous coherent pulse stacking amplification and spatial combining of ultrashort pulses at multi-mJ energies," in *Fiber Lasers XIX: Technology and Systems* (SPIE, 2022), **PC11981**, p. PC119810B.

46. S. G. Rykovanov, C. G. R. Geddes, J.-L. Vay, C. B. Schroeder, E. Esarey, and W. P. Leemans, "Quasi-monoenergetic femtosecond photon sources from Thomson Scattering using laser plasma accelerators and plasma channels," J. Phys. B At. Mol. Opt. Phys. **47**(23), 234013 (2014).
47. F. V. Hartemann and A. K. Kerman, "Classical Theory of Nonlinear Compton Scattering," Phys. Rev. Lett. **76**(4), 624–627 (1996).
48. C. G. R. Geddes, S. Rykovanov, N. H. Matlis, S. Steinke, J.-L. Vay, E. H. Esarey, B. Ludewigt, K. Nakamura, B. J. Quiter, C. B. Schroeder, C. Toth, and W. P. Leemans, "Compact quasi-monoenergetic photon sources from laser-plasma accelerators for nuclear detection and characterization," Nucl. Instrum. Methods Phys. Res. Sect. B Beam Interact. Mater. At. **350**, 116–121 (2015).